UNIVERSIDADE FEDERAL DE SÃO CARLOS
Centro de Ciências Exatas e de Tecnologia
Programa de pós-graduação em Física

Carrier dynamics of low-dimensional semiconductors: from quantum wells and quantum dots to resonant tunneling devices

Andrea Naranjo López

Thesis presented to the Academic Faculty at Universidade Federal de São Carlos in partial fulfillment of the requirements for the Doctoral Degree in the Graduation Physics Course

Advisor: Prof. Dr. Marcio Daldin Teodoro

São Carlos
July 2021

Ph.D thesis

Carrier dynamics of low-dimensional semiconductors: from quantum wells and quantum dots to resonant tunneling devices

Andrea Naranjo Lopez

Departamento de Fisica

Universidade Federal de Sao Carlos

Grupo de Nanoestruturas semicondutoras

July 2021

Supervisor: Marcio Daldin Teodoro

UNIVERSIDADE FEDERAL DE SÃO CARLOS

Centro de Ciências Exatas e de Tecnologia
Programa de Pós-Graduação em Física

Folha de Aprovação

Defesa de Tese de Doutorado da candidata Andrea Naranjo López, realizada em 22/07/2021.

Comissão Julgadora:

Prof. Dr. Márcio Daldin Teodoro (UFSCar)

Profa. Dra. Helena de Souza Bragança Rocha (UnB)

Prof. Dr. Marcio Peron Franco de Godoy (UFSCar)

Prof. Dr. Leonardo Cristiano Campos (UFMG)

Prof. Dr. Ariano de Giovanni Rodrigues (UFSCar)

O presente trabalho foi realizado com apoio da Coordenação de Aperfeiçoamento de Pessoal de Nível Superior - Brasil (CAPES) - Código de Financiamento 001.
O Relatório de Defesa assinado pelos membros da Comissão Julgadora encontra-se arquivado junto ao Programa de Pós-Graduação em Física.

I dedicate this thesis to all 75 *homicidal violence and 89 missing victims*
in the framework of the national strike in Colombia,
from April 28, 2021, to date.
And, of course, to my peculiar family.

Acknowledgements

I want to thank everyone who supported me during the development of my work.

Prof. Dr. Marcio Daldin Teodoro For welcoming me into his group and advisor me all these years.

Prof. Dr. Victor Lopez-Richard Special thanks for his immense support during the final stage of this thesis and all the inspiring discussions.

David Guarin Castro For all his support during my Ph.D. and for sharing his knowledge about physics and life itself with me. I cannot thank you enough for this.

Fabian Hartmann and Andreas Pfenning For the collaboration, the reception at the TEP-UW and all the meaningful discussions.

Mother, Father and Brother For being the most incredible support, inspiration and motivation not only during this moment but for a lifetime.

Juan Camilo Barona Castaño For being my awakening consciousness soul mate, I would drive crazy without our long philosophical conversations.

Colombian, Brazilian and German friends, lab partners roommates and neighbors: For the shared moments with exaggerated cheeriness, listening to me for long hours of non-stop talking and all the messages of support in difficult moments.

Last but not least, I am grateful to CAPES for the doctoral scholarship granting, to DAAD for the doctoral internship scholarship-granting and the Examining Committee members for accepting to contribute to this work.

Andrea Naranjo López

"...no sabía porque este mundo a pesar de tener tantas leyes era tan injusto, comprendió que las leyes no controlarían sino los actos más no los pensamientos, pero nadie le da la razón a la locura, la razón humana es demasiado engreída para soportar la idea de que ella misma está equivocada."

Jaime Naranjo López

Resumo

Esta tese visa estudar heteroestruturas e dispositivos que desempenham um papel fundamental nas tecnologias nanoeletrônicas modernas. Focando nos materiais semicondutores do grupo III-V, especialmente sistemas baseados em arsenetos para aplicações em fotodetecção, serão tratados fenômenos relacionados com os efeitos do confinamento quântico dos estados energéticos de portadores de carga, os quais surgem quando a dimensionalidade é reduzida. Além disso, são discutidas as implicações macroscópicas desse confinamento principalmente nas propriedades ópticas e de transporte de diferentes dispositivos, os efeitos das heteroestruturas do tipo poço quântico de dupla barreira e a influência da introdução de pontos quânticos em sua arquitetura.

Realizadas as medidas de fotoluminescência resolvida por polarização em um poço quântico de GaAs, obteve-se uma melhor compreensão das propriedades desse sistema básico, especialmente de seus complexos excitônicos. Os resultados mostram emissões de éxcitons, biexcitons e tríons em função da temperatura, potência de excitação e campos magnéticos externos. Os éxcitons e biexcitons mostram diferenças essenciais em sua dependência quando aplicado um campo magnetico externo. Enquanto o desdobramento Zeeman dos biexcitons é monotonicamente dependente do campo magnético, com um fator g quase constante, os éxcitons apresentam um comportamento não monotônico, envolvendo uma inversão de sinal em função do campo magnético aplicado. O aparecimento da emissão ressonante do trion em um campo magnético finito, para baixas potências de excitação e uma dada polarização de spin (σ^+) é notório. A dependência não trivial dos níveis de energia com o campo magnético externo, junto com a emissão particular do mesmo para uma polarização, denota uma dinâmica acoplada entre éxcitons e trions, que pode ser descrita por um conjunto de equações de taxa acopladas. A abordagem

teórica utilizada mostra que um processo rápido de spin-flip poderia levar a uma emissão assimétrica e uma dinâmica de spin contrastante dos complexos excitônicos induzidos por sua carga. Uma vez que o sistema básico foi estudado, ideias e conceitos em sistemas com potenciais aplicações tecnológicas são desenvolvidas. Nesse contexto, um dos dispositivos semicondutores mais investigado é o diodo de tunelamento ressonante, não só porque executa respostas optoeletrônicas fortemente dependentes de parâmetros externos, como radiação, temperatura, campos elétricos e magnéticos, mas também devido aos vastos fenômenos físicos que ele permite abordar. Por exemplo, a geração, acumulação e controle de portadores de carga, são alguns dos parâmetros operacionais e de resposta de dispositivos. Portanto, torna-se fundamental estudar como esses três processos estão interligados. Aqui, a eletroluminescência desses diodos tem sido utilizada para investigar a dinâmica e o acúmulo de portadores de carga através da combinação de medidas de magnetoeletroluminescência e magnetotransporte. Os resultados da magnetoeletroluminescência, permitem, entretanto a avaliação dos processos de transporte de carga intrínsecos sem a necessidade de aplicação de luz externa, onde os meios de magnetotransporte não são mais eficazes.

Finalmente, foi estudado um diodo de tunelamento ressonante com uma camada de pontos quânticos de InGaAs integrada, buscando o benefício derivado da característica principal do mesmo, a sensibilidade da corrente de tunelamento às mudanças no potencial eletrostático local, para realizar a fotodetecção. Em princípio, isso poderia levar à detecção de fótons individuais, ou seja, à resolução numérica de fótons. Os resultados de espectroscopia de transporte, fotocorrente e eletroluminescência revelam que o acúmulo de portadores de carga é mantido pelos pontos quânticos, demonstrando que a estrutura proposta é suscetível à captura individual de buracos fotoexcitados. É proposta uma explicação teórica na qual o produto de funções dependentes da voltagem aplicada define como o acúmulo de portadores de carga induz um deslocamento na voltagem de operação do dispositivo e visa quantificar o processo de detecção de um fóton único.

Abstract

This thesis aims to study heterostructures and devices that play a fundamental role in modern nanoelectronic technologies, focusing on group III-V semiconductor materials, especially arsenide-based systems, for photodetection applications. The area under discussion deals mainly with phenomena related to the effects of quantum confinement of the charge carrier energetic states that arise when the dimensionality is reduced. It is also discussed the macroscopic implications of this confinement, mainly on the optical and transport properties of the studied heterostructures. This work will address the effects of heterostructures with quantum wells and the influence of introducing quantum dots within their architecture.

Beginning with polarization-resolved photoluminescence in pure GaAs quantum wells to get a first and better understanding of the properties of this basic system, especially its excitonic complexes. The results show excitons, biexcitons and trions emissions tuned by temperature, excitation power and external magnetic fields. Excitons and biexcitons show essential differences in their dependence on the external field. While the Zeeman splitting of biexcitons is monotonically dependent on the magnetic field, with a nearly constant g-factor, the behavior of the exciton energy division is not monotonous, involving a signal inversion as a function of the magnetic field. Remarkably, a trion resonance emergence in a finite magnetic field appears at low power excitation and σ^+ polarization. The non-trivial dependence of the energy levels with the external magnetic field, together with the particular polarization trion emission, denotes an intricate exciton and trion dynamics, which a set of coupled rate equations can describe. The theoretical approach used shows that a rapid spin-flip process could lead to an asymmetric spin emission and contrasting spin dynamics of the exciton complexes induced by their charge.

Once the basic system has been developed and studied, the ideas and concepts in systems with more potential technological applications are related. In this context, one of the most widely investigated semiconductor devices is the resonant tunneling diode, not only because it performs optoelectronic responses strongly dependent on external parameters such as voltage, incident light and temperature, also due to the vast physical phenomena that it allows to address and study. Since excitation, accumulation, and charge transport control are the operating parameters and responsiveness of the device, it is critical to study how these three processes are intertwined. Here, the electroluminescence of these diodes has been used to investigate the dynamics and charge carrier accumulation through the combination of magneto-electroluminescence and magnetotransport measurements. Magneto-electroluminescence results shed light on blind spots where magnetotransport media are no longer effective and enabling the assessment of intrinsic charge carrier transport processes without the need to illuminate the sample.

Finally, a resonant tunneling diode with an integrated InGaAs quantum dot layer is studied, seeking the benefit derived from the main characteristic of this type of diode to carry out photodetection; the sensitivity of the tunneling current to changes in the local electrostatic potential. In principle, this could lead to the detection of individual photons, i.e., photon numerical resolution. Transport, photocurrent and electroluminescence spectroscopy results reveal that the accumulation of charge carriers is maintained by the quantum dots, demonstrating that the proposed structure is susceptible to capturing individual photoexcited holes. A theoretical explanation is proposed, where the product of different voltage-dependent functions defines how the accumulation of charge carriers induced the voltage change and aims to quantify the single-photon detection process.

Contents

Chapter 1

Introduction

Electronics have been the main drive that has supported the development of all modern technologies and has played a fundamental role in science since the integrated circuit invention in 1959 [1]. For many years, progress in research and technology has been based on silicon-based materials operating at the microscale. However, over time, silicon-relied technologies have reached the upper limit of size reduction, straining electronics to investigate different materials that could be used at the nanoscale. A significant reduction of the device from its initial size of 10 microns forty years ago to 2 nm today has been achieved. However, 30 nm is roughly the limit of the physical characteristic size for classical semiconductors. Therefore, the key to further development lies in entirely new technology, the so-called nanoelectronics, which is the science that deals with electronic components designed and built on a molecular scale [2, 3]. For this purpose, the bulk material is being replaced by systems formed by thin films in the form of quantum wells (QW), quantum wires (QWR) or even quantum dots (QD). When the size is reduced to the nanoscale, innovative new physical phenomena arise mainly due to the quantum effect produced by the confinement of carriers in a region whose characteristic size is comparable to the order of its De Broglie wavelength, becoming necessary to apply quantum mechanics. As a result, new properties of the electronic system can be exposed, such as the discretization of the energy levels of the charge carriers on the dimensionality; this is the quantum nature that describes semiconductor nanostructures [2, 4–7].

Charge carrier transport through two-dimensional (2D) systems is most significantly characterized by the resonant tunneling effect, while one-dimensional systems (1D) can be understood using Coulomb blockade concepts, sequential tunneling or co-tunneling, both through double barrier systems (DBS) [7, 8]. For this reason, a structure that has received significant interest due to the physical phenomenon behind its operation is the resonant tunneling diode (RTD) [4], emerging as a pioneering device in the mid-1970s in the fields of nanoelectronics and optoelectronics, since RTDs can act as light emitters and detectors as well [6, 9]. Fundamentally, an RTD is a semiconductor device composed of a potential

DBS, separated from each other, forming a QW, and highly doped layers at the ends that raise the Fermi level above the conduction band and create accessible states for electrons to tunnel within the device [3–5]. Despite the RTD's simple structure, it has become of great interest and extensive research due to the wide range of applications based on these structures, from the point of view of both quantum transport physics and its application in functional quantum devices. This device has played a significant role in disseminating fundamental physics phenomena, allowing the advance towards the investigation of more complex and sophisticated quantum systems [6, 9] as is the case of this thesis, which aims to study the charge carriers dynamics of three different semiconductor optoelectronic devices, exploiting the intrinsic effects of introducing QW and QDs within the structure.

In terms of optical properties, light emission allows extracting information about the structure such as composition, energy band gap, layer thickness, system temperature, charge accumulation and dynamics, which enriches the transport scenario and intrinsic semiconductor properties. However, light emission under certain conditions, such as from exposure to an electric field, known as electroluminescence, is undesired in terms of light detection because the competition between transport and recombination processes can disturb the system affecting the performance of the photodetector. Nevertheless, from the point of view of investigating quantum phenomena, this effect is beneficial. It provides information on the resonant tunneling process and reveals characteristics of the transport mechanisms of available charge carriers, such as charge accumulation, emission energies and quantization effects.

In this sense, this doctoral thesis turns to account for the combination of optical phenomena with electric and magnetic fields in quantum-well-based structures exploiting the nature of the transitions between the energy bands through photoluminescence and electroluminescence phenomena and of the transport characteristics to shed light on the charge accumulation functioning and the photon-detection mechanism to contribute to the development of optoelectronic devices, such as single-photon detection using RTDs with embedded QDs (QD-RTD).

The document is organized as follows. Chapter 2 presents a theoretical background of the main physical concepts and properties of the structures under study necessary to understand the work in general. Starting with the basic properties of As-based systems followed by the concept of semiconductor heterostructures and their versatility in device fabrication, essentially QWs, QDs and RTDs. The mechanism of resonant tunneling and how electrical transport occurs are presented. Then, the phenomena of magneto-tunneling and electroluminescence are highlighted. In addition, to close the chapter, a review of the fundamental principle of QD-RTD is given.

Chapter 3 introduces the investigated samples, describing how they are constituted in terms of composition, layer thickness and doping levels. A brief description of the

fabrication procedures and the experimental techniques for optical, electrical and magnetic characterization are presented. During this work, the main experimental setup was the confocal microscope, associated with cryogenic systems, different excitation lasers, and simultaneously with electrical configurations for transport measurements.

In chapter 4, the results of a magneto-optical study on a GaAs/AlGaAs QW are presented. The excitonic complexes' emissions, binding energies and spin structure as a function of the excitation intensity, temperature and external applied magnetic fields are determined experimentally and theoretically explained in terms of population evolution, i.e., creation, recombination, and spin relaxation of the identified excitons, biexcitons and trions.

Chapter 5 presents the main results obtained from the electronic transport and magneto-optical measurements when comparing a conventional GaAs/AlGaAs RTD with a GaAs/$Al_{0.6}Ga_{0.4}As$ RTD that contains an $In_{0.15}Ga_{0.85}As$ emitter prewell. The main differences in electronic transport and electroluminescence emission under external parameters as magnetic fields and temperature point out the advantages of introducing a prewell layer adjacent to the emission barrier, and the advantage of using the combination of magneto-transport and magneto-electroluminescence to complement the determination of charge carrier dynamics in RTDs.

Chapter 6 is aimed at presenting an AlAs/GaAs RTD with embedded InGaAs QDs. The initial analysis from the transport measurements allows identifying the optimal AlAs barrier thickness for the QD-RTD operation. Optical measurements demonstrate optically active QDs, which perform as trapping charges. Thus, the effects on the electrostatic potential of the captured charges carriers were experimentally evidenced and explained through a theoretical charge accumulation model.

As a final part, the conclusions of this work and the scientific contributions to the area are presented.

Chapter 2

Theory

This chapter presents a theoretical foundation of the main contents and concepts involving the materials' structure and physical properties of the systems under study, first, reviewing the III-Vsemiconductors group's basic properties, mainly the As-based systems. A brief description of their crystalline structure and an explanation of the energy bands is carried out, followed by the concept of semiconductor heterostructures and their versatility in the manufacture of devices, mainly using semiconductors' heterostructures such as quantum-wells, quantum dots, and finally resonant tunneling diodes. The quantum tunneling phenomena is discerned from the main transport properties. The effects of charge distribution, magneto-tunneling and electroluminescence are examined. To conclude the chapter, a revision of the main works of the single-photon detection mechanism using RTDs with embedded quantum dots is made.

2.1 Structural and electronic properties of the III-V semiconductor family

This section will briefly describe the band structure of the principal materials that constitute the heterostructures systems that have been studied in this thesis: Gallium arsenide (GaAs), indium gallium arsenide (InGaAs), aluminum arsenide (AlAs) and aluminum gallium arsenide (AlGaAs). These are the so-called semiconductors compounds of the III-V family, which usually crystallize in diamond lattice or zinc blend structures that belong to the tetrahedral phases. Two face-centered cubic lattices form the diamond and zinc blend structures (CFC) shifted by a quarter of each other along the cube's main diagonal. In Figure 2.1 (a), the constituent atoms arranged in regular tetrahedrons, with sp^3 hybridized bonds are represented. GaAs is the most studied and, technologically, the most important from the semiconductor group III-V compounds, due to their advantages in high electron

mobility over their Si-based counterparts. For this reason, most of the band structure parameters are known with better accuracy for GaAs than for other semiconductor compounds. Considering that As is the element from group V used on all experiments during this study, the lattice constant (a) of the crystal depends only on the group III element. For GaAs $a = 5.6533\,\text{Å}$ [10–12]. The crystal lattice is defined in real space; however,

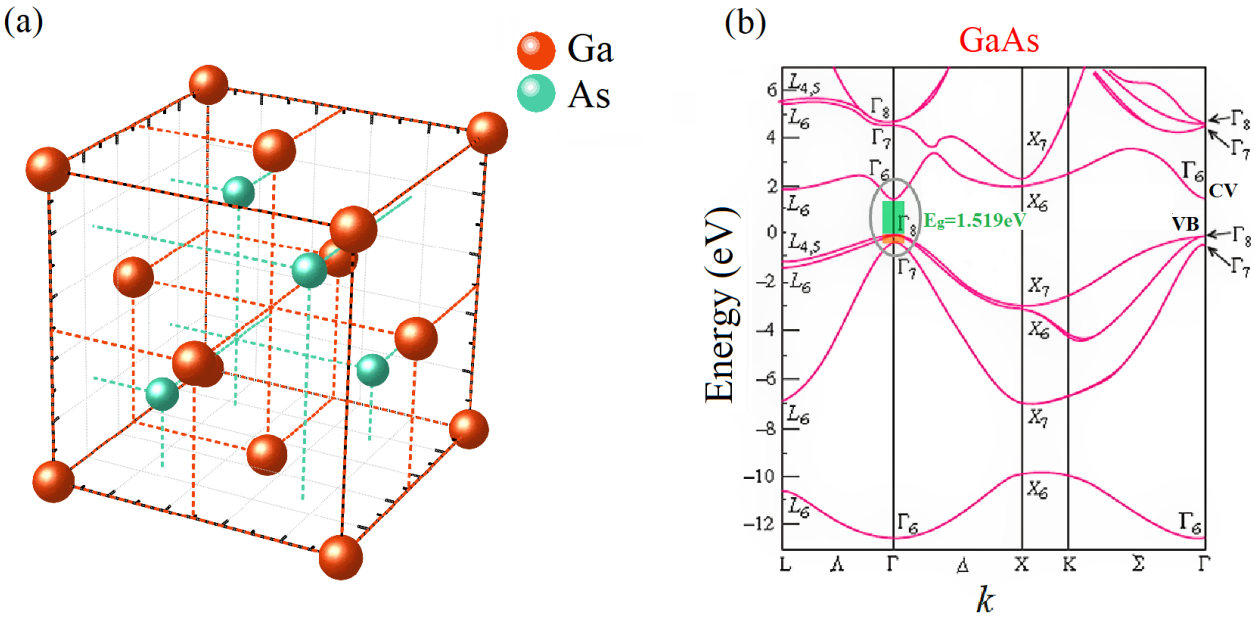

Figure 2.1: (a) Schematic illustration of the spatial distribution of atoms in a zincblende GaAs crystalline structure, Ga atoms are colored in orange and As atoms in green (adapted from [12]). (b) GaAs energy band structure as a function of the wavevector k.

important characteristics can be deduced when considering the reciprocal lattice in the momentum space. The reciprocal lattice defines allowed $\boldsymbol{k}$ states of the respective crystal structure. Because it is also periodic, a unit cell can be defined, where the first zone, called the Brillouin zone, contains all the necessary information that defines the behavior of an electron propagating through the lattice. The reciprocal lattice of the face-centered cubic lattice is a body-centered cubic lattice, and its the first Brillouin zone. The band structure represents the energy distribution of electrons as a function of the wave vector in a solid and can be calculated in each direction of the high symmetry points. The valence electrons are only weakly bonded to the atoms and are delocalized over the crystal structure. Therefore, the band structure can be calculated by solving the Schrödinger equation for electrons in the periodic potential of the ions. For GaAs, at a temperature of $T = 0\,\text{K}$, the band structure shows a direct bandgap (E_g), i.e., the maximum of the valence band and the minimum of the conduction band are in the center of the first Brillouin zone, at $k = 0$, with an energy gap of $E_g = 1.519$ eV (the bandgap is defined as the energy

difference between the valence and conduction band)[10, 11, 13]. As an example, Figure 2.1 (b) shows the GaAs energy band structure as a function of the wave vector $\boldsymbol{k}$ for different directions in the Brillouin zone. Therefore, this material is suitable for optical applications since there is no need for phonons to ensure a transition of electrons from valence to the conduction band. Unlike GaAs, AlAs is an indirect-gap semiconductor. However, due to its frequent substitutional incorporation into GaAs-based systems, AlAs is also an essential optoelectronic material. When it comes to $Al_xGa_{(1-x)}As$ alloys, its energy dispersion is similar to that of GaAs, remaining a direct bandgap for aluminum concentrations lower than $x \sim 0.45$. Above this value, the gap yields to indirect.

2.2 Semiconductor heterostructures

The types of materials involved in modern electronics, in general, are metals for contacts, semiconductors for active components of a device and high-bandgap materials for insulation. The group III-V semiconductors, GaAs, for example, is used for detectors and photonic devices. Another important feature is the type of system that these materials form. In that sense, surfaces, interfaces, and dimensionality play a crucial role in semiconductor technologies. Surface relates to the boundary between a solid and a gas; interface refers to the border between two different solids, as a semiconductor and a metal or two different semiconductors. In this sense, the compromise of more than one kind of material is known as a heterostructure. Finally, the dimensionality or, better, the progressively reduced dimensionality offers the possibility of tuning the electronic and optical characteristics of their macroscopic equivalents following the effects that quantum confinement has on electronic states. [6] From heterostructures with 2-D as quantum wells, researchers have gone to even 1-D quantum wires and 0-D quantum dots. This work will mainly address the effects of 2-D and the effects of introducing quantum dots in these structures.

2.2.1 Quantum well

Esaki and Tsu's (1969) proposed the designing of superlattices with one-dimensional periodic potential using layered structures by alternating thin films of two semiconductors of varying bandgaps, [3, 4] allowing the development of systems that provides devices with unique properties for both applications and the study of fundamental physical phenomena. Before the broad concept of the superlattice, the formation of the potential barrier and quantum well is the focus of this work. This structure consists of semiconductor layers with an interface geometry, doping level and chemical composition defined with

atomic-scale precision. In general, growth on III-V semiconductor base materials is performed by molecular beam epitaxy (MBE) or metal-organic chemical vapor deposition (MOCVD). The structure provides a periodically variable energy band profile created by the difference in the bandgap of the semiconductor sandwiched between other two semiconducting materials that must have a larger energy gap compared to the first one (the name of "quantum well structure" results from this sandwich energy profile). The most common interface consists of GaAs and $Al_xGa_{(1-x)}As$, with x varying between 0.1 and 0.4 to guarantee that high-quality single-crystalline layers can be obtained. The resulting potential profile is shown in Figure 2.2. Due to closely matched lattice spacing in this concentration and the similar chemical composition, the interface is very sharp and well-defined. The superposition of materials with gaps of different energies follows the formation of a confinement region (the quantum well) of charge carriers with energy levels that are characteristic and distinct from the individual volumetric materials. In the AlGaAs/GaAs/AlGaAs interfaces, electrons are trapped in the GaAs layers by the AlGaAs barriers potential due to the discontinuities in the conduction bands of both. Likewise, holes are trapped by a discontinuity in valence bands. Barriers quantize states in the growth direction (z), but carrier movement remains unrestricted in the other two directions [3–6]. Figure 2.2 is presenting a typical double-barrier heterostructure forming

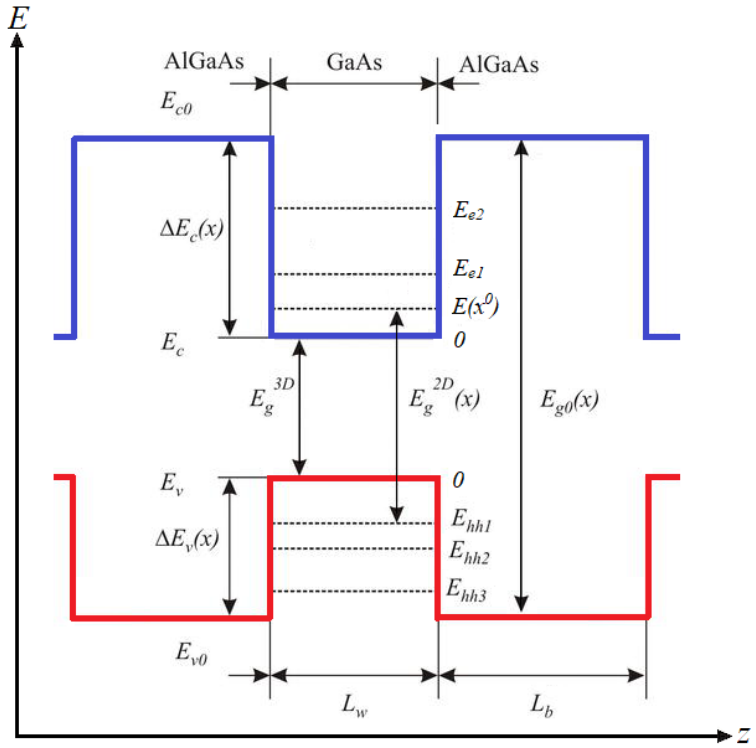

Figure 2.2: Bottom of the conduction band in blue and top of the valence band in red, for a GaAs/AlGaAs quantum well with the main energy values of such a structure.

the quantum well (QW), the thickness of these barrier layers (L_b) and the width of the quantum well (L_w). The height of the barrier ΔE_c is determined by the mole fraction of aluminum (x) in the barriers. E_g^{3D}, E_g^{2D} and E_{g0} are the bandgap energy values for GaAs in bulk, in QW and for AlGaAs, respectively. The energetic position of the quantum levels E_{e1} and E_{e2} for electrons, $E(x^0)$ for excitons and E_{hh1}, E_{hh2} and E_{hh3} for holes depends not only on the thickness of the quantum well but also on x since the height of the barrier is not infinite. The electrons can move from a ground quantum level E_{e1} to the first excited level E_{e2} after the absorption of a photon with energy $\hbar\omega$ [14]. Unlike the bulk case, the probability of transitions between subbands depends on the direction (polarization) of the electric field in the incident electromagnetic wave. In the QW, the electron is confined, and because of the finite width of the well (L_W), the electron will have zero-point energy, which roughly is given by $E = \pi^2\hbar^2/2m^*L_w^2$, where m^* is the effective mass (this is the result in the limit of a square well with infinite barriers)[15].

Photoluminescence experiments have shown that the absorption occurs in the AlGaAs barriers for all energies where $\hbar\omega > E_{g0}$, exciting electrons from the valence to the conduction band. Some have the possibility of getting trapped in the QW states, and the same can happens for holes in the valence band, allowing an electron to fall from the conduction band into a hole in the valence band, releasing the difference in energy as light. Alternatively, electrons and holes can bind together with less energy than the hole electron pair itself, forming quasi-particles known as exciton or excitonic complex depending on the number of carriers involved in the binding process, i.e., with an excess of electrons or holes, biexcitons and trions can be created. Well-known examples of these exciton complexes are excitons and biexcitons, analogs of hydrogen atoms and molecules, respectively. However, this analogy cannot be used to estimate the biexciton binding energy since the effective masses of the electron and hole are generally comparable. [16, 17].

Figure 2.3 presents a schematic illustration of the band structure with the conduction (CB) and valence band (VB) edges profiles with the main excitonic quasi-particles: exciton (X^0), biexciton (XX) and negative trion (X^-). By definition, an exciton is an electron (e^-) bound to a hole (h^+) based on Coulomb interaction [18]. A biexciton is a bound state of two electron-hole pairs, i.e., when two excitons occupy their s-shell state. Although the XX and X^0 are in the same orbital, their recombination energy is different due to the Columb interaction between the two X^0.

The total angular momentum for a XX is: $J = S + L = 0$ due to the orientation of the spins ($S = 0$) and the orbital angular momentum ($L = 0$) for the s-shell. Consequently, no optical transition to the ground state ($J = 0$ as well) is possible because the dipole approximation leads to selection rules that change the total angular momentum of an optical transition by ± 1. Therefore a XX relaxes first into the X^0-state through the emission of a photon. For X, the angular momentum component in z-direction (growth

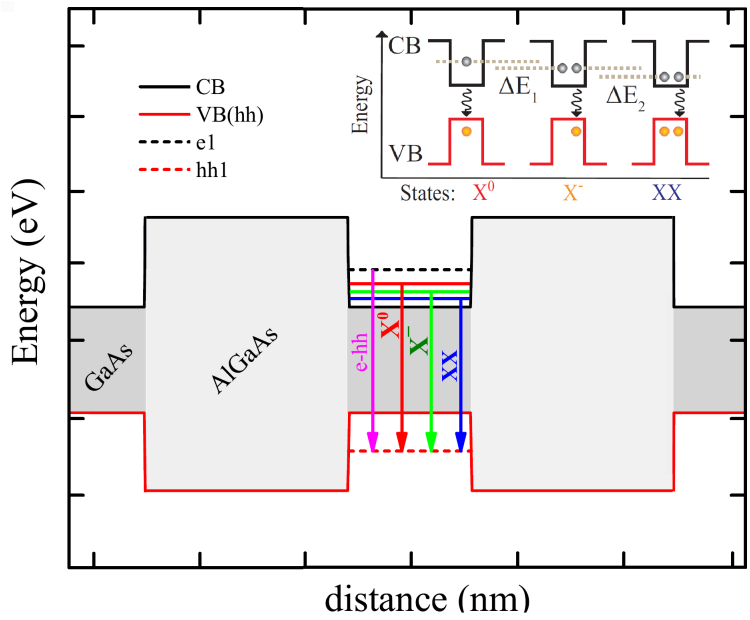

Figure 2.3: QW conduction and valence bands profiles with the optical transitions involving exciton (X^0), biexciton (XX) and negative trion (X^-). The inset shows a schematic band structure of carriers confined in a QW and the different excitonic complexes forming when electrons (grey circles) and holes (orange circles) recombine.

direction) is $J_z = j_{z,e^-} + j_{z,h^+} = \pm 1; \pm 2$ because e^- has a spin of $j_{z,e^-} = s_{z,e^-} = \pm 1/2$ and h^+ of $j_{z,h^+} = \pm 3/2$. Here the transition from the $|\pm 1\rangle$ excitons to the empty ground state is optically allowed. These X^0 are referred to as bright exciton. Its advantage over the electron and hole spin is its neutrality and insensitivity to its electrostatic environment. The transition from the $|\pm 2\rangle$ is referred to as dark excitons in which the electron and the heavy-hole spins are oriented parallel to each other. In this case, a single photon can not take the total spin, and the pair is optically inactive; like the bright one, the dark exciton is neutral [19]. When it is possible to get one extra charge in addition to an X^0, those states are called trions. Trions have either an additional h^+ or e^- (X^+, X^- respectively).

One of the most relevant characteristics of the motion of the excitonic complex is the proximity to the two-dimensional limit; as a result, the electron-hole wave-function overlap increases, resulting in an enhancement (up to a factor of 4 compared with the bulk) of the excitonic binding energy [20]. Furthermore, they dominate the optical spectra of semiconductors close to the bandgap. The optical properties of excitonic complexes in high-quality GaAs/AlGaAs quantum wells have been the subject of extensive study. Optical excitation and relaxation processes provide theoretical bases for confined electron band theory and the coupling between exciton states. Moreover, quantum wells provide a basis for a wide range of photoelectronic applications, such as light-emitting devices,

laser technologies and photovoltaics [20–24].

Magneto-optic studies are of interest to also explore magnetic g-factors and the effective Zeeman splitting of electrons, holes, and excitonic complexes in quantum wells [25, 26]. The radiative recombination efficiency of excitons can be improved by introducing a magnetic field, and this becomes relevant for phenomena, such as the quantum Hall effect, magneto-optical polarization measurements, electron-nuclear spin coupling, and optical detection of nuclear magnetic resonance [24, 25]. Although magnetoexcitons are beneficial for many emission-based devices, the short recombination lifetime of electron-hole pairs is detrimental to applications which the separation and transport of carriers are relevant [24–26]. Finally, for doped quantum wells, it has been established that the spin population of minority carriers at the band edge determines the luminescence polarization when the intensity of the exciting light is weak [27]. In turn, for undoped wells, the photoexcited populations of electrons and holes have the same density, and the polarization of the observed luminescence is influenced by the relaxation processes that occur in both bands [28].

2.2.2 Quantum dots

Quantum dots (QDs) are ultrasmall size low-bandgap semiconductor nanocrystals made up of 100-10,000 atoms embedded in a higher bandgap semiconductor. They impose a three-dimensional (3D) confinement on charge carriers due to their dimension, comparable to the De Broglie wavelength of the carriers. Therefore, QDs can be described as a zero-dimensional (0D) system. The quantum confinement effects lead to unique optical properties due to changes in bandgap, like a discrete spectrum with well-separated quantized states. The electronic states of each energy level exhibit wave functions that are more atomic-like. Since the QDs solutions for the Schrödinger wave equation is very similar to those for electrons bound to a nucleus, QDs are often referred to as artificial atoms, and atomic-like sharp emission peaks are observed, with typical intraband energy levels in the range of 10-100 meV [29]. Thus, the energy levels in a QD are named after the shells of an atom, starting with the s-shell as the lowest energy level.

QDs were first described in 1981 by Ekimov and Onushenko [30]. Later in 1982, Efros and Efros [31] postulated that the effects of quantum size cause changes in the optical and optoelectronic properties. In general, QDs are synthesized from group II-VI (CdSe, CdS, ZnO, ZnS), III-V (GaN, GaP, InP), and IV-VI (PbSe, PbS) elements [29]. Within the QDs, charge carriers can be created through electrical or optical excitation, implemented through doped layers near the QDs, applying a voltage, or randomly getting trapped by the QD potential when using an above-band excitation. However, in QDs, the energy required to create an exciton increase with decreasing size. Smaller QDs possess

larger bandgap energy, emitting photons of higher energy (blue shifted) and vice-versa. Analogous to the case of the QW, the trapped carriers can recombine, releasing a photon with the equivalent difference in energy or bind together, creating exciton quasi-particles [29, 32]. The Coulomb interaction between the three particles leads to a shift in the energy of the emission spectrum compared to the X^0-state. Figure 2.4 shows a schematic illustration of the three different ways that an exciton can be generated inside a QD.

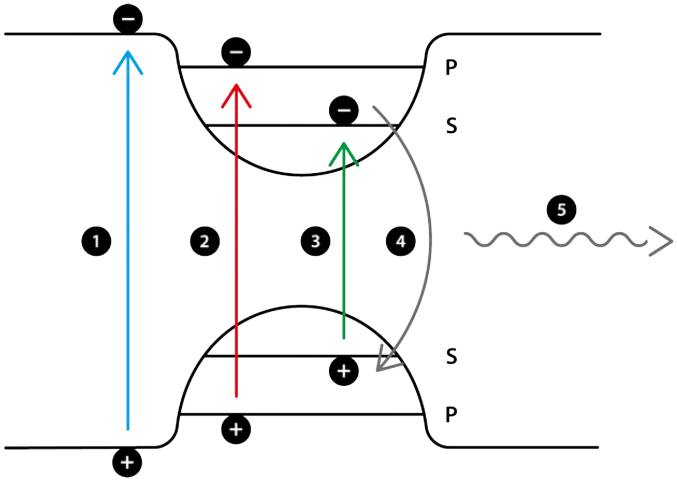

Figure 2.4: Illustration of different possibilities to creat an exciton. 1. non-resonant excitation, 2. quasi-resonant excitation, 3. resonant excitation. Point 4. shows the recombination of the lowest excitonic state and 5. the emission of a photon as a result of it. S stands for s-shell and P stands for p-shell. Valence band on the bottom, conduction band on the top (adapted from [33]).

1. Non-resonant excitation: Carriers in the higher bandgap semiconductor region are excited (1) and trapped within the QD. Since this region is not confined in a 0D system, the energy states are continuous. Thus, it is not required for the excitation energy to match with the energy levels. The trapping process occurs through relaxation based on phonon interaction on a time scale of $\sim 1 - 100\,\mathrm{ps}$.

2. Quasi-resonant excitation: Here, the excitation takes place within the QD. Carriers are raised to the upper shells (e.g. the p-shell) by optical excitation (2). From there, a relaxation of the phonons to the s-shell is possible on a time scale of $< 100\,\mathrm{fs}$.

3. Resonant excitation: This is the direct excitation to the s-shell of the QD (3). From this lower shell, recombination (4) of the carriers is possible. This also applies to non- and quasi-resonant excitation. The recombination leads to the emission of a photon (5) [34].

2.2.3 Resonant tunneling diodes

As introduced in the previous section, a quantum well is created by a double barrier structure (DBS) of intrinsic potential, sandwiching an intrinsic material with a smaller energy gap. Semiconductor devices composed of these layered systems (with the difference that the DBS is intentionally composed of finite barriers to study transport phenomena), with heavily doped layers at the extremities and electrically connected (emitter and collector contacts), are the resonant tunneling diode (RTD) basic configuration. The electrodes raise the Fermi energy level above the conduction band (CB), creating accessible states for electrons. Due to the nanometric characteristic dimensions of this kind of device, which is comparable to the electron wavelengths, it naturally leads to quantum phenomena such as interference, tunneling and energy quantization, among others [3–6]. When a bias voltage is applied, it distorts the energy bands, favoring the alignment of states. Hence, resonant transmission of electrons can occur through the quantum states created in the well when the energy of the electrons on the emitting side coincides with the energy of the quasi-bound state E_0. In other words, the phenomenon of resonant tunneling through the double barrier occurs at these resonant energy levels [6, 14], as depicted in Figure 2.5 (a). Thus, in the RTD, between the double barrier, quasi-bound states (resonant states) are formed, where E_0 represents the quantized level of the lowest energy.

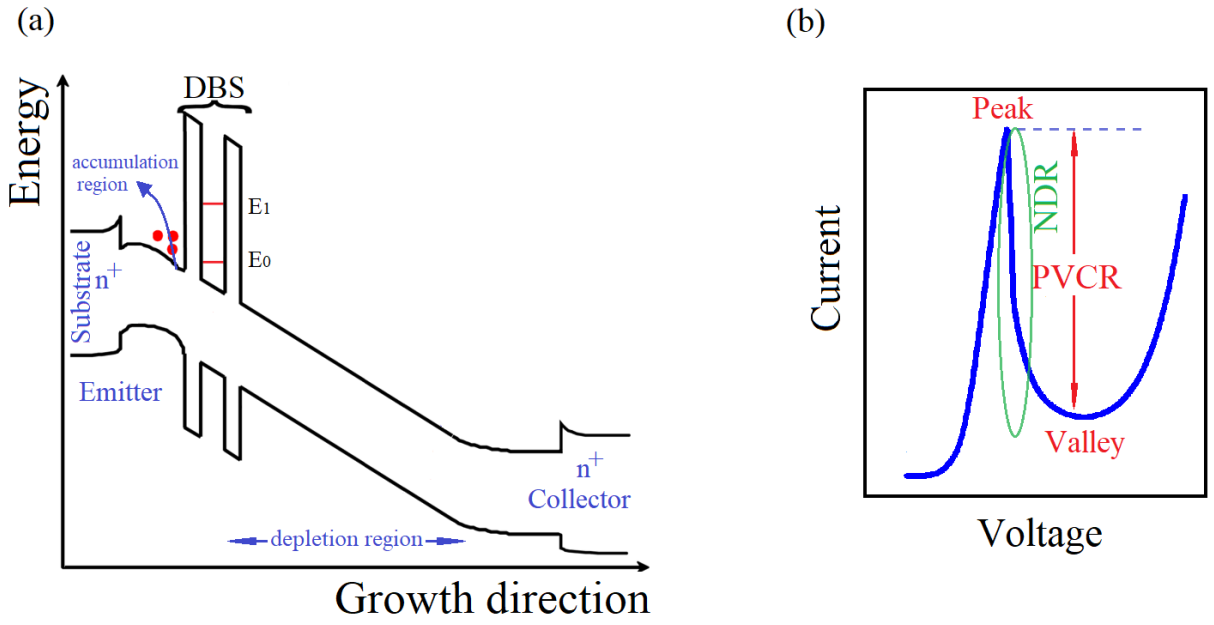

Figure 2.5: (a) Schematic profile energy band of the RTD under an applied electric field. (b) I(V) characteristic curve of an RTD.

As the voltage increases, the number of electrons that can pass through the DBS also increases, contributing to the current as shown in Figure 2.5 (b). With a specific voltage,

the level of the emitter-side conduction band is aligned with the resonance level of the quantum well (E_0), and a maximum appears in the current (peak) and then stops when E_0 drops below the bottom of the emitter's conduction band, resulting in a sudden reduction in current (valley), characterizing the negative differential resistance (NDR) range: the RTDs fingerprint [6, 35].

In addition to transport across resonance levels, one can also identify other transport processes across a double barrier. As already explained, electrons with coinciding energies with the resonant energies, E_0 and E_1 can tunnel through the double barrier with a probability of 1 (if the DBS is symmetric). In the emitter part, the accumulation of electrons in front of the first barrier bends the conduction band and causes a triangular-type potential with discrete energy levels. Thus, an electron can first be scattered to an energy level at this potential, absorb a phonon and sequentially cross the barrier through a resonance level. Alternatively, an electron with initial energy can interact with the vibration of the lattice, emitting a phonon and finally tunneling. On the other hand, electrons with sufficiently high energies can pass through the device, penetrating only through a barrier or even in the entire heterostructure by thermionic emission. Due to the high energy required in this process, the electrons involved are relatively unusual [14].

There is also a finite probability of incident electrons that can tunnel through the non-resonant energy levels that lie between the resonances [36]. Electrons can carry out thermionic emission processes for higher voltages, crossing over the double barrier, promoting an exponential increase in the electric current after the resonance peak. The characteristic current-voltage (I(V)) curve presented in Figure 2.5 (b) examples, in particular, the peak-to-valley ratio (PVCR) between the peak current and the minimum current. The I(V) region after the NDR is considered an important property in the characterization and use of RTDs as high-performance devices.

A simple tunneling model will be presented to describe these processes qualitatively. In the coherent tunneling model, the energy and momentum parallel to the barriers are conserved and the double-barrier structure is a translational invariant. In other words, the total energy of the electrons, $E(k)$, can be separated into lateral (x and y directions) and vertical (z-direction) components as follows [37]:

$$E(k) = \frac{\eta(k_X^2 + k_y^2)}{2m^*} + E_z, \tag{2.1}$$

where m^* is the electron effective mass and it considers the internal periodic potential of the crystal which forms the QW. An electron present in the energy band (either conduction or valence band) of a crystal, the mass of electron critically depends on the curvature of the energy band. The curvature is positive for conduction band and is negative for valence band.

The lateral movement of electrons is free and can be expressed as a simple plane wave with a lateral wave vector, $k = (k_x, k_y)$. The Fermi-Dirac distribution governs electronic density since the contacts are strongly doped to provide a low ohmic contact and high current density, which implies that electrons in the emitter region are considered to be in thermal equilibrium with their surroundings in the area of contact [6, 9, 37]. Figure 2.6(a) shows the distribution of charge density as a function of energy for a highly doped semiconductor, which has a maximum close to the Fermi level; this is expected to provide the most considerable number of carriers available for resonant tunneling. However, this contradicts the experimental observation since the maximum current in an RTD usually occurs when the QW states are near the bottom of the conduction band.

The resonant tunneling current through a double-barrier structure depends on the transmission probability, whose coefficient is correlated with the Fermi level at the electrode, imposing energy and momentum conservations between the 3D states of the emitter and the 2D states of the QW. Fermi energy is generally broad compared to the width of the quantum state in such a way that, at applied voltages, the current starts with the state that coincides with the Fermi level and ceases when the state is aligned with the bottom of the conduction band [9]. So, a sharp resonance in the tunnel current is observed for those voltage values where the Fermi level aligns with a confined level in the quantum well between the barriers [37].

A simple consideration can be made to calculate the current. In a 3D emitter, for $T = 0K$, the electrons occupy the Fermi sphere of radius k_f, which is the Fermi wavenumber in the emitter. Since the tunneling for the QW conserves the lateral wavenumbers, k_x and k_y, the electronic state involved in such a process can be represented by the interaction of the $k_f = q_r$ plane with the Fermi sphere, where q_r is the wavenumber associated with the energy of the resonant state relative to the conduction band [37]:

$$q_r = \frac{\sqrt{2m^*(E_0 + E_c^E)}}{\hbar}, \tag{2.2}$$

where E_0 is the QW resonant state, E_0^E is the energy of the edge of the conduction band. The density of tunneling current should then be proportional to the density of states indicated by the intersection circle in the Fermi sphere as shown in the Figure 2.6 (b).

While the transmission probability through the resonant state is approximately constant, over a small range of applied voltage, the tunneling current can be expressed as follows [37]:

$$J \propto \pi(k_f^{*2} - q_r^2) \propto (E_f^E - E_0), \tag{2.3}$$

where E_f^E is the local Fermi energy in the emitter. Since $(E_f^E - E_0)$ is proportional to the

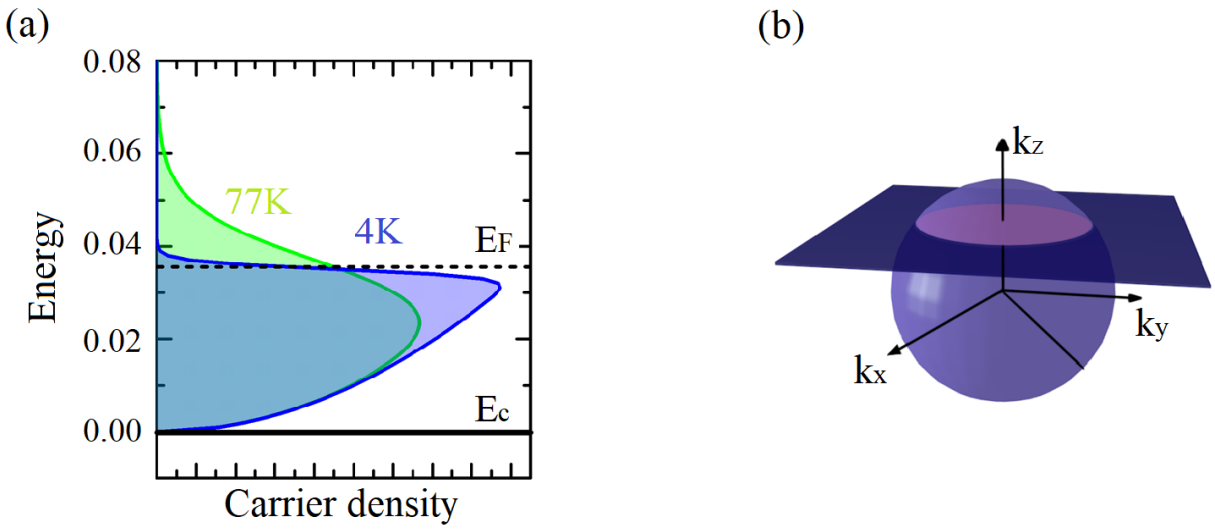

Figure 2.6: (a) Electronic distribution function in highly doped bulk semiconductors for 4 K (blue) and 77 K (green). E_c is the minimum of the conduction band and E_F, the Fermi level. The higher the temperature, the greater the energy distribution of carriers due to Fermi-Dirac distribution. (b) The intersection between the Fermi sphere of the distribution of states in k-space for the emitter side and the plane of a quantized state q_r. (Adapted from [38]).

applied voltage, J grows exponentially until E_0 drops below the end of the conduction band in the emitter region; displaying a minimum in the current [39]. The current density can also be obtained, defining the energies that hold incident and transmitted electrons, E and E', respectively. Due to a separation of the variables, the transmission coefficient T is just a function of the longitudinal energy (E_l) so that the current can be integrated over the transverse direction and assuming only the transmission of coherent waves from the emitter side; the current density expression is giving by [5],

$$J = \frac{em^*kT}{2\pi^2\hbar^3}\int_0^\infty T \ln\left(\frac{1+(\exp^{\frac{E_f-E_l}{k_BT}})}{1+(\exp^{\frac{E_f-E_l-eV}{k_BT}})}\right) dE_l, \tag{2.4}$$

According to Schulman et al. [40], the transmission coefficient in the Tsu-Esaki expression (2.4) can be obtained using a phenomenological function, and a few assumptions, such as a Lorentzian form for the transmission coefficient, symmetric barriers, that the half of the voltage drops from the emitter to the center on the QW that the width of the resonance level could be small enough to neglect the transmission coefficient for distant values from the resonance, i.e., $E_l \approxeq E_r - eV/2$, obtaining a function known as Schulman equation and given by [40],

$$J(V) = A \ln \left[\left(\frac{1 + \exp^{\frac{(E_f - E_r + eV/2)}{k_B T}}}{1 + \exp^{\frac{\left(E_f - E_r - eV/2\right)}{k_B T}}} \right) \right] \left[\frac{\pi}{2} + \mathrm{Tan}^{-1} \left(\frac{E_r - eV/2}{D} \right) \right] \tag{2.5}$$

where, A and D are determined from analysis fitting.

Another interesting feature of the RTDs is the electric bistability in the characteristic I(V) curves, where an electric hysteresis-like behavior appears in the path that the current follows when applying an increasing voltage differing from the path described when it returns by decreasing the voltage [4, 35]. This property is due to the double barrier structure in the device, where the accumulated carriers allow bands to bend when a voltage is applied. This may derive from the presence of an internal (intrinsic) or external (extrinsic) factor of the system, such as a series resistance connected to the device [41]. There is also a distinguishing feature of double barrier tunneling devices in terms of configuration, i.e., relatively easy manufacturing and its simplicity on the structural parameters. For this reason, distinct RTDs based on GaAs/GaAlAs alloys have been investigated by varying the compositions and the structural parameters of the well, the barriers and the electrodes [36].

These reasons put the RTDs as one of the most viable quantum-based devices to transition from the research world to the practical application. Mainly because they generate high-frequency electromagnetic waves in the terahertz (THz) range, allowing the development of novel devices such as THz oscillators, high-speed logic gates/light detectors, high switching speed and high cut-off frequency circuits [36]. Moreover, they are great candidates to be used in the construction of sub-millimeter wave signal sources, such as broadband communication systems, high-resolution radars, image generation systems in low visibility environments, remote probing of the terrestrial atmosphere, among others electronic and optoelectronic utilities [42–45]. Despite the wide range of applications already mentioned, the basic physics phenomena already demonstrated by the RTDs make these nanostructures a countless source of interesting physical problems to be explored. In addition, the progress in the epitaxial growth techniques has improved the manufacturing of heterostructures and, therefore, the improvement of their properties like the peak-to-value current ratio (PVCR) at room temperature. This temperature requirement is one of the essential characteristics that any new technology must satisfy for its implementation, distinguishing the RTDs from other interesting quantum device proposals that have been suggested but still operating at cryogenic temperatures [36].

In the sequence, specific effects in RTDs will be presented that will be useful for understanding the physics that will be explored in this thesis.

2.2.4 Magneto-tunneling: Landau levels

Electron motion always consists of two components if a magnetic field is present in its region of space, a uniform rectilinear movement along the field and a circular movement. Thus, the effect of the magnetic field on free carriers is to orientate them in circular orbits perpendicular to the field direction of the cyclotron radius $R_c = m\nu/eB$, where m is the mass of the charge carrier, ν the velocity and B the magnetic field, and the cyclotron frequency $w_c = eB/m$. Let $\vec{x} = (x_1, x_2, 0)$ be its position and P_i, X_i the position and momentum operators, respectively, the electron has the following Hamiltonian,

$$H = \frac{1}{2m}((P_1 - \frac{1}{2}eBX_2)^2 + (P_2 - \frac{1}{2}eBX_1)^2) \tag{2.6}$$

In quantum mechanics, the effect of the magnetic field causes the quantization of the energy of the system at Landau levels, where the plane waves of the free case are modified to wave functions with a shape similar to the harmonic quantum oscillator. Thus, the energy levels of the system in the plane perpendicular to the magnetic field are defined by $E_n = (n+1/2)\hbar\omega_c$, with $n = 1, 2, 3...e$, where n is the indexes of each Landau level [46].

In the case of RTDs, under a magnetic field parallel to the current of charge carriers, the lateral movement of electrons in a two-dimensional gas becomes quantized in Landau levels, both in the emitter and in the well, transforming the linear momentum quantum numbers in Landau indexes n. Thus, the charge carriers kinetic energy of the xy plane is replaced by the Landau levels, with the energy of an electron within the nth Landau level in the accumulation layer (E_{al}) given by:

$$E = E_{al} + (n + 1/2)\hbar\omega_c, \tag{2.7}$$

The energy for one electron at the Landau level n' from the QW (E_qw) is:

$$E = E_{qw} + (n' + 1/2)\hbar\omega_c, \tag{2.8}$$

For energy conservation in the tunneling process, equations 2.7 and 2.8 must be equal, that is, the Landau levels must be conserved ($n = n'$), given that the effective masses of carriers in the two confinement regions are equal. This type of tunneling is known as coherent magneto-tunneling. Figure 2.7(a) and (b) illustrate an electronic level scheme for the coherent and incoherent tunneling cases, respectively. In real cases, though, there will always be the presence of scattering processes (phonons, impurities, defects) that lead to incoherent tunneling, where there will be no conservation of Landau levels ($n \neq n'$). This transition is accompanied by a transfer of energy and momentum between longitudinal and transverse movements and is then necessarily assisted by elastic diffusion or scattering processes (interface roughness, alloy disorder and optical phonon emission).

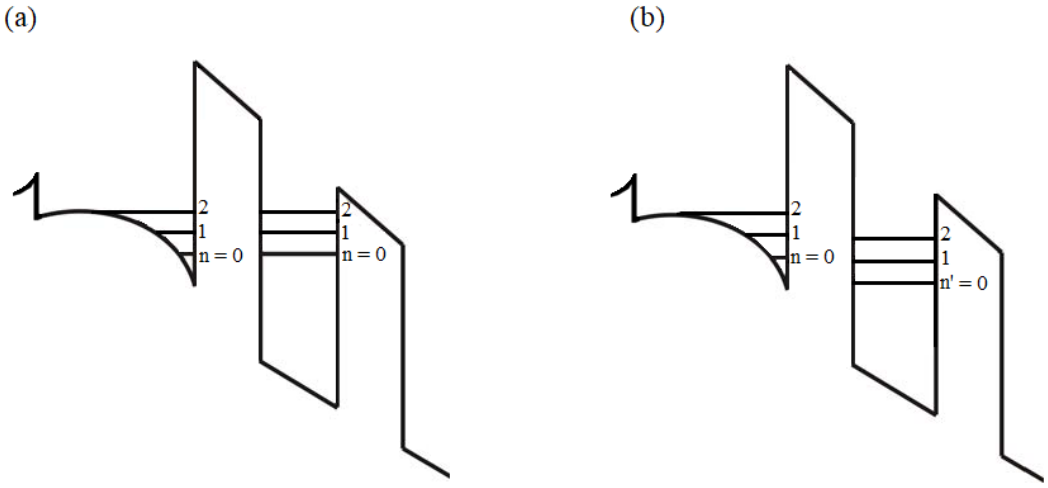

Figure 2.7: Schematic illustration of the electronic levels structure under the conditions: (a) coherent tunneling, with starting at n level and end n' with levels aligned. And (b) incoherent tunneling where the levels are misaligned.

These processes increase the linewidth of the states involved, causing the I(V) curve to lose its sharpness characteristic, broadening the peak and increasing the valley current, thus decreasing the peak-to-valley ratio.

2.2.5 Impact ionization process

Electron impact ionization of a molecule involves the transition between two well-defined (electronic, vibrational, and rotational) molecular states. It plays a crucial role in electron transport in semiconductors at high electric fields. It is another process that semiconductors can also exhibit under an applied electric field. This process can occur in heterostructures doped with pure donor (n-i-n) or acceptor (p-i-p) impurities. When the applied electric field reaches a specific value, usually on the order of hundreds of kilovolts per centimeter [11, 47], the distortion of the conduction band induced mainly in the intrinsic region promotes an acceleration in the electrons that gain enough energy to excite other carriers in less energetic states in the valence band by the impact ionization process. In RTDs, this process occurs in the collecting region where there is no more depletion.

Figure 2.8 shows an illustration of electrons that were previously located in the VB and promoted to the CB, leaving a hole in the VB, which are accelerated in the opposite direction and can recombine with electrons in different regions of the structure. The minimum energy for this process occur must be at least greater than the material energy gap. The different electric fields created in the heterostructure distort the depletion zone

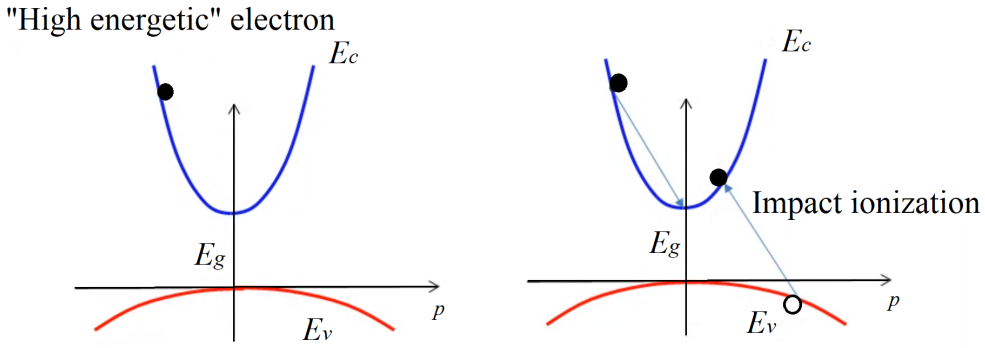

Figure 2.8: Illustration of an impact ionization process for a semiconductor with two parabolic bands. Since the electron is in a high energetic state, it can impact ionize a valence band electron.

to increase it; for example, when an electron-hole pair is photo-generated, the carriers are accelerated in opposite directions. If they hit with another charge carrier with a certain energy, in that case, they undergo impact ionization, exciting other carriers, and so on in a multiplication process until all ionization processes cease due to phonon relaxations and carriers move out of the impact ionization region. This multiplication process is characterized by an ionization rate α_n and α_p, defined by the number of electron-hole pairs generated by electrons and holes per unit distance. Therefore, an electron moving at speed ν_n has an ionization rate:

$$\alpha_n = \frac{1}{n\nu_n}\frac{dn}{dt}, \tag{2.9}$$

where n is the electron concentration and dn/dt the electron generation rate. Considering the complete scenario in which both electrons and holes contribute to impact ionization, the generation rate of electron-hole pairs (G^π) can be written as:

$$G^\pi = \frac{dn}{dt} + \frac{dp}{dt} = \alpha_n n\nu_n + \alpha_p p\nu_p = \alpha_n \frac{J_n}{q} + \alpha_p \frac{J_p}{q} \tag{2.10}$$

where J_n and J_p represent the current density for electrons and holes, respectively. The impact ionization rate, can also be determined through a numerical model, in the case without applied field, only in energy terms [48]:

$$\Pi(V) = C\left(\frac{E - E_{th}}{E_{th}}\right)^a, \tag{2.11}$$

where E is the electron energy, C and a are parameters derivated for each material system

and E_{th} is the energy threshold for the impact ionization to occur.

2.3 QD-RTD for single-photon detection

Single-photon sources and detection are essential for many optical quantum information applications such as quantum key distribution, boson sampling, quantum computation, quantum teleportation, medical imagining, and characterization of the quantum light source itself. Therefore, expanding the photon-counting capability of existing single-photon detectors to highly efficient detection even for weak light, with a good signal-to-noise ratio and photon-number-resolving, is highly desired [49].

Superconducting nanowire single-photon detectors (SNSPDs), photomultipliers tube (PMT) and avalanche photodiodes (APD) are some of those that have been traditionally used for single-photon detection. However, all these devices present advantages and disadvantages. For example, SNSPDs have shown high quantum efficiency combined with low timing jitter. Although, they suffer from significant dead-time after a detection event and do not provide any information on the exact photon number of the incident light pulse. On the other hand, PMT has high multiplication in the visible and UV spectral ranges, while its quantum efficiency is low in the infrared wavelength. Besides, PMT has limited spatial resolution. APD is the mainstream in the infrared wavelength region. However, it has an after-noise critical problem due to the avalanche working process [50–54].

Significant effort has been made to improve efficiency, sensitivity and embed technical problems. One of the latest developments is a field-effect transistor gated by a layer of quantum dots -a new class of devices employing the trapping of charge in defects to achieve single-photon detection [55, 56]. Semiconductor heterostructures based on III-V compounds form the basic device architecture with quantum dots (QDs) embedded in the material [50, 55–59] exploited to achieve trapping. QDs are favored to be controllably placed within the heterostructure to maximize internal efficiency and signal uniformity. The field-effect transistor showed high internal efficiency of up to 68% at 805 nm. In 2005, Blakesley et al. reported a new kind of single-photon detector based on the quantum dot resonant tunneling diode (QDRTD) [58]. The design relies on photo-absorption in the QDs, modifying the tunneling probability in the RTD and basic device architecture with quantum dots (QDs) embedded in the material [58, 59]. QDRTD has demonstrated single-photon detection efficiencies of up to 12% at 550 nm, low-jitter of 150 ns, low dark count rates ($< \times 10^{-2}$ Hz) and the best-reported figures of merit (FOM) [50]. However, no photon number resolution of this kind of RTD-photodetector has been accomplished. RTD photodetectors can be operated as low-noise and high-speed amplifiers of small

optically generated electrical signals [42]. It is exploited that the tunneling current is very susceptible to variations in the local electrostatic potential, which could allow the detection of single photogenerated charge carriers, consequently detecting single photons with the capability of photon-number resolution [60].

By modifying the layer materials to AlAs/InGaAs/AlAs, a much-extended detection wavelength of 1310 nm was reported [59], making the device available for telecommunication applications where the optical spectral range lies between 1310 and 1550 nm. Unfortunately, these devices succeed only at cryogenic temperatures (∼4 K), and practical detection efficiencies are low because of the micrometer-scale device areas [50]. However, improvements are predicted; for example, if noise sources can be eliminated, higher temperature operation may be possible. Also, resonant cavities could increase the device's efficiency. Furthermore, there is evident compatibility with III-V semiconductor QD single-photon sources [61].

The structure scheme and a simulation of the mechanism of single-photon trapped charges upon resonant tunneling processes in the energy band profiles are shown schematically in Figure 2.9 (a) and (b), respectively. The device comprises a photon absorption layer, an n-i-n semiconductor resonant tunneling diode in which the intrinsic region contains a layer of self-assembled quantum dots. Under illumination, the incident photons

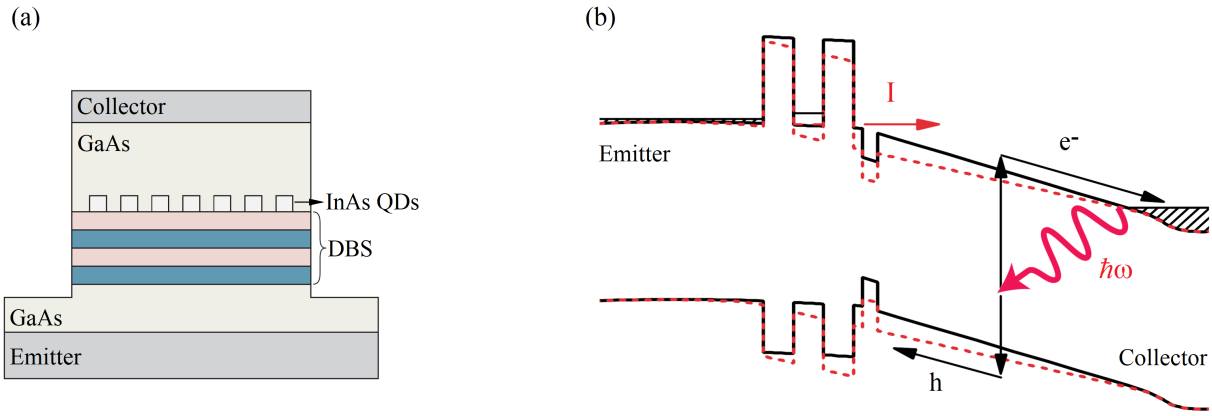

Figure 2.9: (a) Schematic of a QD-RTD single-photon detector array system. (b) Band profiles of the QD-RTD under a positively applied bias. In the dark (black line) and under illumination (red line), it is distorted after the absorption of photons (adapted from [58]).

can create electron-hole pairs in the collector region. These photo-generated holes subsequently flow into the resonant tunneling structure (RTS) and are trapped within the quantum dots. The trapped photo-generated holes reduce the local electrostatic potential in the region of the QDs, lowering the potential in the DBQW and thus altering the

transmission probability of electrons passing within the RTS. Under a positively applied bias, this can be measured as an increase in the current flow [58, 60].

Eventually, the resonant current can be effectively turned on/off by the incident photons. The current flowing through the device can be divided into two parts: the non-active QDs current and the charged QDs current. In the non-active, only RTS contributes, while in the active one, both RTS and QDs contribute. Under an applied negative bias, the QDs get negatively charged, so the potential of the QD is built up in the conduction band and no electrons from the emitter can tunnel through this DBS-QD path, which means that this channel is closed, designated as an "OFF" state. On the other hand, the photo-generated hole will drift towards the negatively charged QDs under an applied electric field, neutralizing the electron stored there and causing an observable resonant tunnel current through this channel; that is, these QDs are switched to an "ON" state by an incident photon. In this detection process, each negatively charged QDs functions as "single-photon switches" [49].

Chapter 3

Experimental methods

This chapter is divided into two parts: the first one will present the main fabrication procedure being the growth method, the structure of the studied samples, detailing layer thickness, composition and doping levels, as well as the processing techniques and device assemble (in the needed case). The second part will describe the optoelectronics experimental characterization techniques used throughout this work, outlining the main experimental setup, the confocal microscope, which was used for spectroscopic measurements as μ-photoluminescence (μ-PL) and electroluminescence (EL) associated with cryogenic and lasers systems in general, along with transport and photocurrent measurements setups.

3.1 Samples and growth

3.1.1 Molecular beam epitaxy (MBE)

MBE is a technique for growing thin (epitaxial) films with superior quality (compare with other growing techniques) of a diverseness of materials: from oxides to metals and semiconductors [62, 63]. However, the most usual use is to grow semiconductor compounds mainly due to a significant role in device processing with high technological value for the electronics industry, where it becomes crucial obtaining perfect and very pure semiconductor crystals with specific electrical properties without the need for processing steps involving the diffusion of impurities to produce doped layers. As its name implies, MBE uses beams of atoms or molecules that are in an ultra-high vacuum (UHV) chamber to provide the source of components on the growing process. These components will be incident in a heated crystal (substrate) with sufficient thermal energy to prevent them from migrating from the surface, and then they will begin to form a crystalline layer in the substrate; when the film grows perfectly ordered with the substrate that is an epitaxial film. If a film is grown on a substrate of the same material, the film is homoepitaxial, and if instead is grown on a substrate of a different material, the film is heteroepitaxial

[62, 64]. In principle, MBE is the ideal method for material preparation, considering that the arrangement can be custom-built, producing crystalline interfaces that are relatively atomically abrupt. Hence, it is possible to assemble a great range of structures, like quantum wells, quantum dots, superlattices, lasers, among others. All of which benefit from the precise control of composition during the growth [62]. The system is explained in Figure 3.1, essentially composed of two chambers, the main (growth) and load lock (preparation) chamber, which is connected through a valve.

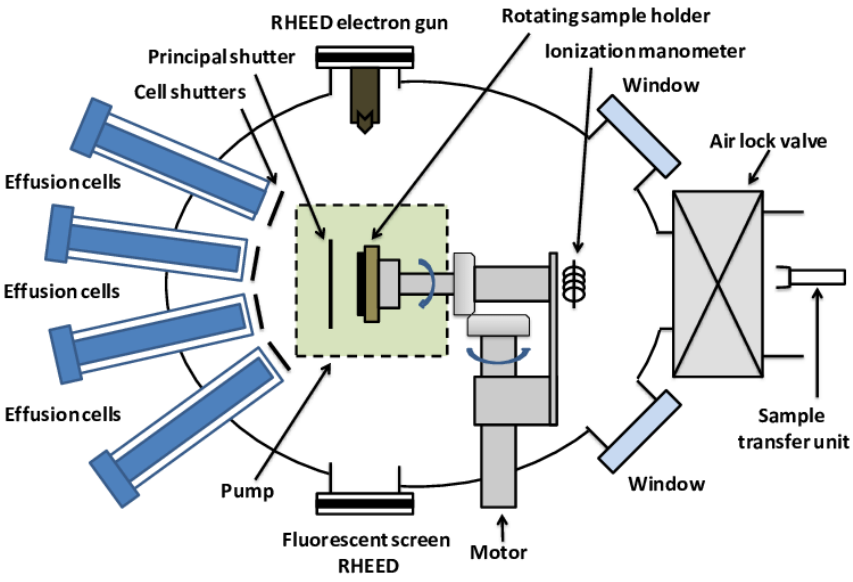

Figure 3.1: Schematic illustration of the main chamber of the MBE facility (adapted from [63]).

First, the substrates are processed to produce a nearly atomically clean surface and then brought into the load lock chamber. To reduce the danger of incorporating impurities in the load chamber, the pressure is reduced, and the substrate is placed on a heating station and heated up. Substrates processed this way can be transferred to the main chamber by a transfer pole and placed onto a manipulator that holds a rotatable plate with a heater underneath. The transferred substrates are placed on this plate. The pressure inside the main chamber is also reduced by a rotary vane pump (mechanical vacuum pumps that operate via positive rotary displacement) and a molecular turbopump. Final pressures are in the range of $\sim 1 \times 10^{-8}$ Torr. Connected to the main chamber are effusion cells and cracker cells from which the beam atoms and molecules travel in nearly collision-free paths until arriving either at the substrate or else at the chilled walls of the chamber. Incorporating them into the substrate takes place mainly at the steps and edges of it because there are possible binding partners. The temperature of the substrate must provide the atoms with sufficient kinetic energy for them to migrate and reach a binding

partner. Though, the temperature should not be too high because this leads to an increase in the desorption of atoms from the surface. Once the desired layer is formed, a shutter is interposed in the beam, and it turns off almost instantly, allowing the composition of the next layer to change very abruptly [34, 62, 64].

For all the samples grown in this work, an n-type crystalline GaAs substrate wafer at the temperature range of $570 - 580$ °C was employed. Group III elements such as Ga need a sufficient amount of As to find enough binding partners. If this is not the case, drops of pure Ga are formed. However, if too much As is provided, the migration duration is shortened, leading to random nucleation centers on the surface and undesirable rough surfaces. The available materials in the effusion cells are Gallium (Ga), Aluminium (Al), Indium (In) and Silicon (Si). For the As-based compounds, the n-type doping profile was produced using Si as the donor, and this was evaporated through temperatures up to 1200 °C. Additionally, there are shutters in front of those cells to regulate the effusion more precisely. The material in the cracker cell is As. In it, the As is sublimated by 400 °C and then guided inside the chamber through a valve. At the top of the cell is the so-called cracker area. There the As_4 molecules are cracked into dimer at a temperature of $800 - 1000$ °C [64]. This process increases the number of available reactants. Afterward, the beam of molecules moves along virtually collision-free paths continuously to spread at the substrate and grow as an epitaxial surface.

As will be described in the sequence, one of the studied samples was grown with a layer of quantum dots of InAs as the low bandgap semiconductor embedded in GaAs as the high bandgap semiconductor. Between the lattice constant of GaAs and InAs exists a mismatch of approximately 7 % [18]. This mismatch introduces strain in the lattice of InAs when it is deposited on GaAs. During this mode, a 2D film made out of InAs is formed, which is on average 1.5 monolayers thick [65]. This layer is referred to as the wetting layer (WL). Further deposition of InAs leads to the formation of QDs on the surface of GaAs. The size, shape, and density of the QDs are highly dependent on the growth parameters [34, 66]. For InAs, a substrate temperature of $510 - 525$ °C is an ideal range. The formation of QDs at a temperature of 520 °C is an almost instantaneous process ($\sim 2 \times 10^{-5}$ s), and their size is self-limiting. A common explanation is based on adatom (atom that lies on a crystal surface) aggregation. The vapor landing on the surface becomes adatoms immediately. They interact through short-range chemical exchange interaction and aggregate to QDs upon collision. According to this theory, the growth rate should be proportional to the number of adatoms and therefore proportional to the flux of the effusion cells. This would also explain the self-limiting growth because only the atoms from the original honeycomb lattice would be incorporated into the QD structure. InAs QDs in GaAs that are grown like this usually have an emission wavelength of $1000 - 1250$ nm [67]. Their emission wavelength can be shifted to lower values (by partial capping and annealing process)

around 900 nm where silicon detectors are more sensitive. In this step, the QDs get buried in a GaAs layer (capping layer) and then the substrate temperature is increased for the annealing process [34, 68].

3.1.2 Samples

All the samples studied in this work were grown by molecular beam epitaxy. The first one consists of a high-quality GaAs/AlGaAs quantum well system. The other samples consist of a set of three resonant tunneling diodes (RTDs), with minor differences in their structures in order to study the correspondent effect in their optoelectronic responses. The first RTD is a reference structure, the second one has a prewell layer adjacent to the double barrier and the third one has a layer of quantum dots. The RTDs underwent additional treatments to carry out transport measures in them. In the next section, this will be detailed appropriately.

The first one is a quantum-well (QW) system grown in the Institute of Physics at the University of São Paulo in a Gen II MBE system on epiready semi-insulating GaAs(001) substrate followed by a 1 μm-thick GaAs buffer layer, a 30×[$Al_{0.18}Ga_{0.82}As$(10 nm)/GaAs(5 nm)] superlattice. A schematic representation of the sample and the band structure (conduction and valence band edges) are represented in Table 3.1 and Figure 3.2, respectively. The quantum well main structure consisted of a 15 nm-wide GaAs quantum-well with 50 nm-thick $Al_{0.18}Ga_{0.82}As$ barriers completed with 2 nm-thick AlAs confinement layers on each side and a final 5 nm GaAs cap-layer. The structure was grown at 580 °C in order to decrease the amount of acceptor atoms inside the barriers [69].

Layer	Thickness (nm)	Material
Cap	5	GaAs
Confinement	2	AlAs
Barrier	50	AlGaAs
QW	15	GaAs
Barrier	50	AlGaAs
Confinement	2	AlAs
Substrate	–	GaAs

Table 3.1: Main layers description of the composition for the quantum-well system structure.

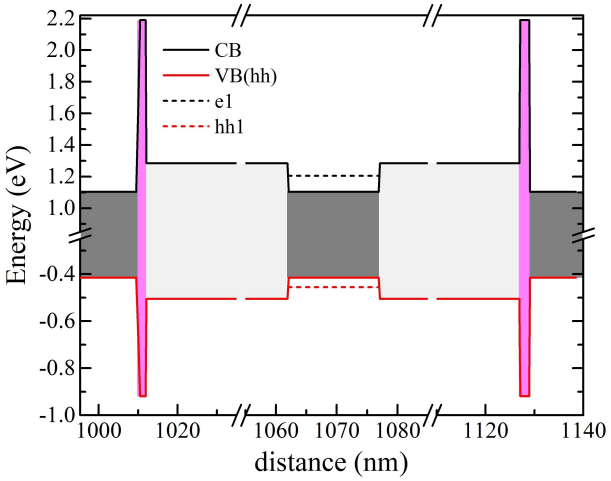

Figure 3.2: QW Conduction and valence band edges showing the first energy levels of electrons and holes, respectively.

The RTDs were developed at the Microstructure Laboratory (Gottfried-Landwehr-Laborfür Nanotechnologie, GLLN) at the Chair of Technical Physics (Technische Physik, TEP) from Universität Würzburg (Würzburg, Germany). All RTDs, in general, were grown on a silicon-doped GaAs substrate, which means that Si atoms are incorporated into the GaAs crystal structure in place of Ga atoms. Since silicon has an additional electron, this means that there are free electrons available. This is called the n-doping process, and the substrate is therefore n-type GaAs. Similarly, one can dope a material with an element that has fewer electrons leading to more positive charges and therefore called p-doping. Typically for the n-doping Si can be used, and for the p-doping beryllium (Be), Zinc (Zn) or carbon (C). The p-(n-)doping shifts the band gap-up (down), which leads to a tilt in the band structure.

Figure 3.3 shows the electron microscopy images (SEM) obtained for the first RTD, labeled as RTD-Ref throughout this document since it is used as a reference diode. Table 3.2 is presenting its composition, consisting of one first layer of 300 nm silicon-doped 3×10^{18}cm^3 n-GaAs buffer layer to minimize the surface roughness. Next to the buffer layer, a 100 nm layer of n-GaAs ranging from 3×10^{18} to 2×10^{17} cm^3 was grown, followed by an intrinsic region (not doped) with two i-GaAs layers of 20 nm thickness incorporating the double barrier or tunneling structure (DBS) between them. The AlGaAs barriers'

RTD-Ref	Thickness (nm)	Material	Doping(cm^{-3})
Cap	10	n-GaAs	3E18
Drain	250	i-$Al_{0.2}Ga_{0.8}As$	3E18
	50	i-$Al_{0.2}Ga_{0.8}As$	0.2E18
	100	n-GaAs	0.2E18
Tunneling Structure (intrinsic)	20	i-GaAs	–
	3.5	i-$Al_{0.6}Ga_{0.4}As$	–
	4	i-GaAs	–
	3,5	i-$Al_{0.6}Ga_{0.4}As$	–
	20	i-GaAs	–
Source	100	n-GaAs	3E18-0.2E18
Buffer	300	n-GaAs	3E18
Substrate		n-GaAs	-

Table 3.2: Two 3.5 nm $Al_{0.6}Ga_{0.4}As$ barriers, separated by a 4 nm layer of i-GaAs, forming the quantum well.

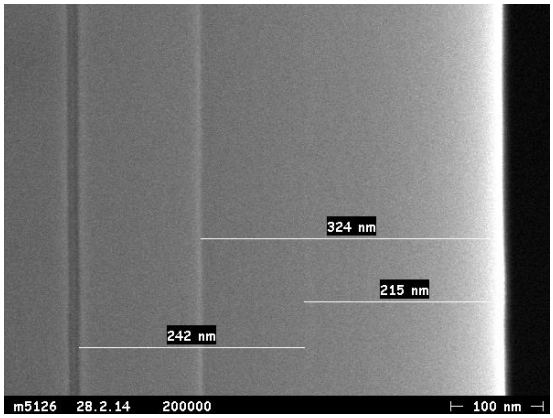

Figure 3.3: Cross-section scanning electron microscopy image of the RTD-Ref sample.

thicknesses (3.5 nm each) were chosen in a way that makes the tunneling of electrons possible while preventing the tunneling of holes. The quantum well (QW) between them consists of a 4 nm i-GaAs layer. On top of the DBS, the drain region starts with a layer of 100 nm of n-GaAs 0.2×10^{18} cm^3 followed by 300 nm of $Al_{0.2}Ga_{0.8}As$ also doped from

0.2×10^{18} to 3×10^{18} cm^3, and finally the covering (cap) layer of 10 nm of n-GaAs 3×10^{18} cm^3.

The second RTD composition is presented in Table 3.3 as well, as the SEM images obtained for this sample are shown in Figure 3.4. This RTD is labeled as RTD Prewell and starts with a 300 nm n-GaAs (3×10^{18}cm^3) buffer layer. Next, a 100 nm layer of n-GaAs from 3×10^{18} to 5×10^{17} cm^3 followed by an intrinsic region which initiates with 15 nm of an i-GaAs layer. A 5nm layer of i-$In_{0.15}Ga_{0.85}As$ forms the Prewell hence, before the DBS of AlGaAs equal to the RTD-Ref. The QW is 4 nm of i-$In_{0.15}Ga_{0.85}As$ layer. On top of the DBS, a 20 nm of i-GaAs layer, followed by 100 nm of n-GaAs (0.2×10^{18} cm^3) and a 300 nm layer of n-$Al_{0.2}Ga_{0.8}As$ also doped from 0.2×10^{18} to 3×10^{18} cm^3. Finally, the covering layer is a 10 nm n-GaAs (3×10^{18} cm^3).

RTD Prewell	Thickness (nm)	Material	Doping(cm^{-3})
Cap	10	n-GaAs	3E18
Drain	250	i-$Al_{0.2}Ga_{0.8}As$	3E18
	50	i-$Al_{0,2}Ga_{0,8}As$	0.2E18
	100	n-GaAs	0.2E18
Tunneling Structure (intrinsic)	20	i-GaAs	–
	3.5	i-$Al_{0.6}Ga_{0.4}As$	–
	4	i-$In_{0.15}Ga_{0.85}As$	–
	3,5	i-$Al_{0.6}Ga_{0.4}As$	–
	5	i-$In_{0.15}Ga_{0.85}As$	–
	15	i-GaAs	–
Source	100	n-GaAs	3E18-0.5E18
Buffer	300	n-GaAs	3E18
Substrate		n-GaAs	-

Table 3.3: A layer of 5 nm and 4 nm of i-$In_{0.15}Ga_{0.85}As$ was added forming the Prewell and the QW.

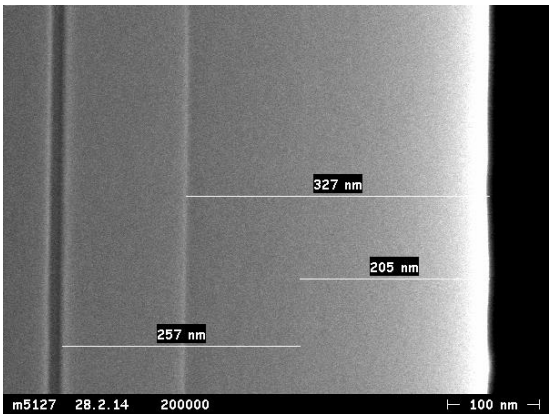

Figure 3.4: Cross-section scanning electron microscopy image of the RTD prewell sample.

The third RTD (labeled as RTD+QDs) is a set of three RTDs in which the two i-AlAs barriers were variated. Their composition is presented in Table 3.4 as well as the electron microscopy image (SEM) obtained for one of the RTDs and is shown in Figure 3.5. They are consisting of a buffer of 300 nm thickness silicon-doped 3×10^{18}cm^3 n-GaAs layer, followed by the source consisting of a 100 nm layer thickness of n-GaAs from 3×10^{18} to 5×10^{17} cm^3, followed by the intrinsic region initiating with 25 nm of an i-GaAs layer. The DBS is formed by two i-AlAs barriers of 1.5, 2.5 and 3.5 nm thickness with a 5 nm i-GaAs QW between them for all cases. After the DBS, a 2 nm layer of i-GaAs was grown before growing the quantum dots layer of i-InGaAs, and a layer of 25 nm of i-GaAs closes the intrinsic region. Next, a 75 nm of n-GaAs with a concentration of 0.2×10^{18} cm^3 followed by a 300 nm layer of n-$Al_{0.2}Ga_{0.8}As$ 3×10^{18} cm^3 doped, and finally, the covering layer consisting of 10 nm n-GaAs 3×10^{18} cm^3.

RTD + QDs	Thickness (nm)	Material	Doping(cm^{-3})
Cap	10	n-GaAs	3E18
Window	250	n-$Al_{0.2}Ga_{0.8}As$	3E18
Drain	75	n-GaAs	0.2E18
	25	i-GaAs	–
		$In_{0.075}Ga_{0.925}As$-QDs	–
	2	i-GaAs	–
Tunneling	1.5/2.5/3.5	i-AlAs	–
Structure	5	i-GaAs	–
(intrinsic)	1.5/2.5/3.5	i-AlAs	–
	25	i-GaAs	–
Source	100	n-GaAs	3E18-0.5E18
Buffer	300	n-GaAs	3E18
Substrate		n-GaAs	-

Table 3.4: Layers thickness are smaller than the reference one, and layer of InGaAs quantum dots was added after the DBS.

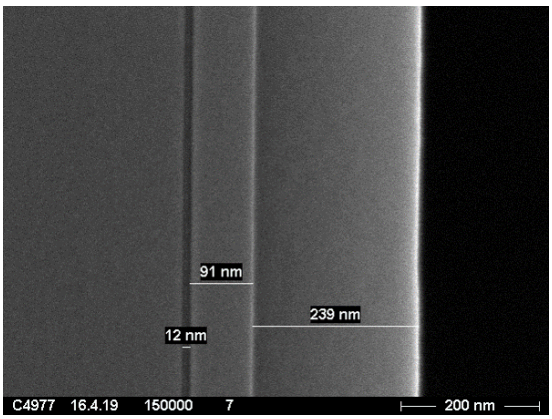

Figure 3.5: Cross-section scanning electron microscopy image of the RTD + QDs sample

3.1.3 Processing

The goal of the processing is to perform electro-optical characterizations on the grown of RTDs. For this, it is necessary to develop electrical contacts on top of them, in such a way that enables the extraction of optical and transport response when applying a varying voltage, and also to isolate the devices from each other to restrict the limits where the electric field is distributed in the sample. A way to do this is through the development of diodes with cylindrical tables and upper contacts. This contact is open (ring-like) for the optical response at the top of the diode (mesa). To obtain the best quality and to be able to make a statistical study, a matrix with several devices of varying diameters is manufactured with mesas of twelve different diameters from 2 to 13 μm (nominal values).

For this purpose, the sample has to go through several processing steps, most of them illustrated in Figure 3.6. First, a 10×10 mm piece is cleaved out of the wafer where the heterostructure was grown. Then, using the spin-coating technique, which consists of adding a drop of material in the center of the sample and bringing it under a high rotation, spreads uniformly over the entire surface, the wafer is covered with a thin layer of photoresist. The photoresist is a light-sensitive material used in photolithography to form a coating pattern on a surface when exposed to light and covered with an optical mask (Figure 3.6 (a)). Afterward, the sample is exposed to ultra-violet light with the mask in the shape of mesas with different diameters (Figure 3.6 (b)), and then, the developer removes the soluble part leaving only the part of the structure revealed (Figure 3.6 (c)). Then, using chemical reactions from plasmas, a dry chemical attack is made to remove the regions not protected by the photoresist, leaving only the cylindrical shapes as shown in Figure 3.6 (d). This removal must have a depth that reaches the double barrier to

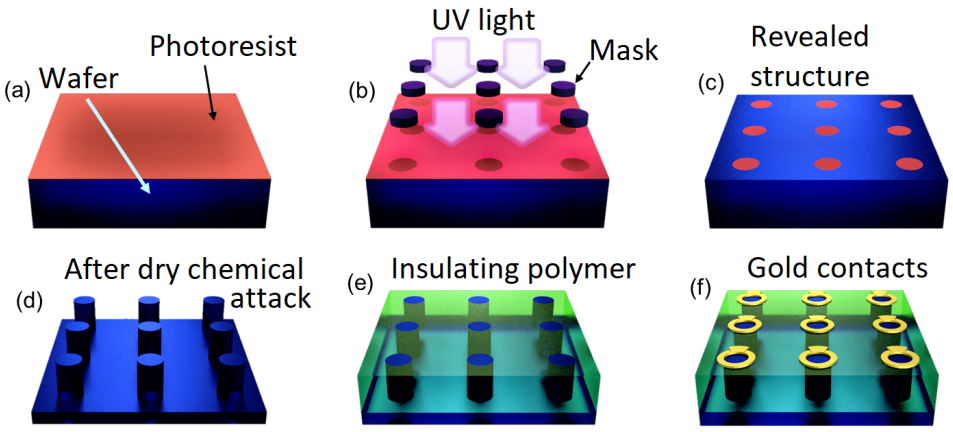

Figure 3.6: Schematic representation of RTD microfabrication processes. (a) Deposition of photoresist on the RTD wafer. (b) Incidence of ultraviolet radiation using an optical mask to protect the desired area. (c) Revealed of the pattern formed by the mask. (d) Dry chemical attack removes not protected structural composition. (e) Leveling the cylindrical structures with an insulating material. (f) Gold contacts are evaporated through optical lithography techniques.

guarantee that all the active layers of the device are located inside the cylindrical mesa only. Next, benzocyclobutene (BCB) is spin-coated onto the mesas structures to isolate and leveled them up and also to facilitate the deposition of the contacts (Figure 3.6 (e)). The sample is then heated up to 210 °C for 2 hours in a nitrogen environment to prevent oxidation on the surfaces. In this baking step, the BCB hardens and drys, so the sample is now bound together. After that, the optical lithography technique is used to form the patterns and deposit (via sputtering) the ring contacts for each mesa (Figure 3.6 (f)). After depositing the contacts, the last step is to fix the sample on the gold metallic base of the chip carrier using silver paint, and by micro-welding, the RTDs' ring contacts are connected to the chip-carrier. This step must be carried out with high precision to obtain the best possible adhesion and electrical and thermal conduction to the RTDs and the most reliable transport results. The ground contact is made by the silver paint itself, as the metallic base extends to the responsible terminal grounding.

3.2 Optoelectronics characterization techniques

This section will present the theoretical basis of the primary measurement techniques used to characterize the samples during this thesis, like photoluminescence and electroluminescence at low temperature via confocal microscopy technique. Different configurations were employed to perform these techniques, i.e., depending on the temperature and external

electric or magnetic fields; depending on the phenomenon under study. Since all the optical characterizations were carried out with a confocal microscope associated with a cryostat, this technique will be described in detail.

3.2.1 Confocal microscope

Marvin Minsky first faced the confocal principle in the 1950s as he tried to visualize the way nerve cells were connected in the human nervous system [70]. He ventured to obtain an image free from out-of-focus information from the surrounding planes. What he proposed was to illuminate only one part of the sample at a time, and exclude all rays not initially aimed at the focal point of the sample, and using a second channel to image a pinhole aperture on a single point on the other side of the objective, rejecting the out-of-focus light [71, 72]. Subsequent improvements utilize a laser and scan the laser beam rather than translating the sample [71]. These two improvements allowed confocal microscopy to become a powerful tool for many scientific fields, such as biology, medicine, and materials science. In the latter one, the primary use is in the reflection mode and with methods such as light polarization [73]. A cross-polarized configuration of a confocal microscope can suppress a high amount of excitation to detect single emissions at the same wavelength from the probe. Then is possible only to collect in-focus single quantum dot luminescence, transitions, and bi-excitation with resonant excitation [74]. This allows for more research into quantum information processing. It is even widely used in industry, for example, facilitating the detection of defects in semiconductor circuits [73].

Figure 3.7 shows the schematic configuration consisting of a laser as a light source, which is collimated, then passes the beam splitter (BS), and then focused on the sample at a focal plane with the objective lens. Only the Backscattered light from the focal point will be imaged on the detector after the pinhole. The aperture of the pinhole will block light from other planes (dash lines). In the confocal system, the excitation and detection address the same focal plane.

Similar to a standard light microscope, the resolution of the confocal microscope is limited by the diffraction of light. The image of an ideal point seen through a circular aperture is blurred, and the diffracted image is known as an Airy disk. The Airy disk radius (R_{airy}) depends on the incident laser wavelength (λ) and the objective lens numerical aperture (NA), $R_{airy} = 1.22\lambda/2NA$ [73].

In our setup, we have a fiber-coupled configuration. Thus, the whole microscope is built using a Thorlabs cage system instead of an optical table. In this matter, we use optical fibers to the excitation source as well as to the detection setup. Therefore, the collection optical fiber's core (in which we focalize the output PL) acts as the pinhole,

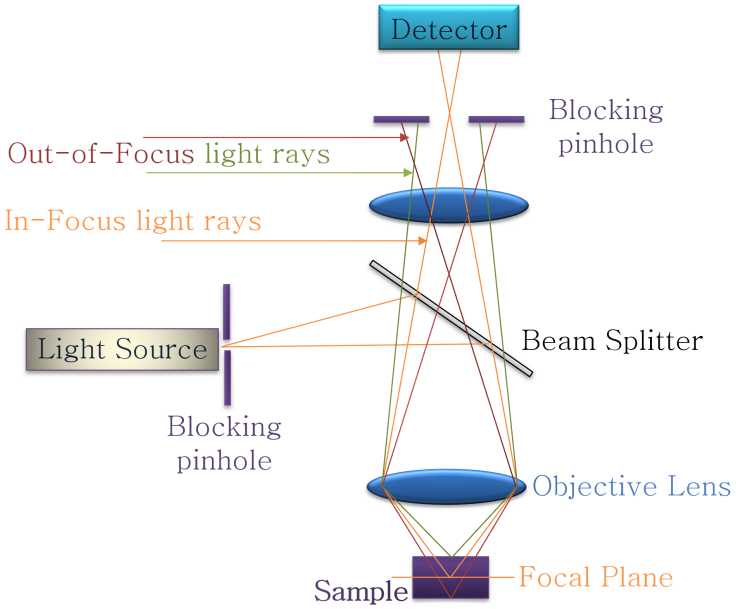

Figure 3.7: Schematic representation of the confocal microscope arrangement.

and only the light within its numerical aperture is captured. Besides, the excitation fiber works with a collimated beam ensuring a single point source. All this increases the efficiency of both excitation and collection. For this reason, the spectroscopy experiments with the confocal microscope guarantee the maximum collection of the emitted light.

3.2.2 Setup

The main experimental configuration used to perform the measurements in this work is around a magneto-cryostat with a closed-loop helium system of ultra-low vibration built by Attocube (attoDRY1000). This cryogenic system operates at low temperatures of 3.6 K in the sample region and 3.2 K in the superconducting coil that allows the application of magnetic fields up to 9 T. Special care has been taken to minimize the vibrations due to the pulse tube cold head and decoupling of the sample space from the rest of the system.

An overview of the setup, including the cryostat and the spectrometer, is presented in Figure 3.8. The confocal microscope stick that is compatible with extreme environments of temperature, pressure, and magnetic fields, is inserted in the cryostat (represented by dashed lines). At one extreme of the microscope's stick is a titanium module where the sample is placed. This module contains a set of electronically controlled piezoelectric nanopositioners with degrees of freedom in the x, y, and z axes that allow the positioning of the sample with a precision of 10 nm. The sample is focused with an objective lens of a high numerical aperture value using the piezoelectric positioners. This assures focusing

and collecting with efficiency for both excitation light and the luminescence emitted by the sample, respectively. Another feature to highlight is that when the sample is inserted into the cryostat, it is located in the center of the superconducting coils, where the magnetic field region is uniform. For the measurements made in this work, the sample was placed in the Faraday geometry; that is, the direction of growth of the sample is parallel to the lines of the applied magnetic field.

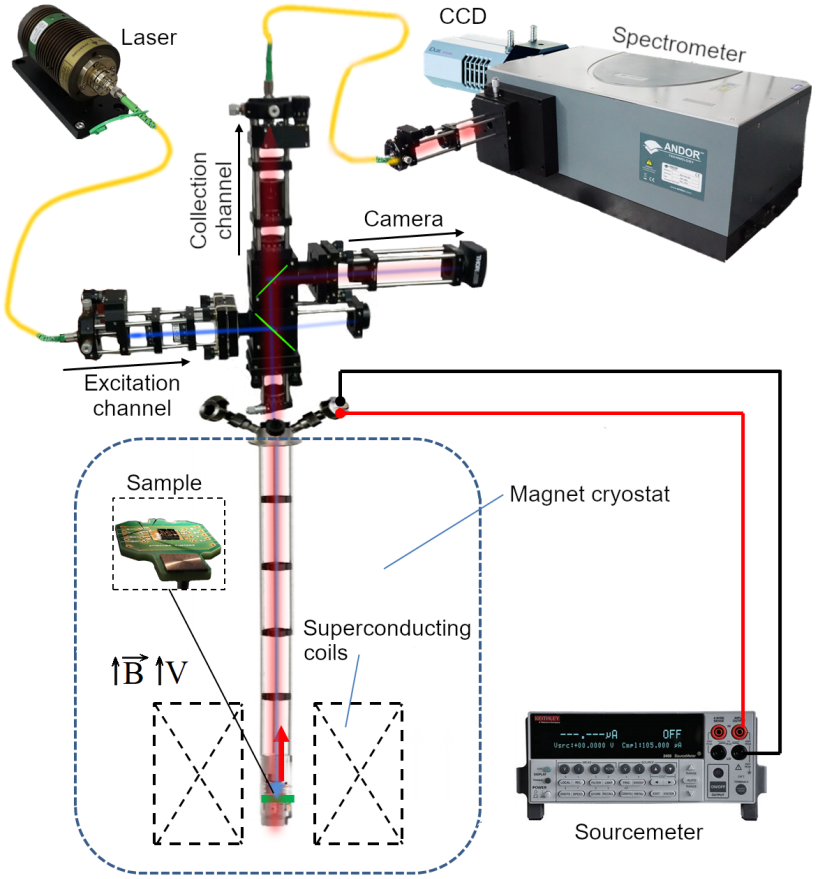

Figure 3.8: Schematic representation of the experimental setup used during this work, particularly for the electroluminescence and photoluminescence measurements (adapated from [75]).

For the PL measurements, several lasers were available, from the ultraviolet to the near-infrared, and the detection system is sensitive in low and high resolution through a 75 cm spectrometer with different diffraction grids and a high-resolution detector CCD (Silicon). For electroluminescence and transport measurements, a voltage source with a sensitivity up to nano ampere was used. The optics required for excitation and collection of the emitted light and the filters for polarization study are aligned in the external region. All the features for each experience will be described in detail in the following subsection.

Polarization and optical alignment

In this thesis, the study of the polarization properties of the photoluminescence of quantum structures was of interest. In this sense, understanding and controlling the polarization is crucial for various reasons, mainly to be able to perform and obtain reliable performance in polarization-based experiments. Characteristics such as reflectivity, insertion loss, and beam splitter ratios will differ for excitation and collection beam paths. As mentioned before, our setup uses a fiber-coupled configuration. Unfortunately, this has some disadvantages. First, single-mode fiber does not maintain any polarization. Therefore, it is impossible to transfer fiber-coupled polarized light to a spectrometer without losing some degree of polarization. Second, the spatial coupling in the fiber can be lost through a microscopic rotation of the optical elements. Since there are several optical elements in the microscope head, it is necessary to calibrate any influence on the polarization of each optical element.

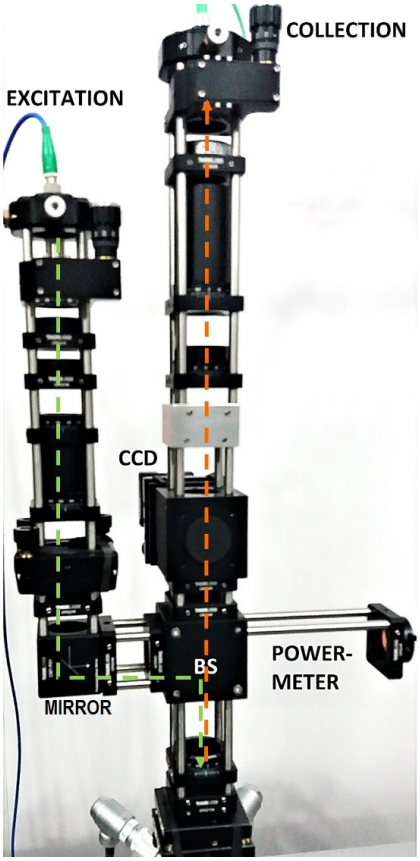

Figure 3.9: Photograph of the head of the confocal microscope with the main optical components and the different light paths. The green dashed line represent the excitation path and the red dashed line with arrow represent the detection path that is sent into one of the detection fiber.

In the experimental setup, the head of the confocal microscope is divided into three channels: excitation, detection, and inspection. All are interconnected with each other by the central microscope body. As in the confocal microscopy technique, all the optical paths (excitation and detection) go through the same optical objective and must be anti-parallel; using two BS in the center of the microscope for beam combination is essential. The first one in the excitation path uses an optical quartz window that reflects 8% of the S-polarization of the incident light and transmits 92% of the light emitted by the sample. The second one is placed with alignment purpose on top of the first; this makes the reflection of the excitation and the collection beams visualized on a CCD camera. The BS's reflection and transmission depend on whether the light is polarized parallel to the s or the p axis to the first BS.

The optical path is described in Figure 3.9. The excitation channel starts from the laser source coupled to a polarization-maintaining single-mode optical fiber. An aspherical lens collimates the laser beam with a diameter of 5 mm to match the clear aperture of the objective inside the cryostat (this lens has a numerical aperture of 0.64 and a focal length of 1.6 mm). The linearly polarized (excitation) light crosses first a polarizer to ensure that the beam will be linearly polarized and then a half-wave plate that rotates the polarization in 2θ, this is, to align the polarization of the incoming light concerning the polarizer axis, so we can ensure that the laser polarization is aligned to the S axis of the beamsplitter. Hence, (S) polarized light is sent to the sample (depending on this alignment, the transmitted power will change, as the polarizer will only allow the component of light polarized along its polarization axis to go through).

When the sample is excited by polarization S, the emitted PL signal will combine S and P components. The collimated emitted beam passes through the same objective and collimated, then crosses two beamsplitters rotated by $\pi/2$ one respectively to the other. In this way, the S and P axis are inverted, and their influences on the polarization effects neutralize each other. In the detection path, a quarter-wave plate is positioned at $\pi/4$ degrees in relation to S and P; that is, it will convert the linear light emitted by the sample into a circular one, generating $\sigma+$ and $\sigma-$ components. Then a linear polarizer allows analyzing the beam polarisation and will define the $\sigma+$ and $\sigma-$ directions based on the variation of the transmitted intensity with the wave-plates respective orientation. Finally, luminescence is focused on the collection of optical fiber to be sent into the detection setup, which is the spectrometer coupled to a highly sensitive CCD camera.

3.2.3 Photoluminescence

In general, PL consists of light emission after the absorption of photons. In semiconductors and if the energy involved is sufficient, the absorption of photons causes excitation of electrons from the valence band to the conduction band, leaving holes in the valence band; both electrons and holes can remain in a bonded state under Coulomb attraction, interacting and moving through the crystalline lattice as quasiparticles with a neutral charge, called an exciton. Excitons can then move around the lattice without transporting liquid charge providing the origin to the conduction of carriers in semiconductors, in periods that are usually in the order of nanoseconds, interval after which excitons may recombine emitting a photon of equivalent energy to the semiconductor state [76].

The photoluminescence phenomenon consists of three main processes: Excitation, associated with the generation of electron-hole pairs; thermalization, related to the relaxation of the system to thermal equilibrium conditions; and finally recombination, in which the thermalized electron-hole pairs recombine, thus producing luminescence. The photoluminescence technique consists of measuring the radioactive recombination channels of the electron-hole pair generated in the excitation through incident light on the sample. It is a non-destructive technique that does not require special preparation of the samples and allows the study of optical properties as a function of different parameters such as temperature, excitation intensity, external magnetic and electric fields. The emission spectrum provides information that allows identifying impurities, disorders in the composition of alloys, energy gaps, interface roughness, discrete energy levels, among others.

3.2.4 Electroluminescence

Like photoluminescence, electroluminescence consists of the excitation of electrons from the valence band to the conduction band, generating electron-hole pairs that interact and recombine in regions of minimal potential and emitting light. The difference is that the initial excitation, in this case, is an electric field that accelerates electrons and holes in opposite directions, allowing them to recombine in regions where the potential energy is the lowest.

EL processes have been observed in different RTD structures with doped compositions of opposite signals at heterostructure ends. However, electroluminescence (EL) in type-n tunneling structures due to the radioactive recombination of holes produced by impact ionization in high electric fields is rarely observed and appears particularly in low-dimension systems, such as quantum wells and super-lattices. When the applied voltage is sufficient to inject electrons into the non-doped region and obtain energy greater than

approx 1.5 times the band-gap, the electrons can initiate the impact ionization process, leading to the production of the electron-hole pair. The holes generated by ionization return to the strongly doped upper contact, where they recombine and produce electroluminescence [42–45]. Ideally, the absolute intensity of EL (number of photons emitted per second) should be equal to the number of holes generated per second due to ionization, assuming that the holes are generated due to each impact. Thus, the measurement of the EL intensity may provide the number of impact ionization events occurring per second [77].

3.2.5 Electrical measurements

The Semiconductor Nanostructure Group (GNS in Portuguese) from the Universidade Federal de São Carlos has a software that enables total control of all possible measures and parameters for each experiment. In this program, the application of an electric field with a real-time construction of the current facilitates obtaining the transport measurements. That is the reading of the electric current as a consequence of an applied voltage. In the RTDs, the contacts are organized in such a way that the direct voltage causes the electrons to move from the emitting contact located in the substrate to the top collector contact. As the direction in which the voltage is applied can influence the electrical response, the measurements were made varying in both directions, forward bias up to a certain value and down to zero again. In some cases, reverse bias experiments were performed as well; completing this cycle, the I×V curve is obtained. Different I×V studies were made, for example, with different resistances associated in series with the RTDs, as a function of temperature and under an applied magnetic and electric field, the last one is conjugated with the electroluminescence measurements discussed above.

Chapter 4

Quantum well

This chapter will present a comprehensive experimental and theoretical magneto-optical study of the behavior of the excitonic transitions, the energy and the spin structure observed in excitonic complexes of a GaAs/AlGaAs quantum-well (QW). The studies were carried out as a function of the excitation intensity, temperature and external applied magnetic fields. The type of resident carriers (holes or electrons) in the QW was controlled optically by above energy barrier illumination, permitting a direct comparison of positively ($\sigma+$) versus negatively (σ-) circular polarization of luminescence emissions.

4.1 Background

The optical properties of confined electron-hole complexes (excitonic quasiparticles) in high-quality GaAs/AlGaAs quantum-wells have been the subject of large studies since they dominate the optical spectra of semiconductors close to the band-gap. The relevant feature is that the exciton complex motion is close to the two-dimensional limit, resulting in an enhancement (up to a factor of 4 compared with bulk) of the excitonic binding energy due to an increased electron-hole wave-function overlap [20].

In spite of many investigations on exciton complexes and their recombination in undoped quantum wells [16, 78–80], the mechanisms driving these dynamics and the identification of the contribution of each complex are still controversial. For instance, the photoluminescence peak sometimes observed at the lower energy side of the neutral exciton emission ($0.6 - 1$ meV) has been ambiguously attributed to either biexciton or trion recombinations [16, 78–88]. In Ref. [79], a series of undoped GaAs/AlGaAs QWs with different widths showed a PL line around 0.7 meV below the excitonic emission with σ^- polarization that was ascribed to positive trions (X^+), where the excess of charges would come from unavoidable background concentration in the barriers or, for doped samples due to the influence of possible ionized donors/acceptors [79, 80]. In contrast, due to

similarities of the binding and excitation energies and their behavior as a function of temperature, other works have also described this transition as resulting from biexcitons [83–88].

The present chapter addresses the duality of the interpretations of the nature of this excitonic emission by providing an analysis of the binding energies and the interplay of the spin relaxation process of excitons, biexcitons, and trions determined experimentally by polarization-resolved photoluminescence and magnetospectroscopy. These findings are explained in terms of an effective analysis of population evolution via rate equations that includes creation, recombination, and scattering between different spin-resolved exciton complexes.

Figure 4.1 (a) shows an illustrative representation of the studied QW and Figure 4.1 (b) shows a diagram of the band structure with the conduction and valence band edges profiles and the first energetic positions of the quantum levels E_{e1} for electrons and E_{hh1} for heavy holes involved in the observed optical transitions for exciton (X^0), biexciton (XX) and negative trion (X^-).

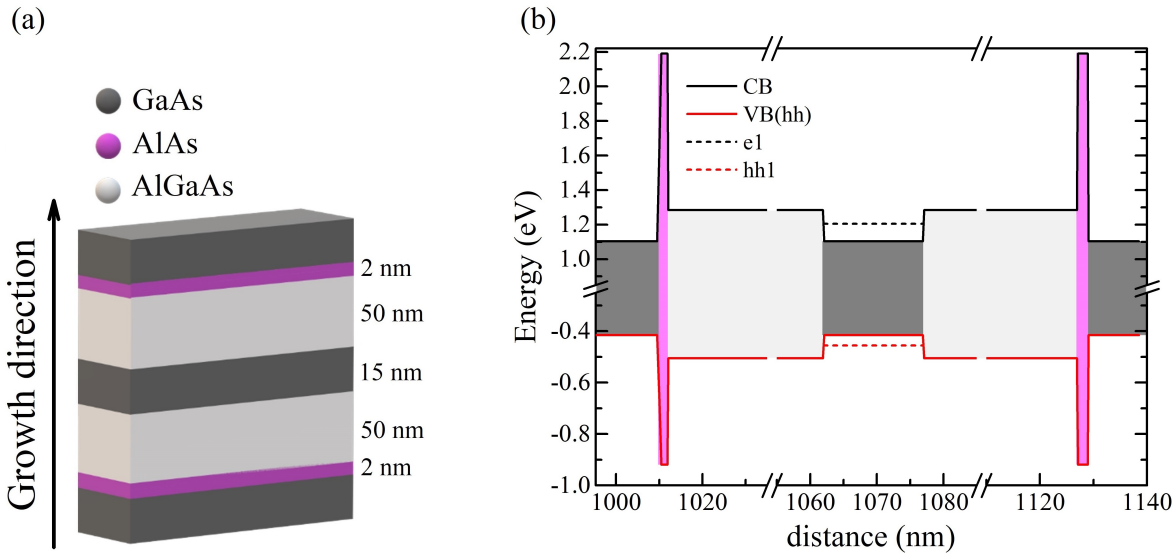

Figure 4.1: (a) Schematic illustration of the quantum well system structure. (b) Conduction (CB) and valence bands (VB) profiles of the QW with the first energetic position of the quantum levels E_{e1} and E_{hh1}, for electrons and for holes, respectively.

4.1.1 Theoretical framework

To interpret the possible exciton recombination, a theoretical framework is considered [89] in which exciton, biexciton, and trion populations are intertwined through a set of rate

equations. The exciton dynamics can be described by

$$\frac{dn^{\pm}_{X_0}}{dt} = P^{\pm}_{X_0} - \frac{n^{\pm}_{X_0}}{\tau_x} - F^{\pm}_{XX} - F^{\pm}_{X^-} \mp Z(X_0), \tag{4.1}$$

where P_{X_0} is the excitons density. Equation 4.1 corresponds to an exciton generation rate with a given spin, $P^{\pm}_{X_0}$, determined by the incident-light polarization. The exciton decay rate

$$\frac{1}{\tau_x} = \frac{1}{\tau_{r,X_0}} + \frac{D(E_{X_0})}{\tau_{nr,X_0}}, \tag{4.2}$$

combines the optical recombination, characterized by τ_{r,X_0}, and the nonradiative activation time, τ_{nr,X_0}, weighted by the thermal factor, $D(E_{X_0}) = \exp(-E_{X_0}/k_BT)$, with $E_{X_0} > 0$ being the exciton activation energy. The term $F^{\pm}_{XX} = 2\frac{(n^{\pm}_{X_0})^2}{\tau_\beta} - \frac{n^{\pm}_{XX}}{\tau_{r,XX}}$ correlates the exciton and biexciton densities, $n^{\pm}_{XX}$, by assuming that the biexciton population is proportional to the square of the exciton concentration, as expected at thermal equilibrium. Here $\tau_{r,XX}$ is the biexciton recombination time, and $1/\tau_\beta$ the biexciton formation rate. The penultimate term in Eq. (4.1), $F^{\pm}_{X^-} = \frac{n^{\pm}_{X_0}}{\tau_t} - \frac{D(E_t)}{\tau_t}$, sets the link with the trion dynamics by introducing a formation rate, $1/\tau_t$. According to this model, the biexciton density evolution can be characterized by the expression

$$\frac{dn^{\pm}_{XX}}{dt} = P^{\pm}_{XX} + F^{\pm}_{XX} - \frac{n^{\pm}_{XX}}{\tau_{nr,XX}} D(E_{XX}) \mp Z(XX), \tag{4.3}$$

that contemplates a direct biexciton generation, $P^{\pm}_{XX}$, and a nonradiative dissociation rate, $\tau_{nr,XX}$, with a nonradiative activation energy, E_{XX}. In turn, the trion equation is given by

$$\frac{dn^{\pm}_{X^-}}{dt} = F^{\pm}_{X^-} - \frac{n^{\pm}_{X^-}}{\tau_{r,X^-}} \mp Z(X^-). \tag{4.4}$$

The terms $Z(Y)$ that appear in Eqs. (4.1 - 4.4) account for the spin thermalization between Zeeman split states with energies E^+_Y and E^-_Y at finite magnetic fields, and are defined as

$$Z(Y) = \frac{n^+_Y}{\tau^s_Y} F(E^-_Y - E^+_Y) - \frac{n^-_Y}{\tau^s_Y} F(E^+_Y - E^-_Y), \tag{4.5}$$

where τ^s_Y is the spin-flip time of the corresponding excitonic complex, and

$$F(x) = \begin{cases} D(x)\ ; & x \geq 0\ , \\ 1\ ; & x < 0\ . \end{cases} \tag{4.6}$$

This definition allows intralevel Zeeman states to change their relative positions by varying the magnetic field. The stationary condition can be simulated by setting the left-hand side of the rate equations equal to zero.

4.2 Photoluminescence spectra

4.2.1 Temperature dependence

Figure 4.2(a) displays the photoluminescence spectra corresponding to the GaAs/AlGaAs quantum-well emissions as a function of increasing temperature for a fixed laser power of 1μW using a 730 nm laser and without magnetic field. Three peaks have been identified. The first two overlapping peaks in the spectra around 1.5328 and 1.5316 eV have been ascribed to the biexciton (XX) and the exciton (X^0) emissions, respectively, and a low-intensity peak at 1.539 eV to the band to band (e-hh) emission. Figure 4.2(b) and (c) shows the peak position of all the observed emissions and the corresponding PL integrated area of each peak as a function of the inverse of temperature ($1/(k_BT)$), respectively (values obtained from the deconvolution of the PL spectra).

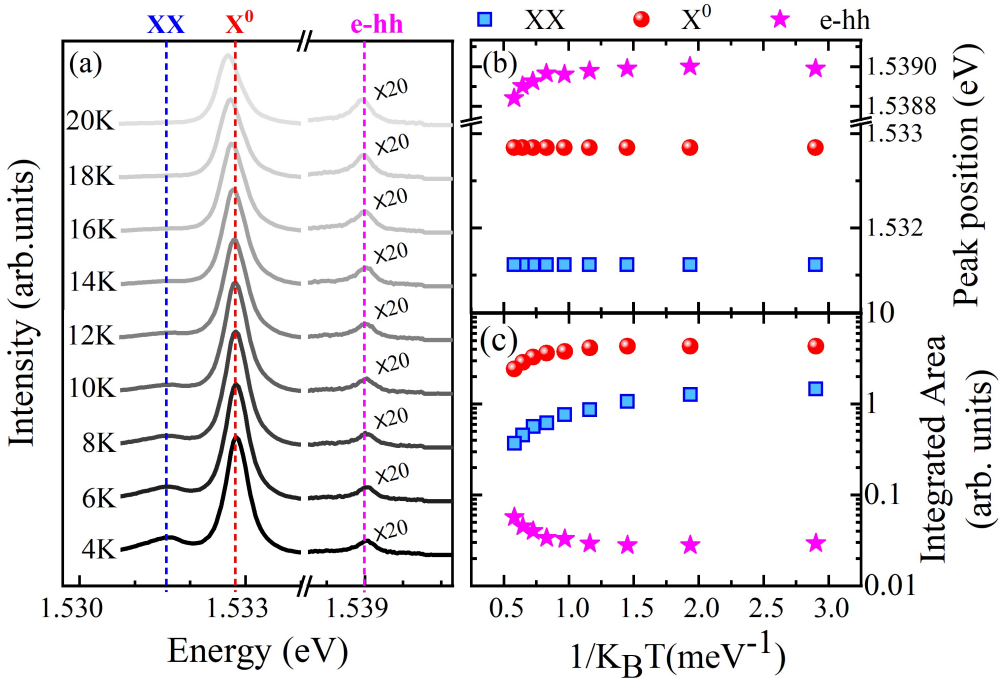

Figure 4.2: (a) Photoluminescence spectra of the quantum well emissions at $B = 0$ T as a function of temperature and with a laser power of 1μW. Verticals pink, red and blue dashed lines represent e-hh, X^0 and XX emissions, respectively. (b) and (c) Peak position and integrated area as a function of the inverse of temperature $1/(k_BT)$ for e-hh (pink stars), X^0 (red spheres) and XX (blue squares) emissions, respectively.

As can be seen from the Figure 4.2(b), exciton and biexciton peaks exhibit a difference in energy of $\approx$ 1.2 meV which corresponds to the biexciton binding energy E_b^{XX}. According to the literature, biexcitons have binding energy between (1.0 - 1.5 meV) for GaAs QW in similar conditions [86, 87, 90, 91]. With this relatively small binding energy, biexcitons are essentially observed at low temperatures. The increase in the temperature

causes dissociation of the biexcitons due to the increase in thermal excitation and their intensity tends to decrease more rapidly than that of the excitons emissions. The fact that the two of them are overlapping in the spectra requires detailed analysis to distinguish both emissions. From Figure 4.2(c) it is clear that their emission intensities decrease with rising temperature. However, the temperature range is not complete to determine a comprehensive temperature-dependence. Studies with the range up to room-temperature have shown a redshift of GaAs QW emissions when the temperature is increased [92]. However, as can be seen in Figure 4.2(a), the emission attributed to the biexciton recombination disappears at 20 K, and since the temperature dependence of the exciton recombination is well established, we focus our analysis just in this narrow temperature window. Figure 4.3 presents a detailed analysis of the experimental data with the aim of further investigation of the nature of the low-energy peak.

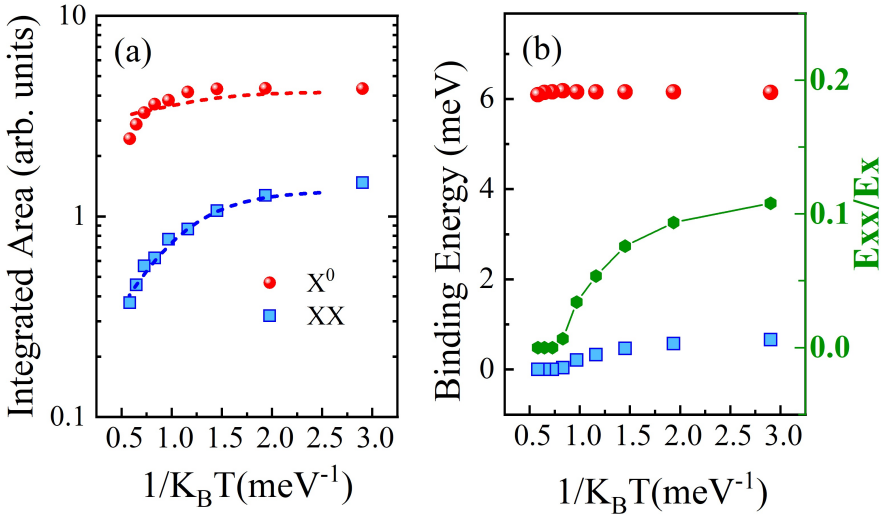

Figure 4.3: (a) Integrated area of the biexciton (blue squares) and exciton (red circles) emissions. The dashed lines represent the best fit. (b) Exciton and biexciton binding energies. Right-green side, ratio of the biexciton to exciton binding energy.

The evolution of the PL-Integrated area as a function of the inverse of temperature $(1/(k_BT))$ is fitted according to the theoretical description of the exciton dynamics and shown in Figure 4.3(a), where is neglected the spin index due to the spin degeneracy of the excitonic states in the absence of magnetic field. Figure 4.3(b) shows the exciton binding energy $E_b^X \approx 6$ meV and the biexciton binding energy $E_b^{XX} \approx 0.9$ meV and the ratio of the biexciton to exciton binding energy E_{XX}/E_X as a function of the inverse of temperature $1/(k_BT)$ obtained from the PL peak position.

Solving the coupled Eqs. (4.2) and (4.3) for the steady-state, we obtained the PL intensities of the exciton and biexciton emissions as $I_{X_0} = n_{X_0}/\tau_{r,X_0}$ and $I_{XX} = n_{XX}/\tau_{r,XX}$, respectively. We have used $P^+_{XX(X_0)} = P^-_{XX(X_0)}$ to describe a linearly polarized laser light

without considering the trion contribution, since this state will only appears in the presence of a magnetic field. For the sake of simplicity, it was set τ_{r,X_0}=$\tau_{r,XX}$=1 ps. The other parameters were obtained by fitting the experimental data (dotted lines in Figure 4.3(a)).

The coupling of exciton and biexciton dynamics makes the simultaneous fitting of both X^0 and XX data an intricate task. However, a good qualitative agreement with the following values have been found: $\tau_{nr,X_0} = 1.09363$ ps, $\tau_{nr,XX} = 0.104407$ ps, $E_{XX} = 2.4$ meV, $E_{X_0} = 8.5$ meV, $P_{X_0} = 2.8$ kW/cm^2, $P_{XX} = 1.3$ kW/cm^2, and $1/\tau_\beta = 0.00007$ ps^{-1}. Note that the transition rate of non-radiative processes for biexcitons is an order of magnitude larger than for excitons. Furthermore, excitons are mainly photocreated, while the formation rate of biexcitons from exciton states is negligibly small, i.e., the biexciton formation is almost instantaneous and does not result from a two steps process. The formation of secondary biexcitons has also been disregarded in Ref. [85], since the quasi-equilibrium between the exciton and biexciton populations is not established. The large value of τ_β indicates that the biexciton dynamics may be decoupled from the other excitonic complexes.

4.2.2 Power dependence

Figure 4.4(a) shows the photoluminescence emissions of GaAs/AlGaAs QW depending on the incident laser power. These measurements were carry out using a laser wavelength of 440 nm, at a fixed temperature of 10 K, and collected for different laser powers ranging from ∼10 nW to ∼0.1 mW. Figure. 4.4(b) displays the exciton and biexciton binding energies $E_b^{X^0}$ and E_b^{XX}, respectively.

For the exciton binding energy ($E_b^{X^0}$), it was calculated as the difference between the bandgap energy ($e - hh$) and the bound exciton energy X^0. The biexciton binding energy (E_b^{XX}) as the energy difference between the X^0 and the biexciton energy XX states taken from the PL peak position, as a function of laser power. Figure 4.4(c) presents the integrated PL intensity behavior as a function of laser power. Turning to these experimental results, it was also found three peaks and ascribed to the band-to-band close to 1.541 meV (not shown), the single exciton (X^0), and the biexciton (XX) emissions. The evolution of the last two when increasing power is opposite to that obtained with rising temperature. With the increase in the excitation power, the population of excitons in the semiconductor grows linearly, promoting the formation of biexcitons, which grow in a super-linear manner [86, 87, 90, 91]. Therefore, the peak associated with biexciton emissions grows strongly with increasing excitation power, while the one associated with exciton grows less intensely. At low excitation power, the XX peak is less intense than the X^0 peak. With the increase in power, XX grows more strongly than X^0 and at ≈30 μW an inversion in intensity occurs between these two peaks.

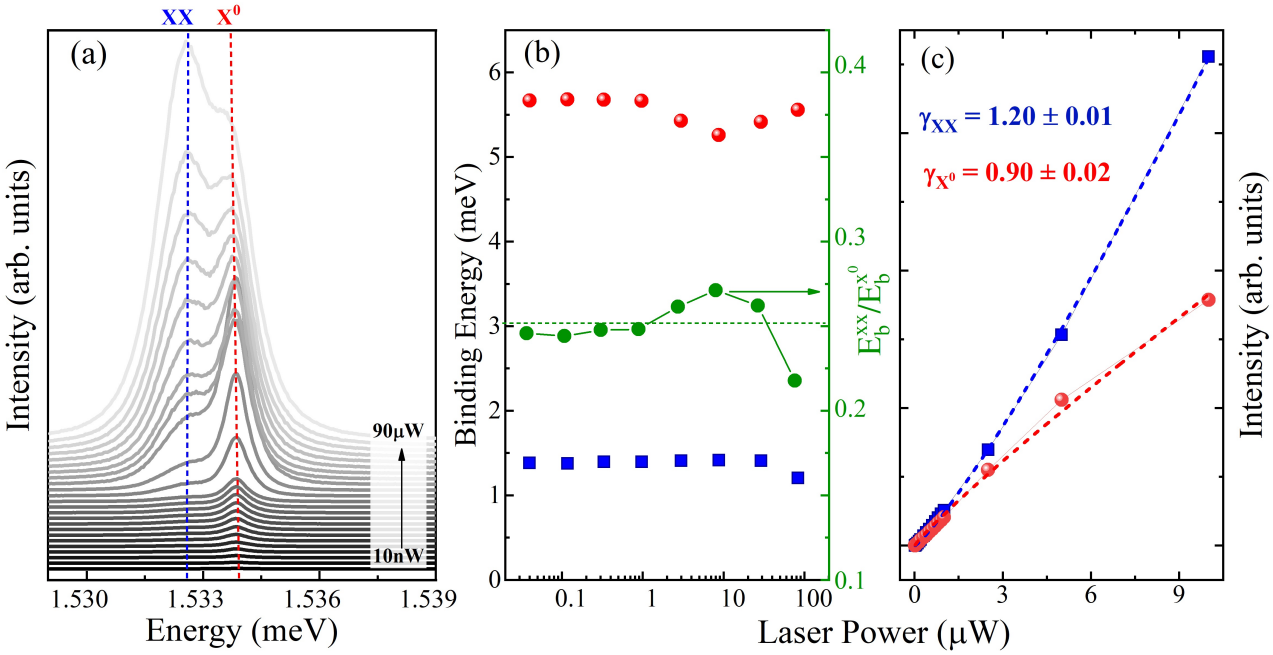

Figure 4.4: Photoluminescence spectra of the QW emissions at T= 10K as function of the laser power. Verticals blue and red dashed lines indicate biexciton (XX) and exciton (X^0) emissions, respectively. (b) Exciton and biexciton binding energies (right-green side: ratio of the biexciton to exciton binding energy) as a function of power. (c) Integrated intensity as a function of power.

In Figure 4.4(b) one can see that the exciton binding energy $E_b^{X^0}$ remain almost constant around 5.8 meV, as well as the biexciton binding energy E_b^{XX} around 1.4 meV, including the ratio of biexciton to exciton binding energy $E_b^{XX}/E_b^{X^0}$ stay nearly constant (~ 0.25), irrespective of the laser power. These values are in excellent quantitative agreement with previous reports about exciton and biexciton states in a 160 Å wide GaAs quantum well [84, 86, 87]. Note that the values of the binding energies presented here differ from the values afore presented with the temperature. This is probably because the emission behavior of these complexes is strongly dependent on the excitation wavelength and also on the power.

To quantitatively analyze the superlinear behavior of the biexciton and the linear one of the exciton, a deconvolution of the PL spectra for each excitation power to obtain the integrated PL intensity of each peak has been made, adjusting the shape of the spectra using Gaussian area functions. Finally, fitting the integrated PL intensity as a function of power using an expression of the type, $I \propto P^{\gamma}$ helps to interpret the nature of the transitions depending on the range of the γ values. According to the literature for $\gamma >$ 1, corresponds to biexciton, while $\gamma \approx 1$, correspond to exciton. Figure 4.4(c) is showing that the exciton peak has a linear behavior with power ($\gamma \sim 0.9$), while the biexciton peak

has a superlinear behavior ($\gamma \sim 1.2$), confirming that in fact those emissions belong to the exciton and biexciton complexes. Therefore, our experimental results associated with the theoretical framework developed here, clearly demonstrate that the low energy peak only can be ascribed as a biexciton transition rather than possible trion recombination as it was already present in the literature [16, 78–80, 82].

4.2.3 Magnetic-field dependence

Now the focus is on the magnetic-field dependence of the quantum well emissions. Magneto-photoluminescence spectroscopy and coherent optical experiments performed with polarized light, allows to study the spin-relaxation processes accompanying the energy momentum relaxation[20, 28]. Figure 4.5 shows the PL spectra at a fixed temperature of $T = 3.5$ K and four different laser powers, namely, 0.1, 0.8, 7.9 and 68 μW, without magnetic field (Figure 4.5 (a)), and in the presence of a magnetic field of 9 T for both circular σ^- (Figure 4.5 (b)) and σ^+ (Figure 4.5 (c)) polarization components. The polarization-dependent magneto-PL results reveal that the optical response of the

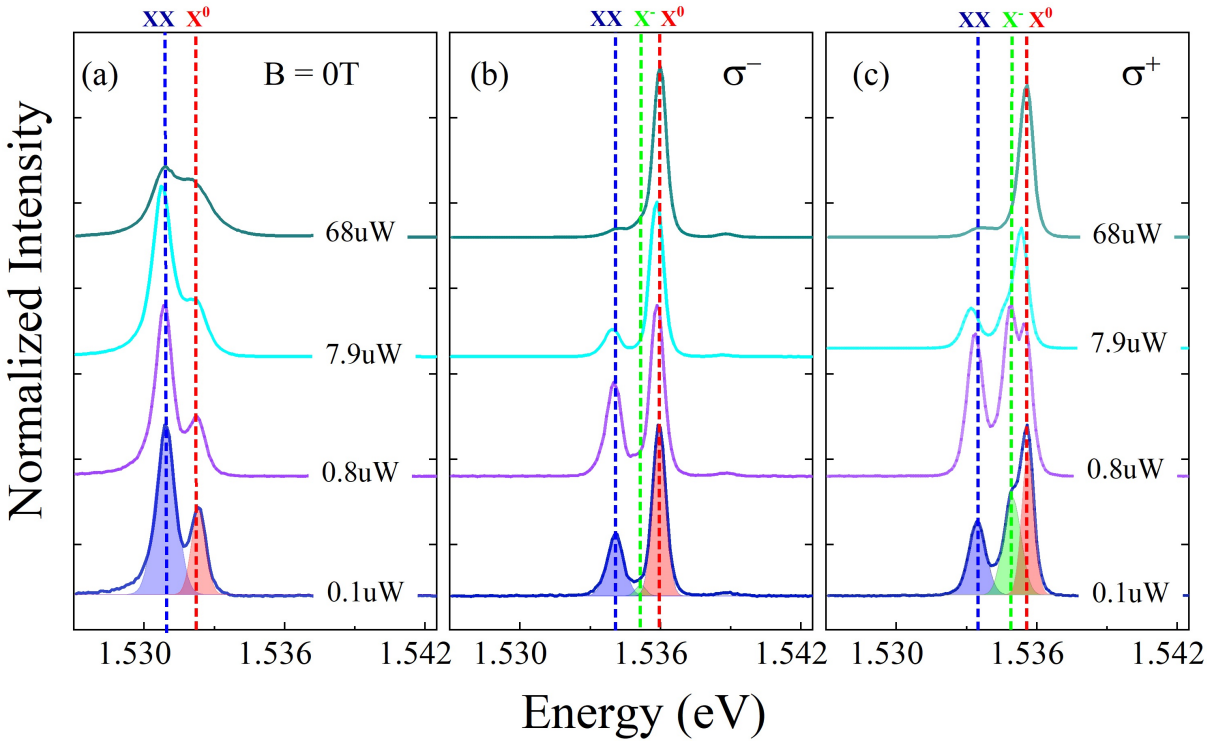

Figure 4.5: Photoluminescence spectra of the quantum-well emissions at $T = 3.5$ K as a function of laser power. (a) Without magnetic field. (b) and (c) $B = 9$ T with σ^- and σ^+ luminescence components, respectively. The vertical green dashed line indicates a new state (trion, X^-), which is clearly present for the (σ^+) luminescence component.

GaAs/AlGaAs quantum well strongly depends on the excitation power of the laser. For

zero magnetic field, we observe two low energy peaks ascribed to the single exciton and the biexciton emissions, separated by the biexciton binding energy of ≈ 1.5 meV as expected based on the results previously shown. The exciton to biexciton intensity ratio increases with the increasing laser power. Under an external magnetic field, the exciton intensity increases, while the biexciton intensity decreases. More interestingly, in Figure 4.5(c), an additional transition emerges at a finite magnetic field, ascribed to the trion X^-, which appears predominantly for σ^+ polarization at low laser power and disappears at the highest laser power. In the case of σ^-, the corresponding transition could only be identified at very low intensity. Yet, due to the lack of experimental resolution, it was not possible to perform a reliable deconvolution with the fitting procedure.

To explore the dependence of the exciton and biexciton states with the external magnetic field and, to investigate the new magnetically-induced peak, a detailed study of the evolution of the quantum well emissions for each laser power showed in Figure 4.5 was carry out. Figure 4.6 presents the results regarding the complexes' energy variations from the polarization-dependent magneto-PL spectra as a function of the magnetic field for all four laser powers.

The upper panels (Figure 4.6(a-d)) show the evolution of the emission peak positions as a function of the applied magnetic field and laser power. For low laser power, the new transition is emerging from $B > 3$ T and particularly for σ^+ polarization. Lower down in Figure 4.6(e-g) the binding energies (E_b) for excitons, biexcitons, and trions are presented. In the case of the excitation power of 68 μW, only the E_b for excitons and biexcitons (Figure 4.6(h)) is shown, since the emission identified as trion is absent at this power.

As was previously mentioned the exciton binding energy ($E_b^{X^0}$) was calculated as the difference between the bandgap ($e - hh_{\sigma^-}$) and the exciton energy ($X^0_{\sigma^-}$) states, and for the biexciton binding energy (E_b^{XX}) as the energy difference between the exciton ($X^0_{\sigma^+}$) and the biexciton energy (XX_{σ^+}) states. And the binding energy of the magnetically-induced state, which has been attributed to negative trions ($E_b^{X^-}$) was calculated as the energy difference between the $X^0_{\sigma^+}$ and the $X^-_{\sigma^+}$ states. All this data was obtained from the PL spectra and let a significant advancement in the understanding of the intricate and contrasting magneto-optical emission of these excitonic states. In Figure 4.6(e-g) is observed that its binding energy depends linearly on the magnetic field, as previously observed for negative trions [78].

Following the Figure 4.6(i-l) presents the corresponding Zeeman splitting ΔE, that is, the energy difference between σ^+ and σ^- emission for each state. It is observable a non-linear Zeeman splitting for the excitons, including an inversion of its sign. These features were reported before and produced by the spin-dependent field-induced combination between the light- and heavy-hole valence subbands [93–95]. While for the biexcitons state,

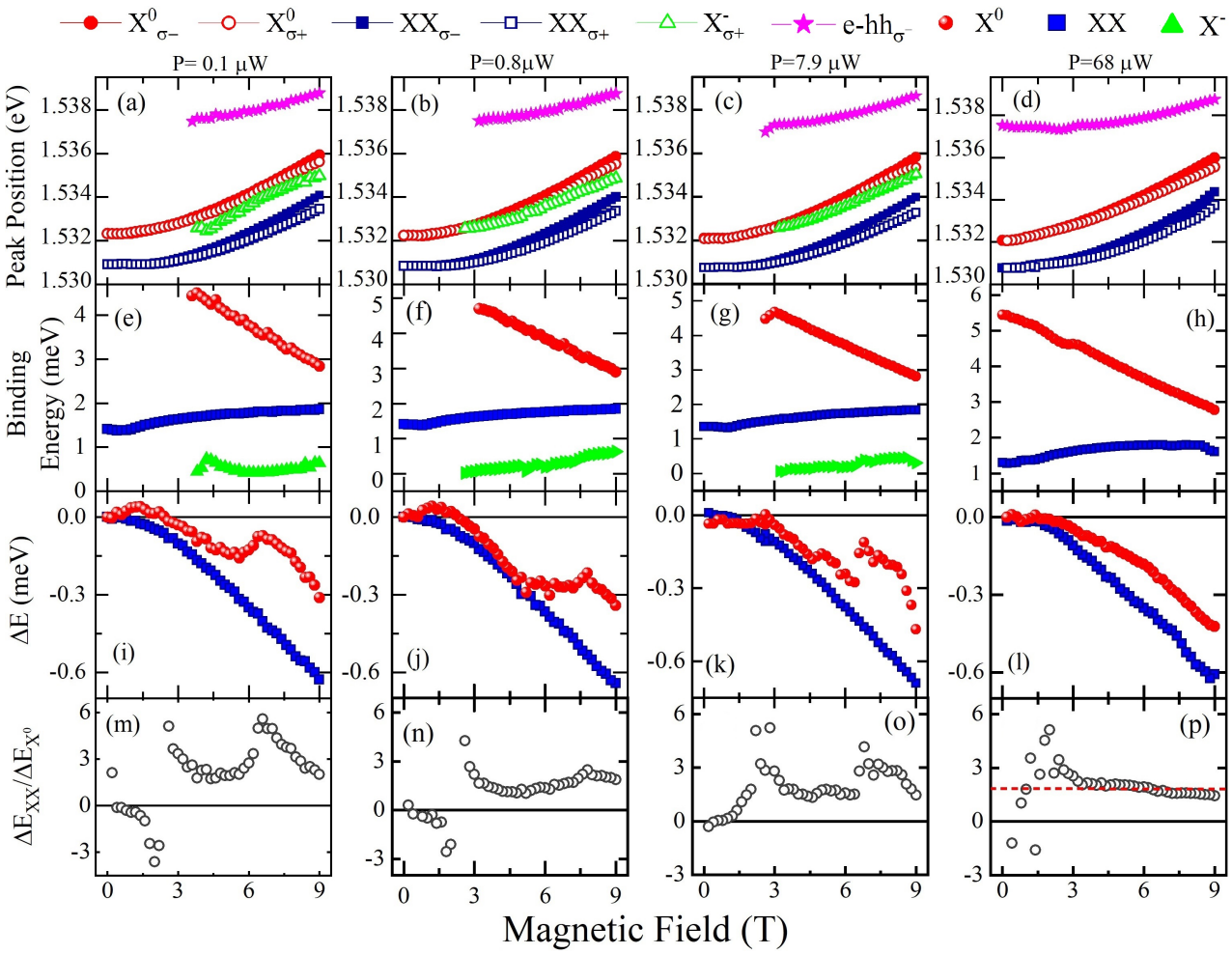

Figure 4.6: Results of PL measurements of the quantum-well emissions at $T = 3.5$ K and all laser power as a function of the magnetic field. (a-d) Peak positions. Filled and empty symbols represent σ^- and σ^+ circular polarization, respectively. (e-h) Binding energy for excitons, biexcitons, and trions. (i-l) Energy variation ΔE of circularly polarized emission of the exciton and biexciton for X^0 (red spheres) and XX (blue squares). (m-p) Biexciton to exciton Zeeman splitting ratio.

the Zeeman splitting ratio is essentially linear with the field, especially for $B > 3T$, which indicates a nearly constant g-factor. The analysis of the Zeeman splitting provides relevant information about the biexciton spin structure. A standard biexciton ground state in semiconductors consists of two electrons and two holes occupying the lowest electron and hole orbitals, each with paired spins. Such a quasi-particle decays emitting a σ^+ polarized light, leaving a σ^- exciton behind, or emitting a σ^- light, decaying into a σ^+ exciton state. Thus, a conventional biexciton state shows the same Zeeman splitting as the single exciton state [16, 78, 96–101]. This is not what is observed in the magneto-PL results.

Finally, at the bottom, the biexiton to exciton Zeeman splitting ratio is presented in Figure 4.6(m-p) which is ~ 2 for higher power lasers and $B > 4$ T. Such behavior suggests the presence of an unconventional biexciton state [102]. Biexcitons with different Zeeman splittings from exciton states were reported before in quantum dots [102] and interpreted as a consequence of non-trivial spin configuration.

Figure 4.7 illustrates the polarization-dependent magneto-PL integrated intensity results as a function of the magnetic field, for all four laser powers. Figure 4.7(a-d) shows the corresponding PL intensity, calculated as the integrated area of each peak. Note that, in the presence of an external magnetic field, the exciton intensity increases, while the biexciton intensity decreases. Figure. 4.7(e-h) is exhibiting the degree of circular polarization (DCP) of the PL emissions from the exciton and biexciton states, defined as the ratio of emission intensities (I_Y) as $DCP = (I_Y^+ - I_Y^-)/(I_Y^+ + I_Y^-)$ acquired in σ^+ polarization (I_Y^+) and σ^- polarization (I_Y^-).

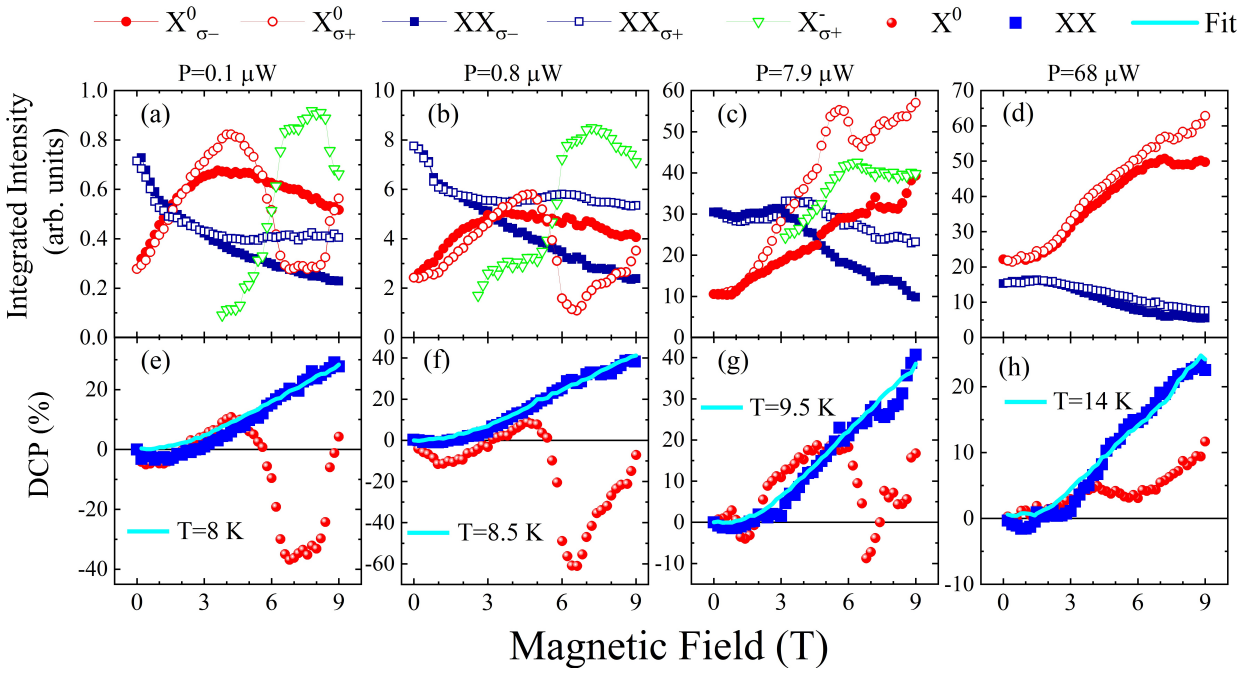

Figure 4.7: (a-d) Integrated PL intensities as a function of magnetic field for X^0 (red circles), XX (blue squares), and X^- (green triangles). (e-h) Degree of circular polarization of the exciton and biexciton. The black line indicates the polarization of the biexciton obtained according to the equation of the thermal equilibrium population of Zeeman sublevels.

The magnetically induced energy splitting leads to a population imbalance of the Zeeman sublevels, which manifests as a finite degree of circular polarization (DCP) of the photoluminescence, as shown in Figure 4.7. The magnetic-field evolution of the DCP

allows corroborating the apparent decoupling of the biexciton dynamics from the rest of the excitonic complexes. Indeed, the biexciton DCP follows the Zeeman Splitting behavior, ΔE_{XX}, of Figure 4.6(i-l) and can be fitted according to the equation describing the thermal equilibrium population of Zeeman sublevels [89], defined as

$$DCP_{XX} = -\tanh\left(\frac{\Delta E_{XX}}{2k_B T}\right). \tag{4.7}$$

The experimental data (square symbols) and the theoretical prediction (line) from equation 4.7 are shown in Figure 4.7(e-h). A good agreement between both can be achieved by using the nominal value of the temperature, which is shown in each case. Note that the experimental data fit with the temperature (solid line) is not of the bath temperature of the lattice T = 3.5 K, which indicates heating induced by photoexcitation. Nevertheless, is close enough to corroborate the biexciton decoupling that was already observed in the previous discussion on temperature dependence. The polarization of the exciton state (circular symbols), in contrast, does not seems to follow the Zeeman splitting; instead, its observed a negative polarization even for negative ΔE, which indicates a weaker emission from the lower energy spin component.

Furthermore, these results show that the emission intensity of the $X^0_{\sigma^+}$ state is strongly affected by the emergence of the $X^-_{\sigma^+}$ state (Figure 4.7(a-c)). Interestingly, it can be seen that the magnetic field at which the new peak appears coincides with the crossing between the two excitonic states with different polarization. That is, the X^- peak becomes visible when the energy of the σ^+ exciton state is lower than the energy of the σ^- state.

The spin asymmetry of the exciton and trion emissions can be further explored with the proposed theoretical framework. To proceed, has been solved the coupled Eqs. (4.1) and (4.4) by setting $F^{\pm}_{XX} = 0$ since the biexciton dynamics can be decoupled, as proven above (see Figure 4.2(b) and 4.7(e-h) and related discussions).

As presented along with the temperature-dependence analysis, a minimum number of free parameters to allow accurate reproduction of the experimental results has been kept. Namely, it is fixed $\tau_{r,X_0} = \tau_{r,X_-} = \tau_t = \tau^s_{X_0} = 1$ ps, and left only $\tau^s_{X_-}$ as a free parameter (see Eq. 4.5). Since the spin-down states (σ^-) have higher energy than the correspondent spin-up states (σ^+), a faster spin-flip process suppresses the $X^-_{\sigma^-}$ emission, in agreement with the experimental results displayed in Figure 4.7(e-h). Note that, while the $X^-_{\sigma^+}$ and $X^-_{\sigma^-}$ populations monotonically grow with increasing magnetic field, the $X^0_{\sigma^+}$ intensity decreases, while $X^0_{\sigma^-}$ remains almost constant. The physical reason for that is the thermally activated trion dissociation ($D(E_t)$) that decreases as the magnetic field increases, following the enhancement of the trion binding energy. This mechanism leads to the decrease of the $X^0_{\sigma^+}$ emission and the simultaneous increase of $X^-_{\sigma^+}$ emission, which is corroborated by experimental results.

4.2.4 Conclusions

Through the combination of the theoretical framework and experimental results, it has been proved the nature of a GaAs quantum well excitonic peaks. First, the Zeeman splitting and binding energies have been determined by polarization-resolved photoluminescence measurements, which spectra showed an increasing splitting of the high energy peak, attributed to the exciton and trion states; this last one is a magnetically induced state, appearing predominantly for polarization σ^+ under a finite magnetic field and strongly influencing the exciton emission. Besides, the dependence of the exciton spin splitting and polarization on both the laser power and external magnetic fields is shown. With a non-resonant excitation, biexcitons are also observed and established as mainly photocreated with dynamics almost independent of excitons and trions. The theoretical analysis explained the decoupled biexciton dynamics from the other quasi-particle complexes. On the other hand, biexciton's PL emission showed a supralinear dependence on the laser power, decreasing dramatically with increasing temperature exhibiting a monotonic Zeeman splitting, a constant g-factor, and a polarization defined by the thermal population of the Zeeman sublevels. The theoretical framework can satisfactorily explain the intricate dynamics of excitons and trions, including their spin asymmetry. Furthermore, a controversy about the nature of a low-energy excitonic peak through the combination of experimental results and theoretical framework has been clarified, proving that it can be attributed to a biexciton emission.

Chapter 5

Resonant Tunneling Diodes

This chapter will present the main results obtained from the electronic transport and optical measurements of n-type GaAs/AlGaAS double barrier quantum well (DBQW) resonant tunneling diodes (RTDs). Comprising both the reference (GaAs) and the prewell (i-$In_{0.15}Ga_{0.85}As$) RTD's samples. First it is shown the analysis of the transport results and a comparison pointing out the main differences in electronic transport and electroluminescence emission under external parameters as magnetic fields and temperature. Results are compared between the RTD-Ref and RTD-Prewell samples, where the advantages of introducing a prewell layer adjacent to the emission barrier are highlighted. Photoluminescence data is presented to complement the scenario of the dynamics and charge accumulation of the carriers.

5.1 Basic transport properties of AlGaAs-based RTDs

Electrical characterizations were performed on both RTD-Ref and RTD-Prewell samples to study and compare the electronic transport properties. The RTDs were operated in a two-terminal setup with a single bottom contact, and just for DC positive bias voltages, (the diodes were designed to operate in positive or forward bias because the resonance peak of the electric current occurs at lower voltages and with more stability) that is, the carrier injection comes from the substrate side to the top contact with a high precision voltage source, and the current was measured as voltage drop V_{out} across a series resistor with a digital multimeter.

Figure 5.1 shows the Simulated band structure with the conduction and valence energy band diagram of both RTDs: RTD-Ref and RTD-Prewell Figures 5.1(a) and (b), respectively. To investigate the RTDs in detail the electroluminescence induced while the I(V)-characteristics is been obtained must be considered. Current-voltage characteristics

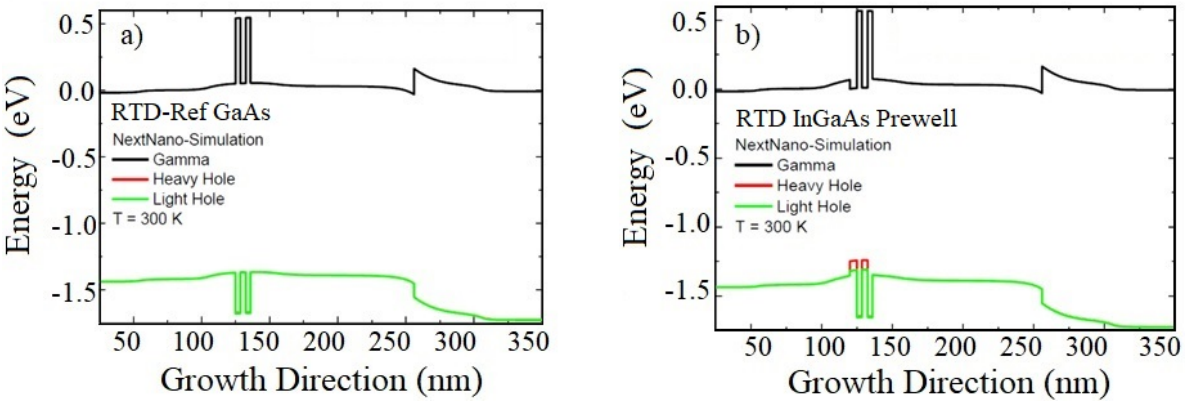

Figure 5.1: (Simulated conduction band (CB) minimum and valence band (VB) maximum for the (a) RTD-Ref and (b) RTD-Prewell.

were carried for RTD-Ref and RTD-Prewell at 4K in forward bias. The corresponding current density-voltage (j(V)) is obtained from the I(V) and the diode area and are displayed in Figure 5.2(a). After surpassing a critical voltage of V ≈ 2V, the EL emission is

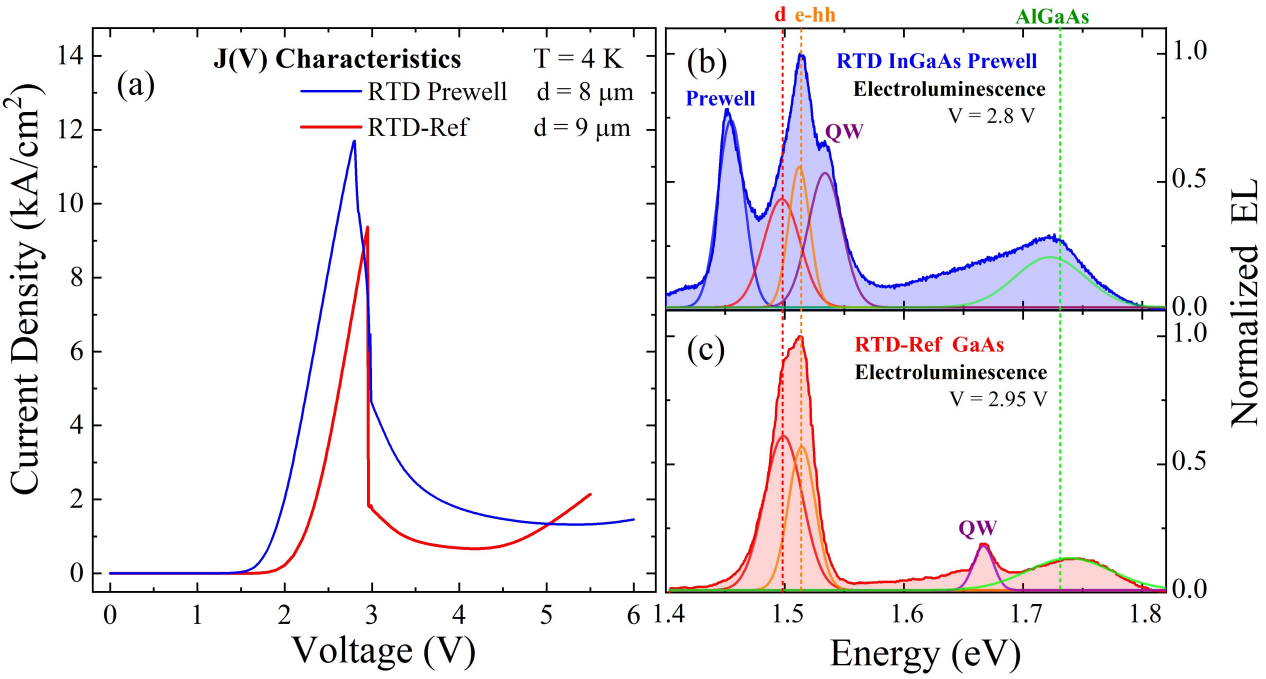

Figure 5.2: (a) Current-voltage characteristics for both samples. (b) and (c) EL normalized signal obtained at resonances for RTD-Prewell (blue) and RTD-Ref (red) spectra, respectively. Main emission lines are present, identified through colorful Gaussian adjustments to represent regions where recombination takes place.

observed. EL spectra for both RTD-Ref and RTD-Prewell samples were collected at reso-

nant current conditions $V_{res} = 2.95$ V and $V_{res} = 2.47$ V, and are shown in Figures 5.2(b) and (c), respectively.

These j(V) characteristics with noticeable resonances are the main evidence of resonant tunneling of electrons traveling directly from the highly doped region through the double barrier structure of the devices. For RTD-Ref the peak current density is j_{peak} = 9.4 kA/cm^2 at V_{res} = 2.95 V and after resonance voltage, the valley current density is j_{val} = 0.7 kA/cm^2 with a minimum at V_{val} = 4.17 V producing, as a result, a Peak to valley current ratio (PVCR) of $\approx$ 14. While for the the RTD-Prewell the peak current density is j_{peak} = 11.7 kA/cm^2 at V_{res} = 2.8 V, and after resonance voltage, the valley current density comprises a longer voltage range with a minimum around j_{val} = 1.3 kA/cm^2 at V_{val} = 5.3 V producing a PVCR of $\approx$ 8.8. Since the heterostructure designs are almost equal (aside from the pre and quantum-well composition), the resonant currents and voltages are comparable. Furthermore, the valley current density is higher for the RTD-Prewell leading to a lower PVCR at 4 K.

The RTD-Prewell EL normalized spectrum exhibits five distinct emission lines according to the fittings shown: the lower energy peak ascribed to the prewell at 1.453 eV, d = 1.497 eV associated with the donor-band level recombination [103, 104], e-hh = 1.512 eV is the band-to-band (e-hh) emission in the bulk of GaAs, QW = 1.533 eV, originated from the quantum well, and AlGaAs = 1.724 eV, which arises from the AlGaAs optical window region. In turn, the Ref-GaAs spectrum consists of four emission lines, (without the lower energy peak of the prewell), d = 1.498 eV, e-hh = 1.514 eV, QW = 1.666 eV originated from the quantum well, and AlGaAs = 1.735 eV. In both cases, it wasn't possible to exactly identify the origin of the broadband superimposed on the AlGaAs emission line, it is associated with the level of donors in the AlGaAs optical window, since in the $Al_XGa_(1-x)As$ alloys is very unstable, ranging from 6 meV for $x < 1$ to 160 meV for indirect bandgap.

Figure 5.3 provides the intercorrelations among the measures of I(V) with the EL emissions for both samples, across the entire RTDs operating active voltage range, and focusing on the emissions coming from the DBQW region. After exceeding the critical voltage value of V $\approx$ 2V EL emissions are observed and shown in Figure 5.3(a) and (b) RTD-Ref and RTD-Prewell, respectively. From this value a low density of holes are created via impact ionization on the collector side, due to the electric field this holes can go through the entire structure tunneling the resonant states towards the prewell. As the prewell is energetically most favorable the holes will relax to the lowest accessible state and finally recombine with electrons there. Thus, appearing the strongest emission line at the lowest energy side is attributed to the prewell ground state at $\approx$ 1.453 eV. In contrast, as the RTD-Ref has not a prewell, the holes recombine mostly with electrons from the donor level, probably from the highly doped region of the emitter side, as a result, the

donor level emission is observed at ≈ 1.49 eV from voltages values of 2.2 V.

By increasing the voltage, the other EL emission lines increases compared to prewell emission, because electrons tunnel through the DBQW, increasing the charge density in other regions rather than accumulating in the prewell, and for example, a fraction of holes can now reach the highly doped region, emerging donor emission as well. This voltage affect the prewell energy because of the electrons that tunnel resonantly through the DBQW undergo an electrostatic feedback screening the prewell [75] therefore its energy has a rapid increase initially and then becomes nearly constant until the resonant condition. While the voltage is increasing up to the resonance, the emission associated with the band-to-band (e-hh) intrinsic GaAs bulk are observed at ≈ 1.51 eV (for both samples) and competing with the donor level, where they get populated up to the maximum leading to a better-resolved emission peak. Finally, the emissions associated with the quantum-well (QW) and the AlGaAs optical window (OW) are also emerging around 1.533 eV and 1.724 eV, respectively, and particularly in this range of voltage where a portion of the holes created via impact ionization on the collector side recombines with electrons accumulated in the AlGaAs and in the QW resonant states. Surpassing the resonance, the signal/noise

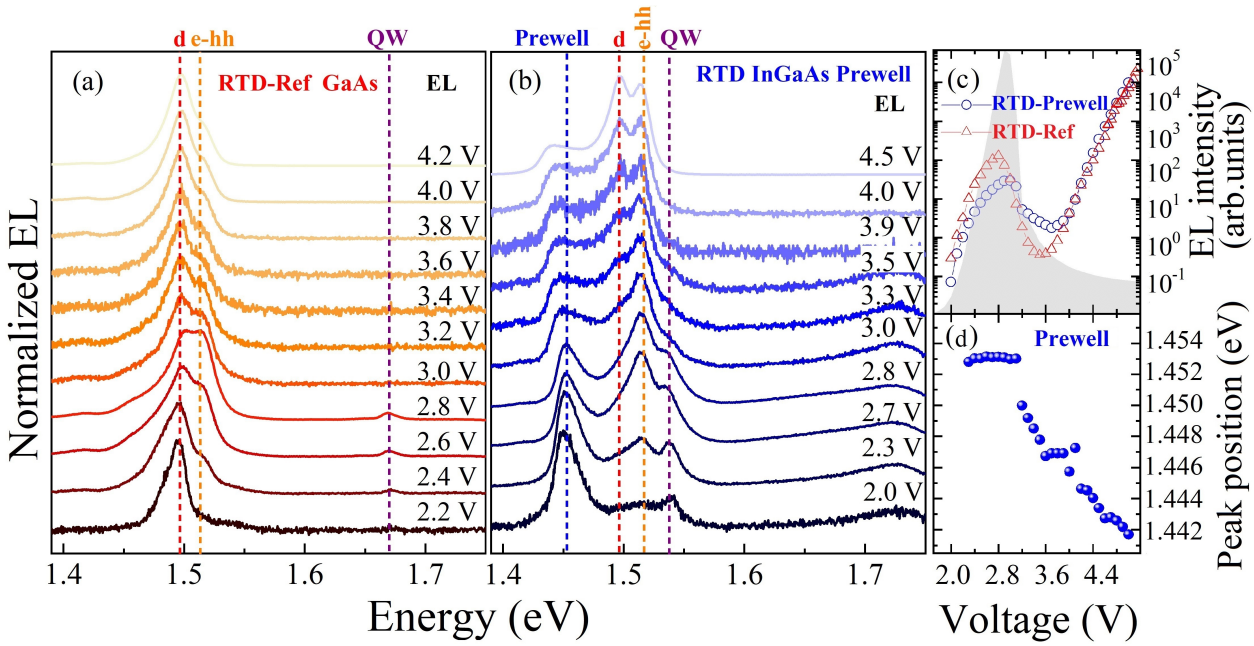

Figure 5.3: Voltage dependence of: (a) and (b) Normalized Electroluminescence spectra variation for RTD-Ref and RTD-Prewell, respectively. (c) Integrated EL intensity for RTD-Prewell (blue opened circles) and RTD-Ref (red opened triangles), the gray shadow correspond to the RTD-Prewell I(V) curve. (d) Prewell peak position.

ratio is lessened, leading to a general reduction in the electroluminescent spectrum. The donor level is most likely to come from the emitter contact side, therefore, until the res-

onance condition the generated holes thermalize to the prewell lowest state and cannot go further into the emitter region, whereas the charge carrier density inside the QW is mainly induced by the resonant tunneling, as well as the recombination rate. Differently, after the resonance, the generated holes have now enough energy to surpass the prewell and reach the region to recombine with electrons bound with donor impurities making the less energetic level (d) again more intense than the GaAs bulk emissions. After that, as no charge is located inside the QW, the QW emissions are no longer visible. The electrons are forced to accumulate in the prewell, whose emission gets more asymmetric in the high energy side and its relative intensity increases until reaching a maximum point at around 3.8 V. Finally, as holes accumulate more and more in the intrinsic region and the prewell escape rate gets higher, a decrease in the prewell emission is clearly noted.

These EL emissions across the RTD active voltage range provides insight into the evolution of the band profiles, the internal charge carrier transport processes, and the quantum well states during the resonant tunneling. For example, for the RTD-Ref it is the sum of electron and hole quantization energies by subtracting E_{QW} from E_{e-hh} ($E_e + E_h = 146$ meV), the same is not possible for RTD-Prewell due to a lack of optical information from the bottom of InGaAs-QW. Apart from that, these findings are not possible to obtain through pure photoluminescence (PL) measurements, because, under an electric field, the incident light can disturb the system and change the intrinsic charge carrier dynamics and DBQW quantization due to the large photogeneration of electron-hole pairs, and at V = 0 V is not possible to observe any QW emission line, making EL better suitable for this analysis [105–107].

To analyze the EL spectra shown in Figure 5.3(a) and (b) gaussian fittings were performed. The results of the RTD-Ref and RTD-Prewell considering all integrated emissions are presented in Figure 5.3(c) as a function of voltage. A gray shadow of the RTD-Prewell I(V) curve is additionally plotted, only for illustration purposes. Both intensity curves have a similar response with a peak at resonance, followed by an intensity drop in the valley region and increasing again at high voltages. In the negative differential conductance (NDC) region, the RTD-Ref exhibits a decrease of about three orders of magnitude, besides the fact that the RTD-Prewell decreases only in one order of magnitude. It has been demonstrated that such a higher EL peak to valley ratio (PVR) for structures like RDT-Ref is due to a competition between the coherent and sequential tunneling channels [108], in contrast, the smaller optical PVR of RTD-Prewell is probably caused by the charge build-up in the prewell. As the prewell layer is the active element and the one which rules a great part of the quantum transport, its emission is analyzed individually, Figure 5.3(d) shows the evolution of its peak position under the applied voltage. The prewell peak position obtained at the peak maximum intensity ≈1.453 eV at 2.0 V, remains nearly constant up to the resonant voltage. After the resonance, a constant redshift

is observed of about 4.40 ± 0.24 meV/V.

Until now, it has been studied the charge carrier dynamics as a function of the applied voltage, without a magnetic field, by analyzing the electroluminescence variations along with the voltage RTD operation range and discussing the differences between the structures with and without the emitter prewell. The next section will be focused on the electrical and optical properties depending on the magnetic field.

5.1.1 Magnetic field dependence

Current-voltage characteristics and Electroluminescence emissions of the RTDs were measured under different magnetic fields (Magneto-electroluminescence) in the range from 0 to 9 T applied perpendicularly to the plane of the double barrier structure (the so-called Faraday configuration). The results obtained for the RTD-Ref are presented in Figure 5.4. To make the evolution of the current density and EL emission clear when applying the magnetic field, the results are presented according to a sequence of colors.

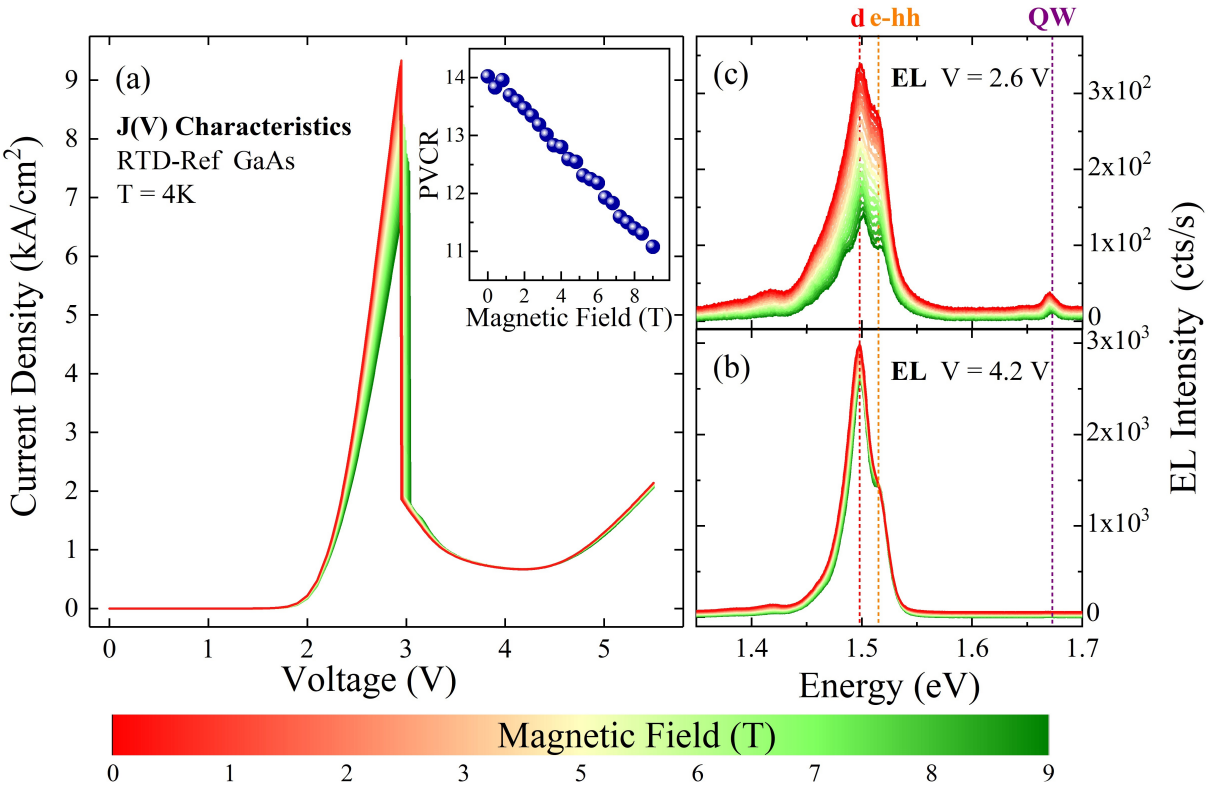

Figure 5.4: Magnetic field dependence of RTD-Ref. Fields between 0 and 9 T. (a) Current density-voltage characteristic curves, (inset: PVCR). (b) and (c) EL spectra of the RTD-Ref at 2.6 V and 4.2 V, respectively.

From Figure 5.4 (a) it is clear that the resonance peak is shifted to lower values of

current (due to the magneto-resistance effect) even though to higher voltages with the increasing of the applied magnetic field, while the valley current and voltages values remain basically constant, this behavior leads to a decrease in the PVCR of ≈ 20% as can be seen in the inset. Figures 5.4 (b) and (c) shows the spectra collected on-resonance (V=2.6V) and after (V=4.2V) resonance, respectively, for magnetic fields from 0 to and 9 T. The EL spectra consist mainly of three emission lines: the donor level (d) at ≈ 1.49 eV, the band-to-band (e-hh) at ≈ 1.51 eV, and the quantum-well (QW) at ≈ 1.66 eV. In this figure and for both cases (on and after resonance) it is evident an overall reduction of the intensity of the emitted light as the magnetic field increases probably due to the increased magnetoresistance.

Figure 5.5(a) illustrates the density current-voltage results of the RTD-Prewell under different magnetic fields from 0 to 9 T. In the same way, as for the RTD-Ref, the resonance peak is shifted to lower values of current and higher voltages with the increasing of the applied magnetic field. The values for valley currents and voltages continue almost constant, leading to a decrease in the PVCR of only 5% (when compared to the RTD-Ref) as shown in the inset.

Figures 5.5(b) and (c) present the EL spectra of the RTD-Prewell obtained after surpassing the critical voltage of V ≈ 2V and for magnetic fields from 0 to and 9 T, on-resonance (2.7 V) and after resonance (4.6 V), respectively. On-resonance, the first noticeable one is the prewell with at ≈1.453 eV, its intensity remains the same, in contrast, all other peaks weaken due to the increased magnetoresistance. After resonance, the prewell emissions lines become stronger at 9 T, whereas the emissions related to the QW and the AlGaAs optical window are no longer visible. The general EL suppression after resonance is stronger in this RTD when compared with that obtained for RTD-Ref. This may be because electrons confined in the prewell with defined energies are screened by strong magnetic fields due to the in-plane confinement enhancement [109], reducing the tunneling probability, and therefore, the overall emission. This is not the case for the RTD-Ref because a broader distribution of the 3D states does not undergo any magnetic field screening, keeping the transport constant. Furthermore, besides the EL intensity reduction, there are splittings in the prewell emission.

Given that the magnetic field influence on the optical properties of the structures is more pronounced in the RTD-Prewell showing splitting subbands into degenerated electron and hole Landau Levels (LL) (with the same degeneracy ($2eB/h$) separated by the cyclotron energy gaps [110]), appearing in the EL coming from the prewell quasi-bound state, a more detailed analysis of the spectra of El from the RTD was performed. Figure 5.6 presents two-dimensional intensity color-maps EL of all the RTD-Prewell EL spectra as a function of the magnetic field for different voltage values. Top (Figures 5.6(a), (b) and (c)) and bottom (Figures 5.6(d), (e) and (f)) panels correspond to the measurements

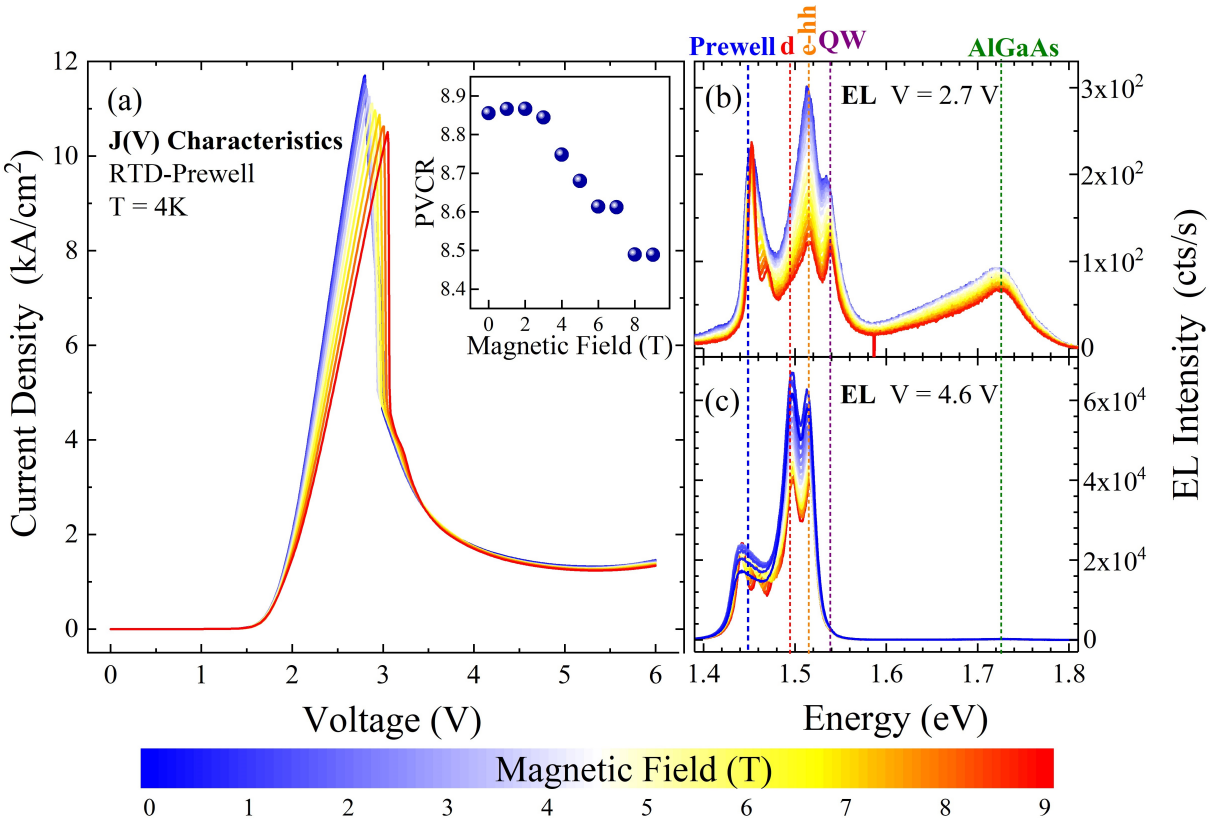

Figure 5.5: Magnetic field dependence of RTD-Prewell. Fields between 0 and 9 T. (a) Current density-voltage characteristic curves, (inset: PVCR). (b) and (c) EL spectra of the RTD-Prewell at 2.7 V and 4.6 V, respectively.

performed before and after resonance, respectively. All the peaks mentioned in the above section are identified.

An almost linearly field-dependent and equidistant Landau Levels fan-shaped pattern can be identified from the data in a magnetic field of the emitter prewell emission line over a wide voltage range. Despite of that, there are differences between the LL splitting before and after the resonance condition. Another remarkable feature is the lack of LL splitting in the QW state, which is an indicator that resonant transport occurs through its ground state. Upper panels ((a), (b) and (c)) from Figure 5.6 evidences a state in which the LL are not well resolved yet. This is because the escape rate through the resonant states in the QW is more favorable since the QW is supporting strong charge build-up due to resonant conditions, consequently, a greater fraction of electrons tunnel through the double barrier rather than thermalize, accumulate and recombine in the prewell. The lower panels ((d), (e) and (f)) of Figure 5.6 show the events after resonance, where the LL are well resolved (indicated with black lines). In this case, the energy level misalignment quenches significantly the resonant tunneling condition, promoting a

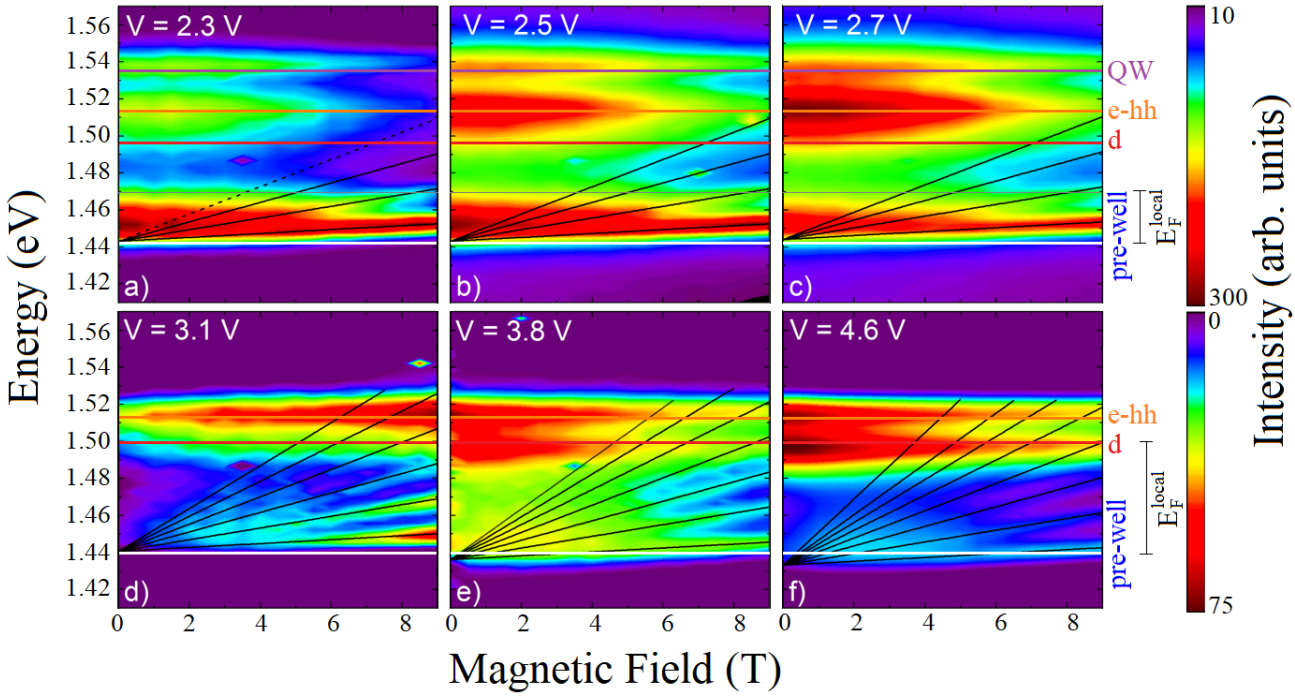

Figure 5.6: Two-dimensional intensity color-map of RTD-Prewell EL emissions vs. magnetic field obtained at (a) 2.3 V, (b) 2.5 V, (c) 2.7 V, (d) 3.1 V, (e) 3.8 V and (f) 4.6 V. Black lines indicate the Landau levels splitting calculated with Eq.5.1

thermalization process, allowing electrons to accumulate in the prewell, raising $E_F^{prewell}$ to higher energies and thereby increasing the number of LL splittings [111]. Quantification of the LL allows a direct determination of changes in relevant parameters, such as mass, carrier density, band edge, etc. From the experimental dependences of the transition energies with the applied magnetic field, the energy separation of the LL can be estimated directly from the EL intensity since the magnitude of an electron-hole LL transition is proportional to the occupation and saturates when electrons and holes levels are full. The transitions between the LL of a parabolic band for the holes and the non-parabolic band for electrons have been calculated using a two-band model [110, 112]

$$E_N = \frac{E_g}{2} + \sqrt{\left(\frac{E_g}{2} + E_0\right)^2 + E_g\left(N + \frac{1}{2}\right)\frac{\hbar e B}{m_{0,e}} + \left(N + \frac{1}{2}\right)\frac{\hbar e B}{m_{0,h}} + H_0}, \tag{5.1}$$

where $m_{0,e} = 0.071 m_0$ [113] and $m_{0,h} = 0.15 m_0$ [114] are the band edge masses of the $In_{0.15}Ga_{0.85}As$ conduction and valence bands, respectively, E_g is the $In_{0.15}Ga_{0.85}As$ band gap energy, N is the Landau level quantum number, E_0 and H_0 are the electron and hole subband energies, obtained by subtracting E_g from the experimental prewell emission at B = 0 T accordingly to get the best fit for the LL. The calculation results are shown as

solid lines in the colorplots of Figure 5.6 where it can be seen that all Landau energies for N $\neq$ 0 converge in one point at B = 0 T, and fit well with the experiment. Experimental and theoretical ground state differ at low magnetic fields. This simple theory diverges from the experiment for low fields which indicates a small renormalization of the band gap due to the applied electric field.

Resolving the current evolution when applied a magnetic field, the charge carrier density at the emitter prewell can be calculated [37, 111]. The difference between Landau levels represents the change during the tunneling. The Nth Landau level aligns to the local Fermi energy, exhibiting peaks in the tunnel current versus magnetic field curves when the Landau levels pass through the local Fermi level, leading to oscillations with a definite period $\Delta(1/B)$ and related to the local Fermi energy E_F^{local} by the equation [37]:

$$(\Delta(1/B))^{-1} = \frac{m^* E_F^{local}}{e\hbar}, \tag{5.2}$$

where m^* is the effective mass.

From the I(V) characteristics curves at several magnetic fields obtained for RTD-Ref and RTD-Prewell, is possible to extract the current as a function of the magnetic field by transposing the data and fixing the voltage. Figure 5.7(a) exhibits normalized current oscillations as a function of the inverse field (1/B), red and blue lines draw the result for each sample respectively, at different voltages. Oscillations are evident for both samples, which are the signature of two-dimensional electron gas (2DEG) quantization due to the crossing of the Landau levels and the Fermi energy [39]. For the RTD-Ref these oscillations are present from 1 V to 2.2 V and can be further seen after the resonance, presenting a higher frequency, from 4 V and forward. Despite this RTD has not a prewell on its structure, an emitter triangular prewell is created due to the band structure bending under an electric field [47]. For the RDT-Prewell the oscillations are produced by the InGaAs emitter prewell quantization of the Landau Levels and they can only be resolved in a small range of voltage from 0.75 V to 1.95 V. The oscillations seems suppressed possibly by the magnetoresistance for higher voltages as the electron density increases. After the resonance (horizontal dashed line) the oscillations get an inverted concavity and without a complete a period. Figure 5.7(b) displays the charge carrier density inside the (triangular) emitter prewell ($\eta_{prewell}$) as function of the voltage for the RTD-Ref and RTD-Prewell calculated using Eq. 5.2 for fully occupied states $E_F = \hbar^2\pi\eta/m^*$, [115–117] and current oscillations with period $\Delta(1/B)$. This gives,

$$\eta_{prewell} = \frac{e}{\hbar\pi\Delta(1/B)} \tag{5.3}$$

Before the resonance, the densities of charge carriers calculated for both samples are close, certainly, because they were grown with the same donor profile. For the RTD-Ref, the charge carrier density can be calculated even after the resonance ($<$ 4 V), obtaining

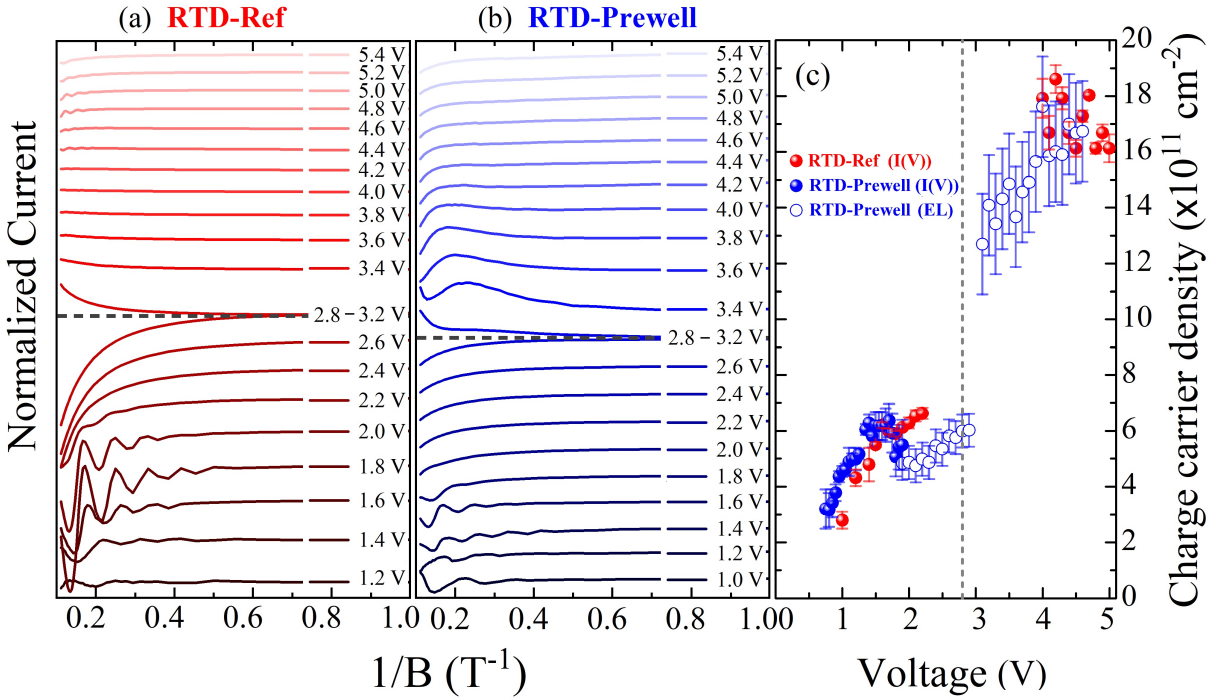

Figure 5.7: (a) and (b) Normalized current oscillations as function of the inverse of magnetic field, for voltage values from 1.0 to 5.5 V for RTD-Ref and RTD-Prewell, respectively. Offseted for clarity. (c) Charge carrier density as function of voltage extracted from the current oscillations of RTD-Ref and RTD-Prewell, red and blue spheres, respectively, and from the RTD-Prewell EL emission, opened blue circles. Vertical dashed-line indicates the resonance voltage.

more elevated carrier densities than the before resonance. This is a result of the charge carrier accumulation on the emitter side [111] indicating a coherent transport related to the tunneling through excited levels in the QW.

For the RDT-Prewell is not possible to calculate the charge carrier density for voltages above resonance using this method since the oscillations cannot be resolved. This lack of oscillations are probably due to strain-induced defects caused by the Indium incorporation on the prewell, which could destroy the phase coherence when the system is off-resonance. Alternatively, also probably due to incoherent transport, such as thermionic emission, incoherent tunneling, leakage toward the sidewall, and others not influenced by the magnetic field. Nevertheless, even though it is not possible to calculate the charge carrier density when the current oscillations are missing, EL measurements are useful to investigate the charge accumulation and complete the map of carrier density changes across the RTDs' operating voltage range. Hence, the prewell emission before resonance (Figure 5.6), provides the prewell quasi-Fermi energy, $E_F^{prewell}$. Derived from the difference between the peak position and the energy at half-width at $B = 0T$ (half-width is

$\approx 2/3$ of the $E_{Fermi} - E_{Val}$ since EL peak is determined by both, E_{Fermi} which affects the high-energy side while E_{Val} the low-energy side) [118, 119].

After resonance, the prewell emission asymmetry interferes with the donor emission line (d), which difficult the identification of the quasi-Fermi energy with the prior procedure. In this case, the EL intensity as a function of the magnetic field can be fixed energy values since the splitting LL are well resolved. Thus, the $E_F^{prewell}$ can be determined as the difference between prewell emission energy and the energy position at which LL are no longer detected but extrapolated down to 0 T. Therefore considering that the charge carriers are thermalized, the density of the 2D states at the prewell were calculated the same as Eq. 5.3 for fully occupied states as:

$$\eta_{prewell} = \frac{E_F^{prewell} m^*}{\hbar^2 \pi}. \tag{5.4}$$

The charge carrier density extracted from the EL measurements using this calculation is depicted in Figure 5.7 (b) as open blue circles. The error bars before and after resonance are estimated considering the spectral noise and the donor emission linewidth due to the interference between the LLs, respectively. (d) As can be seen, before resonance, these results coincide within the same range of the blue dots, and after resonance, the obtained charge carrier density is similar to the RTD-Ref. These agreements are indications that the optical emission can also be used to estimate these quantitative features.

5.1.2 Conclusions

Via magneto-transport results, the charge carrier density for both samples was resolved. Magnetic current oscillations were found before resonance and comparable. However, the loss of the oscillations after resonance for the Prewell RTD unable to estimate the charge carrier density through this method. Hence, an approach to evaluate charge accumulation utilizing magneto-electroluminescence was proposed, finding that the internal charge carrier transport processes are observed without the need for photoluminescence. Since RTDs have shown extreme sensitivity to variations in the local electrostatic potential, directly affecting the transport characteristics, i.e., variations induced by illumination and the Landau levels splitting in the emitter prewell through EL was observed, the prewell quasi-Fermi energy level was estimated; thus, enabling the determination of the charge carrier density after resonance. Despite the differences between both samples on their optical and transport properties, mainly attributed to the prewell presence, the results showed good agreement regarding transport effects. Furthermore, combining transport and optical outcomes gives valuable information on the charge carrier dynamics, for example, allowing the determination of the charge carriers accumulation throughout the RTDs operating voltage range.

Chapter 6

Quantum Dots Resonant Tunneling Diode for Single-Photon Detection

This chapter presents the main results obtained from transport and optical spectroscopy of AlAs/GaAs RTD double-barrier structures with embedded InGaAs quantum dots and different AlAs barrier thicknesses. Firstly, from the analysis of transport results, the tunability of the resonant current density by adjusting the AlAs barrier thickness. Secondly, it is presented active quantum dots and their outcomes on the electro-optical properties. Finally, it is demonstrated that the resonant tunnel current is highly sensitive to the accumulation of single photoexcited holes by the quantum dots.

6.1 Electric transport characterization

RTDs have an electrically active region of only a few nanometers thick, including the double barrier quantum well (DBQW) structure. Initial electrical characterizations were performed in a set of three samples, consisting of AlAs/GaAs RTD double-barrier structure (DBS) with embedded InGaAs quantum dots, with different AlAs barrier thicknesses, and for increasing diameter sizes ranging from 3 to 13 μm; in order to elucidate the electric transport properties depending on the structure parameters, such as barrier thicknesses and diode diameter contrasting the main differences due to the insertion of a QDs layer to DBS.

The RTDs were operated in a two-terminal setup with a single bottom contact and for both forward and reverse bias voltages at cryogenic temperatures T = 4 K. The current was measured as voltage drop V_{out} across a series resistor with a digital multimeter. At low temperatures, coherent transport is enhanced compared with incoherent transport; this makes possible to study the purely quantum phenomena involved in the structure without undesirable external disturbances.

Figure 6.1 shows the RTD current density-voltage (J (V)) characteristics obtained from dividing the current into the diode's cross-sectional area (all diodes that showed an electric response) for the sample with the thinner barrier thickness of $t_b \approx 1.5$ nm.

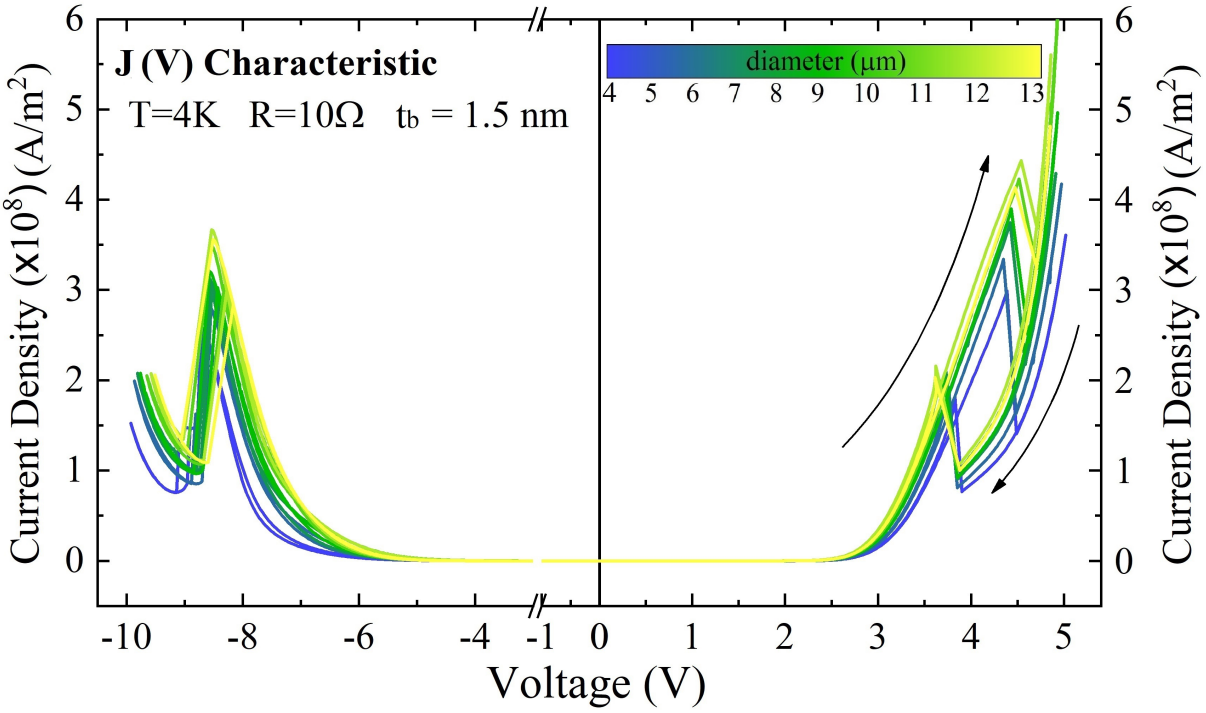

Figure 6.1: Density current-voltage (J(V)) characteristics at forward and reverse bias of the $t_b = 1.5$ nm sample for different diameters between 4 and 13 μm, obtained at 4 K. The arrows indicate the current flow direction.

Resonant tunneling is observed for almost all diameters, with well-defined resonance peaks appearing at high voltages close to 4.5 V and -8 V, followed by the region of negative differential conductance (NDC), with peak to valley current ratios of up to $PVCR \approx 4$ in forward bias and $PVCR \approx 3$ in reverse bias. It is observed that the current density is highest for the largest diameters. The asymmetry of the J(V)-characteristics, i.e., the difference in voltage required to achieve the resonance condition depending on the bias direction, is due to the asymmetric heterostructure layout in which the diodes were designed: in the case of forward bias, the electrons move directly from the highly doped region to the double barrier structure, while for the reverse bias, electrons are required first to overcome a potential barrier formed after the optical window (OW) of AlGaAs, which also drives them through a long path before reaching the DBS.

Figures 6.2 (a) and (b) are showing the linear behavior of the peak and valley current as a function of the diodes' area, at the reverse and forward bias, respectively. It is evident that the current peak density scales almost linearly with the diameter since the electrical

transport is directly proportional to the area that the electrons pass through. The PVCR reaches values up to 4.18 as shown in Figure 6.2(c), at forward bias. From this figure, it can be noticed that for areas smaller than 30 μm^2, the PVCR is lower and increases until it approaches at around 4 for diodes starting from 40 μm^2. High PVCR values indicate a high-quality device since the valley includes currents unrelated to quantum tunneling, such as leakage current. The electrical power is also directly proportional to the area (nearly linear) as shown in Figure 6.2 (d). The values of peak-current power at forward bias are lower when compared with the reverse bias case because the resonant condition is located at lower voltages.

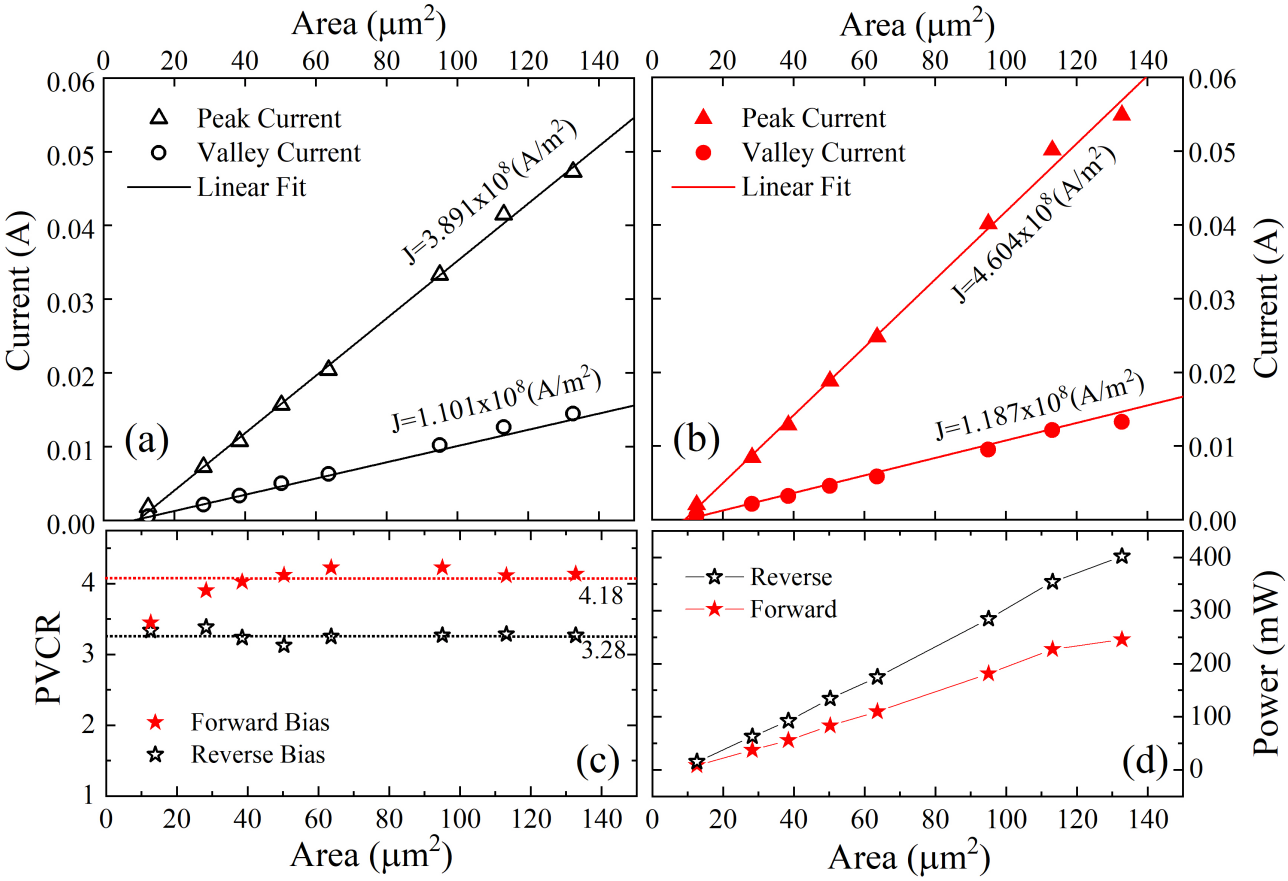

Figure 6.2: For $t_b = 1.5$ nm sample: Peak (triangles) and Valley (circles) currents as a function of the diode area at (a) reverse (black) and (b) forward (red) bias voltages. (c) Peak-to-valley current ratio (PVCR), and (d) Electrical power calculated at the peak of resonance, for forward bias (red stars) and reverse (black stars) as a function of the diode area.

Figure 6.3 (a) presents the RTD current-voltage density (J (V)) characteristics of the $t_b = 2.5$ nm sample at forward and reverse bias, obtained at 4K. Here is presenting the J(V) for diode diameter d = 9 μm only, because resonant tunneling was not observed for

all diameters, as in the sample previously presented. Comparing with this sample, yet, the resonances appear at lower voltages, around 3 V and -6 V and the density current is one order of magnitude smaller. Figure 6.3 (b) presents the linear behavior of the peak

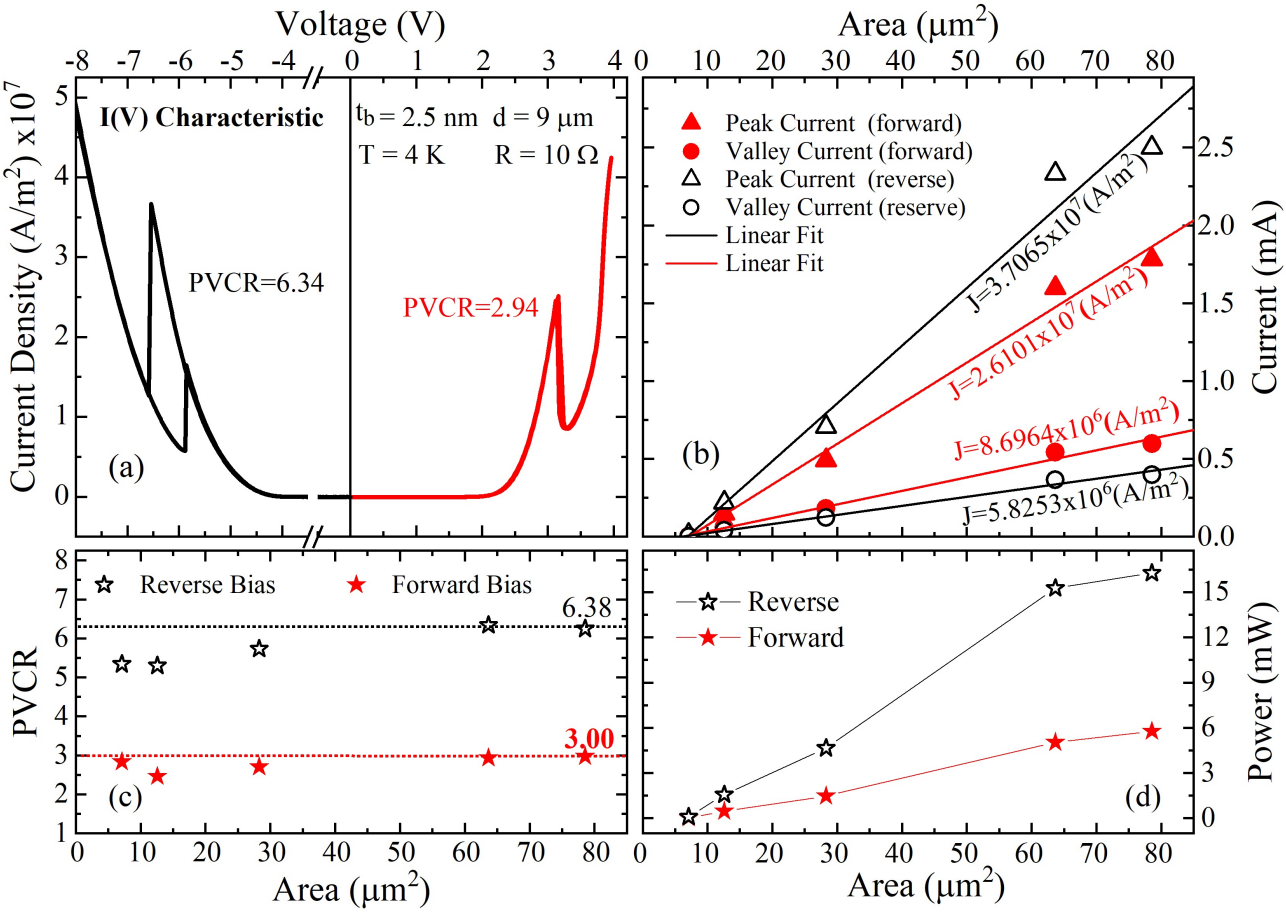

Figure 6.3: (a) Density current-voltage (J(V)) characteristic at forward and reverse bias of the $t_b = 2.5$ nm sample and diameter d = 9 μm, obtained at 4 K. (b) Peak (triangles) and Valley (circles) electrical current as a function of area, for reverse (black and empty symbols) and forward bias (red and full symbols), respectively. (c) peak-to-valley current ratio (PVCR), and (d) electrical power calculated at the peak of resonance. For forward bias (red stars) and reverse (black stars) as a function of the diode area.

and valley current as a function of the area, at the reverse and forward bias, respectively. Despite there is not a complete mapping regarding different diameters, the peak current scales almost linearly with the area, and the current density peaks are around J(V)= 3.7×10^7 A/m^2 at reverse bias voltage, and J(V)= 2.6×10^7 A/m^2. In addition, the NDC was observed for all diodes that showed an electric response, at reverse bias with PVCR=6.38 and forward bias with a PVCR=3, see Figure 6.3 (C). Finally, Figure 6.3 (d) presents the (nearly linear) electrical power calculated at the peak of resonance. The

values of peak-current power at forward bias are lower when compared with the reverse bias case because the resonant condition is located at lower voltages.

Figure 6.4 (a) displays the RTD current-voltage density (J (V)) characteristics of the t_b = 3.5 nm sample at forward and reversed bias, obtained at 4K. Similarly, as in the previous sample, not all the diodes exhibit resonant tunneling; therefore, the result of J (V) is being presented only for the diode diameter d = 6 μm. Any diode presented a well-defined current-voltage characteristic at forward bias; instead, it is observed a "shoulder" around 3 V (that did not allow a full analysis in this voltage region). Comparing with the two samples already presented, the resonances appear at lower voltages around -5.5 V and lower current densities (3 and 2 orders of magnitude). Figure 6.4 (b) displays

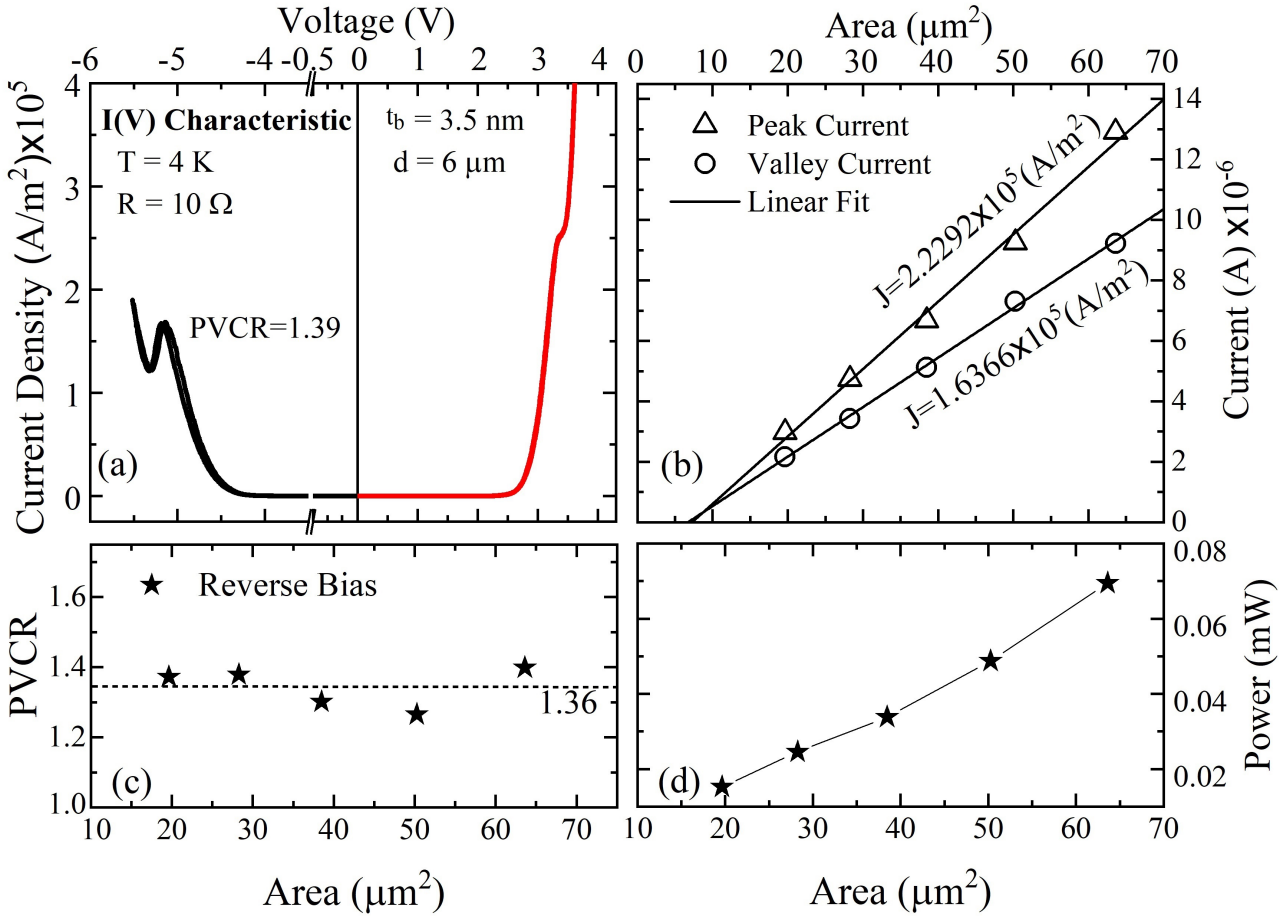

Figure 6.4: (a) Density current-voltage (J(V)) characteristic at forward and reverse bias of the t_b = 3.5 nm sample and diameter d = 6 μm, obtained at 4 K. (b) Peak (triangles) and Valley (circles) Current as a function of area, for reverse bias (black and empty symbols). (c) Peak-to-valley current ratio (PVCR), and (d) Electrical power calculated at the peak of resonance, for reverse bias (black stars) as a function of the diode area.

the linear behavior of the current peak and valley as a function of the area at reverse bias. Notwithstanding there is not a complete mapping regarding different diameters and voltage range, at the reverse bias case it can be seen that the peak as the valley current, scales almost linearly with the area, with current densities around $J(V)_{peak} = 2.2 \times 10^5 (A/m^2)$ and $J(V)_{valley} = 1.6 \times 10^5$ A/m^2. Furthermore, the NDC was observed for all diodes that showed an electric response at reverse bias with a PVCR ≈ 1.36 as shown in Figure 6.4 (C). Finally, Figure 6.4 (d) presents the electrical power calculated at the peak of resonance at the reverse bias condition.

6.1.1 Barrier thickness dependence

Since high current density is one of the upmost significant properties for high bandwidth operation devices, in the case of RTD, the current density is an essential feature in diode operation relying on their use and can be tuned by varying the height and the thickness of the barriers. Therefore, a final part of this study is on the effect of the barrier thickness over the current densities of the RTD-QDs. Figure 6.5 is summarizing a systematic study of the resonant tunneling injection across three different samples with differing AlAs barriers thickness (t_b = 1.5, 2.5, and 3.5 nm). The mean resonance current density J_{peak} calculated from the preliminary analysis for each of the grown structures were considered.

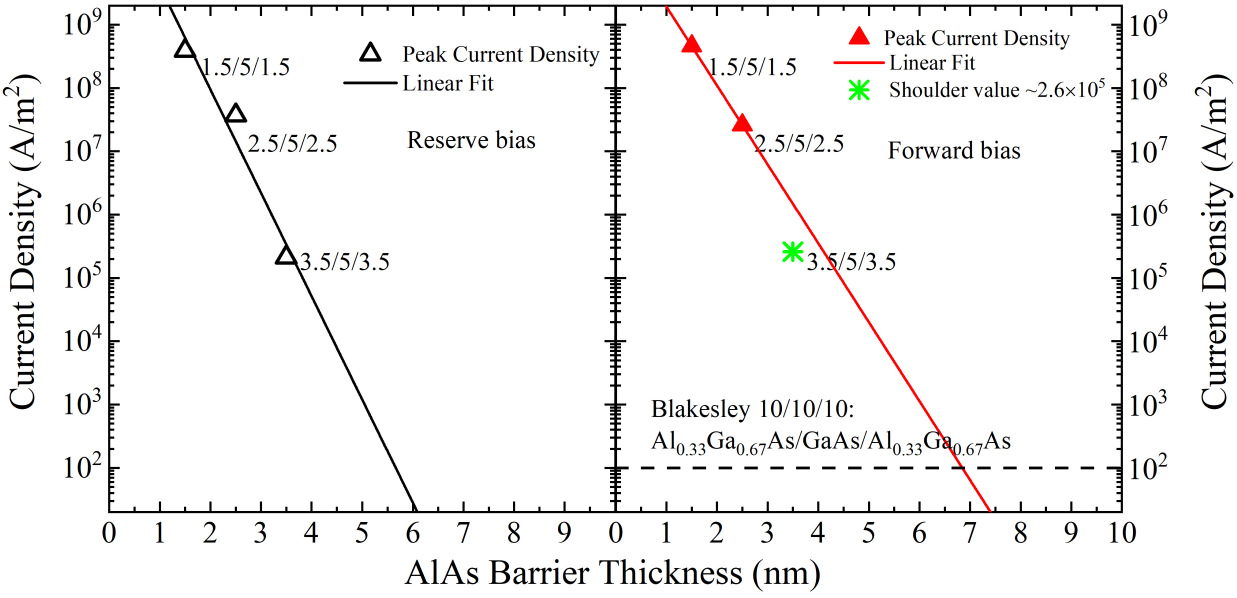

Figure 6.5: Resonance current density as a function of the AlAs barrier thickness, for both, reverse (black empy triangles) and forward bias (full red triangles). The dashed line is indicating the peak current density value reported by Blakesly on similar RTDs with thicker DBS [58].

From the graph above, it can be seen that the peak current-density (J_{peak}) for both forward and reverse bias exhibits a strong modulation as a function of barrier thickness, with nearly exponential dependence. The intensity of the tunneling current is decreasing several orders of magnitude as increasing the thickness of the tunneling barriers. By reducing the AlAs barriers' thickness from 2.5 to 1.5 nm, the peak current density increases from 2.6×10^7 to 4.6×10^8 A/m^2 for forward bias, and from 3.7×10^7 to 3.9×10^8 A/m^2 for reverse bias condition. Besides that, when reducing the thickness from 3.5 to 2.5 nm, the peak current density increases from 2.3×10^5 to 2.6×10^7 A/m^2 (reverse bias condition only). From Figures 6.2 (c) and 6.3 (c), it is also clear that the average PVCR of 4 and 3, respectively, is higher for the RDT with the thinnest barriers. This may be due to the high-resonance voltage, V_{peak} = 4.5 V, which limits the injection of excess current across the active region. In addition to the strong modulation in electron transmission, thicker barriers will also generate higher ground-state energies. Self-consistent calculations indicate an energy change of approximately 100 meV per monolayer, assuming symmetric barriers. Consequently, the resonant peak is expected to occur at larger peak voltages for devices with thicker tunneling barriers.

6.2 Optical properties

Figure 6.6 shows the calculated band structure with the conduction and valence energy band diagram of the RTD with integrated InGaAs QDs, employed in these experiments.

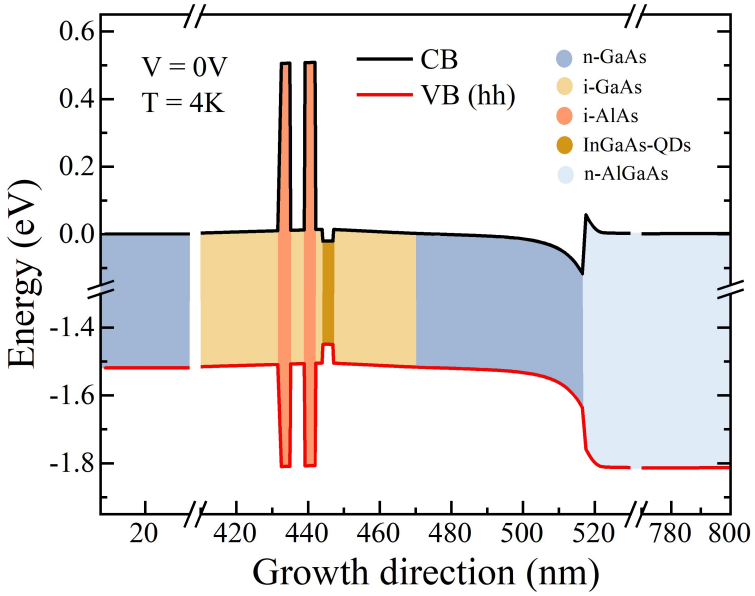

Figure 6.6: Simulated conduction band (CB) minimum and valence band (VB) maximum for the GaAs/AlGaAs QD-RTD.

The RTD heterostructure comprises five parts: the doped contact GaAs layers are shaded grey; the undoped GaAs spacer layers and QW are shaded pale-yellow; the AlAs barrier are shaded coral; the QDs layer is shaded bronze and the AlGaAs optical window (OW) is shaded in light-blue. The OW is intentionally grown with a higher bandgap than the absorber to allow optical access to the active RTD region.

After the basic electrical characterization, optical spectroscopy and photocurrent analyses will be focus only on the 2.5 nm barrier sample. Although it is interesting to work with high current densities, it is also a desirable parameter that the resonance of electric current occurs at the lower voltage values possible, considering that the diodes were designed to operate as photodetectors.

Figure 6.7 shows the μ-Photoluminescence (μ-PL) spectrum of the QD-RTD obtained at 13 K using a laser wavelength of $\lambda = 532$ nm and 5 μW of excitation power. The Figure shows the AlGaAs (OW) emissions at the high-energy side, the GaAs barriers and spacing layers at a wavelength of $\lambda \approx 820$ nm, following the band identified as the wetting layer, and the InGaAs QDs between the region of 860 - 930 nm [120, 121].

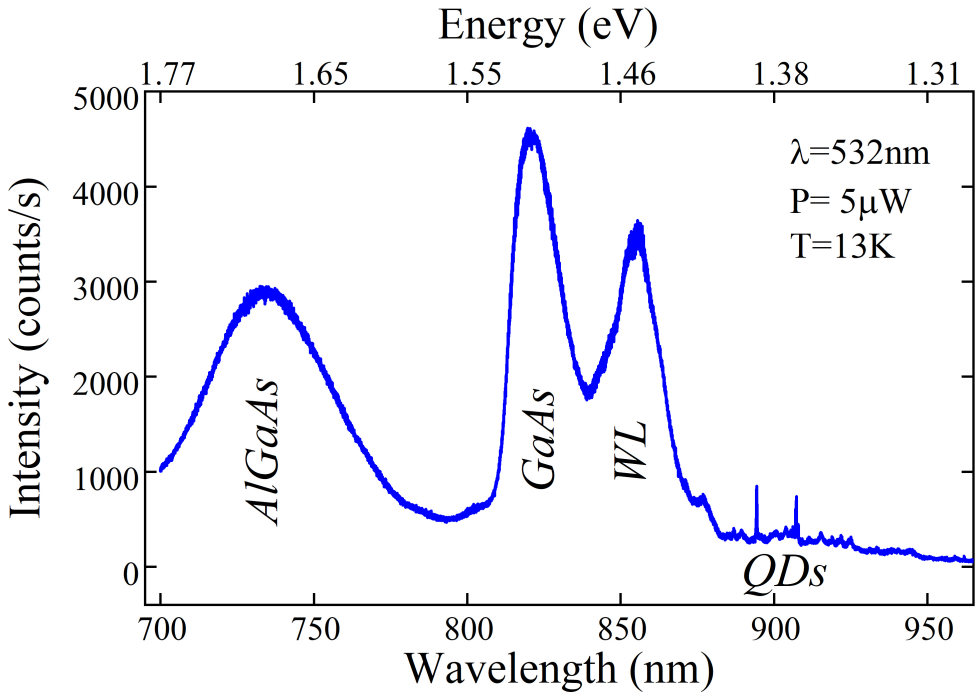

Figure 6.7: Micro-photoluminescence spectrum showing the optical window, GaAs layers, wetting layer and QDs emissions.

The μ-PL spectra of Figure 6.8(a) present the QDs emissions lines obtained for all diameters diodes (4 - 13 μm) from the QD-RTD. InGaAs QDs emissions have been de-

tected in the wavelength range from 860 up to 930 nm, which is in between 1.33 - 1.43 eV. Figure 6.8(b) displays a single QD emission line at 904 nm, and a Gauss fit is used to find parameters as the linewidth.

Figure 6.8(c) presents the linewidth obtained from the analysis of each spectrum as a function of the diode diameter, with linewidths of around 300 μeV. This outcome confirms the presence of optically active InGaAs QDs. Single quantum dot μ-PL emission additional indicates that the QDs can be used for charge trapping of optically generated charge carriers, confining electrons, and holes. As a consequence, the QDs could act as a trap for single photogenerated charge carriers.

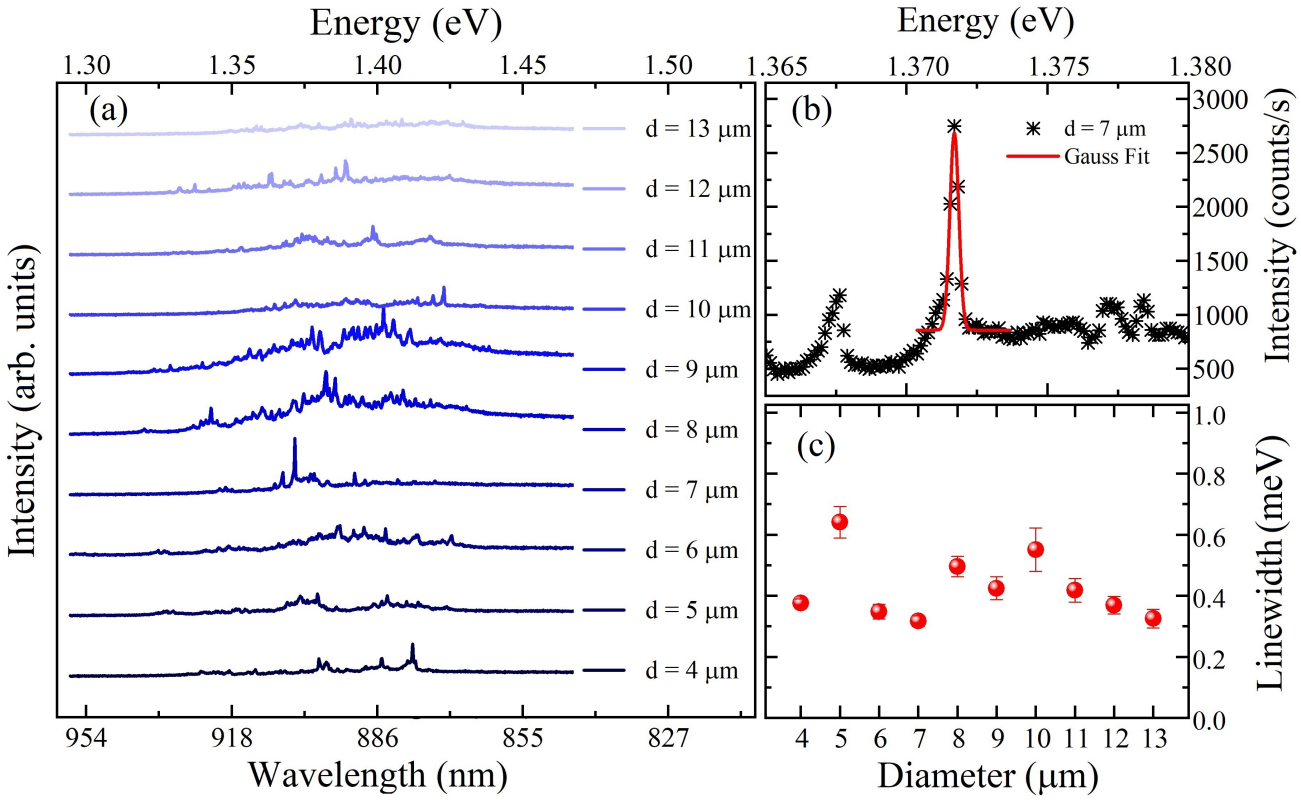

Figure 6.8: (a) μ-PL emission spectra showing single QDs emission lines. (b) Single QD emission (black asterisk). The used Gauss fit (red line). (c) Linewidth as a function of diode diameter.

After verifying the aptitude of QDs to act as charge carrier traps via μ-PL emission of QDs in this heterostructure, the RTD is studied as a photodetector, evaluating the RTD current-voltage (I(V)) characteristic curve under illumination. It is worth highlighting that the absorption layers (collector n-GaAs side and n-AlGaAS optical window) are

highly doped precisely to enhance the photogeneration of charge carriers.

6.3 Optoelectronic properties

To study the optoelectronic transport properties of the QD-RTD photodetector, current-voltage characteristics of a diode with diameter d = 9 μm were carried out in the dark and under illumination. At the same time, the QDs emissions were investigated as a function of the applied voltages. Figure 6.9 presents the results of the influence of the electric field on the emission characteristics of the QDs.

Figure 6.9 (a) shows the I(V)-characteristics measured for positive and negative bias in the dark and under illumination (U.I.) using a laser wavelength of λ = 750 nm, and power P = 3μW. The I(V)-characteristics display exponential growth of current, a well pronounced NDC region and bistability. For positive bias in the dark, the resonance current and voltage for the up-sweep direction are I_{peak} = 1.58 mA and V_{res} = 3.47 V, whereas valley current and voltage for the down-sweep direction are I_{val} = 0.57 mA and V_{val} = 3.45 V. The peak to valley current ratio is PVCR = 2.77. For the opposite bias voltage direction in the dark, the resonance current and voltage for the up-sweep direction are I_{peak} = 1.96 mA and V_{peak} = −7.60 V and the valley current and voltage down-sweep direction are I_{val} = 0.38 mA and V_{val} = −6.97 V. The peak to valley current ratio is PVCR = 5.15. For negative bias, no photosensitivity was observed, following that, no photogenerated carriers accumulate, therefore, no photocurrent in this voltage region occurs. Underwriting that it is the voltage region in which the diodes were designed to operate. Figures 6.9 (b) and (c) presents the μ-Photoluminescence spectra measured when the RTD is under applied voltages from −3.3 V up to 0.9V, showing sharp and discrete emission lines from the QDs. Peaks 1 and 2 represents quality QDs emissions. When increasing the applied positive voltage, QDs intensity emissions increase, followed by a red-shift up to 0.7 V, where the light emission vanishes. While increasing the negative voltage, the intensity remains constant following a blue shift and vanishing at voltages of $\sim$ 3.3 V. The deconvolution results for peaks 1 and 2 are presented in Figures 6.9 (d) and (e), showing the variation of the emissions intensity and variation of the peak position as a function of the applied voltage, respectively.

This result is significant because a strong influence on the local electrostatic potential is noticeable. Even with minor changes in the electric field, the emissions characteristics of the quantum dots are notably affected, i.e., quenching the QDs light emission for voltages above 0.9 V in the positive bias and above −3.3 V in the negative bias where no current is flowing yet. Thus, it could be possible to manipulate the charge carrier dynamics in this low voltage region, where the QDs are optically active.

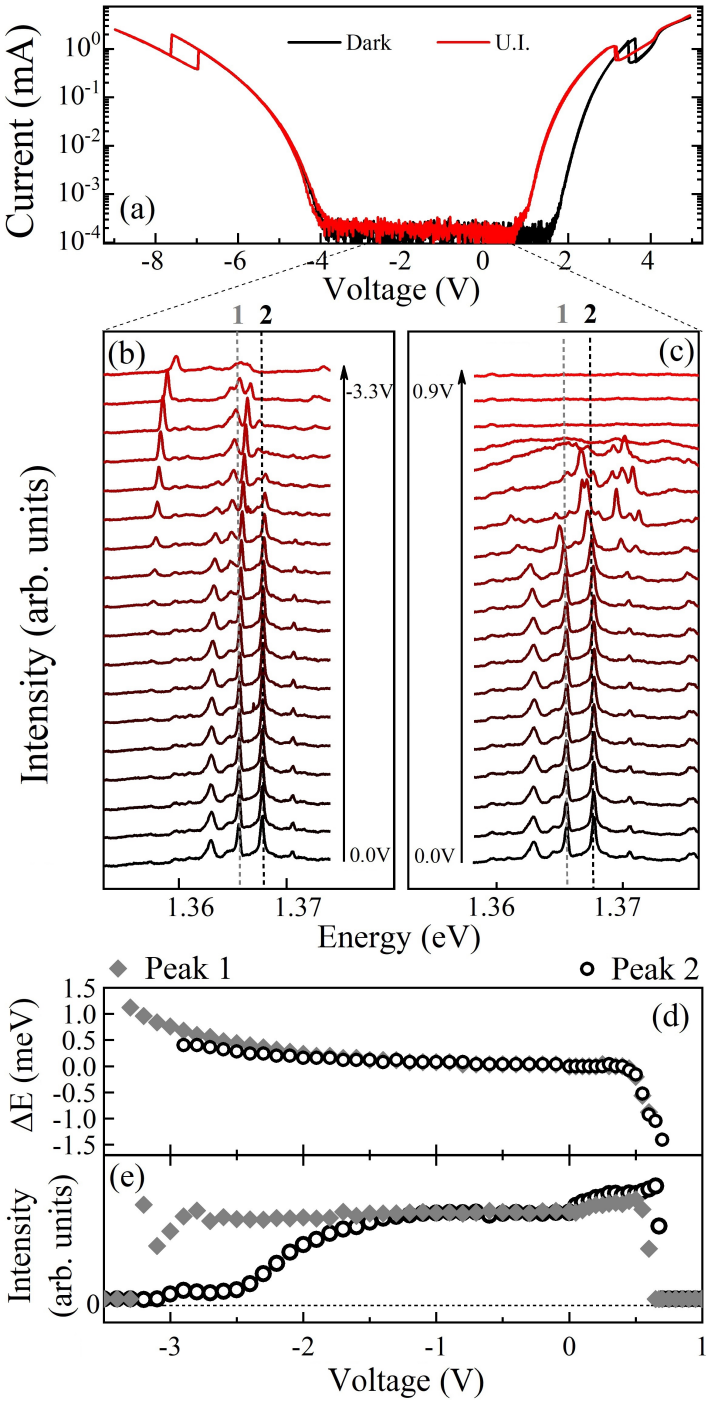

Figure 6.9: (a) I(V)-characteristics for positive and negative bias in the dark and under illumination. (b), (c) QDs μ-PL spectra measured under applied voltages from -3.3V to 0.9V. Variation of (d) Intensity and (e) Peak position as a function of the applied voltage for peak 1 (full gray diamonds) and peak 2 (empty black holes).

To increase the reliability of the QD-RTD photodetection mechanism, I(V)-characteristics were repeated in the dark and under illumination for different excitation

wavelengths: λ = 750, 800, 850 and 900 nm, and using different laser powers from P = 15 nW up to P = 30 μW (depending on each case). All measurements were carried out at a cryogenic temperature of T = 2 K, using a resistance of 10 Ω, for positive and negative voltage sweeps from V = -9 V to V= 5 V. Figures 6.10 (a), (b), (c) and (d) shows the I(V)-characteristics obtained in the dark (solid black lines) and under illumination (solid

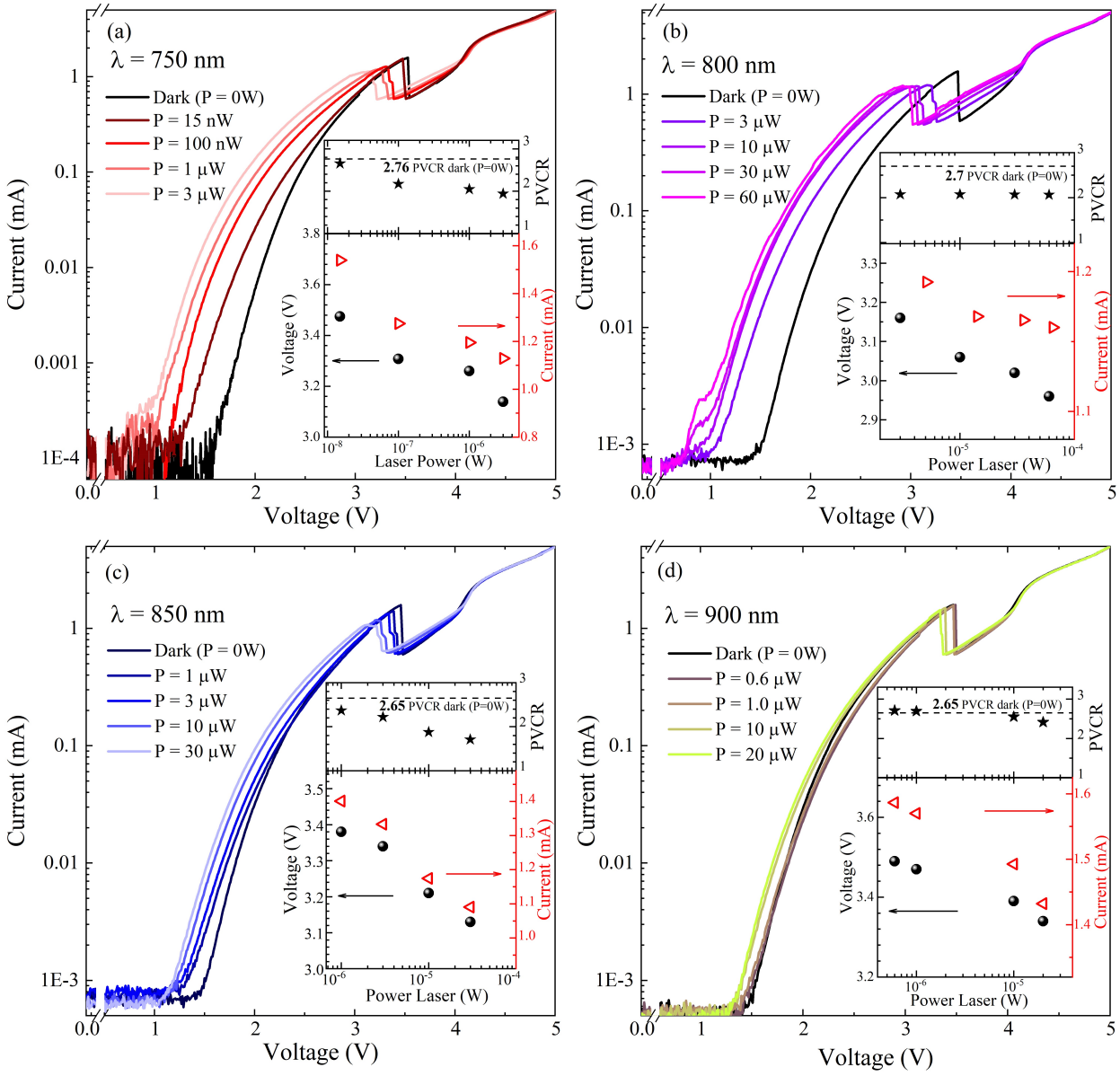

Figure 6.10: I(V)-characteristics in the dark and under illumination for different power lasers and wavelengths: (a) λ=750 nm, (b) λ=800 nm, (c) λ=850 nm, (d) λ=900 nm. The insets are showing the voltage (left black side) and current (red right side) values at the peak of resonance and the PVCR (upper panel) as a function of the laser power.

colored lines) for different power lasers at the excitation laser wavelengths of λ = 750, 800, 850 and 900 nm, respectively.

The I(V)-characteristics show a PVCR strongly dependent on the laser power, and a current line shape above 4.5 V. In all cases, the voltage, peak current and PVCR decrease with increasing laser power, and the results of this dependence with the laser power are shown in the inset of each figure. When illuminated, electron-hole pairs are generated by absorption of incident photons (photogenerated carriers). Due to the applied electric field, the photogenerated carriers drift along with the RTD. The photogenerated holes, for example, can accumulate in the vicinity of the DBS and be captured by the QDs, enhancing the local electric field, consequently inducing an additional voltage drop across the DBS; this causes a displacement of the I(V)-characteristics to lower voltages inducing a voltage shift (ΔV) as observed in the Figures 6.10 (a)-(d).

The results are exposed only for positive bias to summarize all the obtained results since the photocurrent almost totally vanishes for negative bias because, as previously mentioned, no photogenerated carrier accumulation occurs. Apparently the higher the energy of the laser and the higher its power, the higher the voltage shift. So, there is a directly proportional relationship between the excitation power and energy with the accumulated and trapped photogenerated carriers. The most noticeable change in the I(V) curve was obtained in the case under illumination with a laser of $\lambda = 800$ nm, and with this excitation wavelength, the higher incident laser power (P = 60μW) was used. Given that under these conditions, a "shoulder" was observed in the low-voltage region of I(V), which indicates a possible accumulation of holes. The following discussion will focus on this case.

Figure 6.11 (a) shows the photocurrent results comparing the I(V)-characteristics obtained in the dark (solid black line) and under illumination (solid pink line) using a laser of wavelength $\lambda = 800$ nm and a power of P = 60 μW. The inset shows a comparison of the I(V)-characteristic obtained experimentally in the dark and a theoretical I(V) obtained by adjusting the experimental one using Schulman's equation:

$$J(V) = A \ln \left[\left(\frac{1 + \exp^{\frac{(E_f - E_r + eV/2)}{k_B T}}}{1 + \exp^{\frac{\left(E_f - E_r - eV/2\right)}{k_B T}}} \right) \right] \left[\frac{\pi}{2} + \mathrm{Tan}^{-1} \left(\frac{E_r - eV/2}{D} \right) \right] \tag{6.1}$$

The purpose is to analyze the changes in the I(V)-characteristics after resonance, where the dark and under illumination (U.I.) curves are almost the same; however, both exhibit unusual (line-shape) behavior above 4.5 V. Thus, Schulman's expression has been used to fit the experimental I(V) curve essentially after resonance, with the idea of using it as a

"theoretical" curve to obtain a ΔV for both cases dark and under illumination.

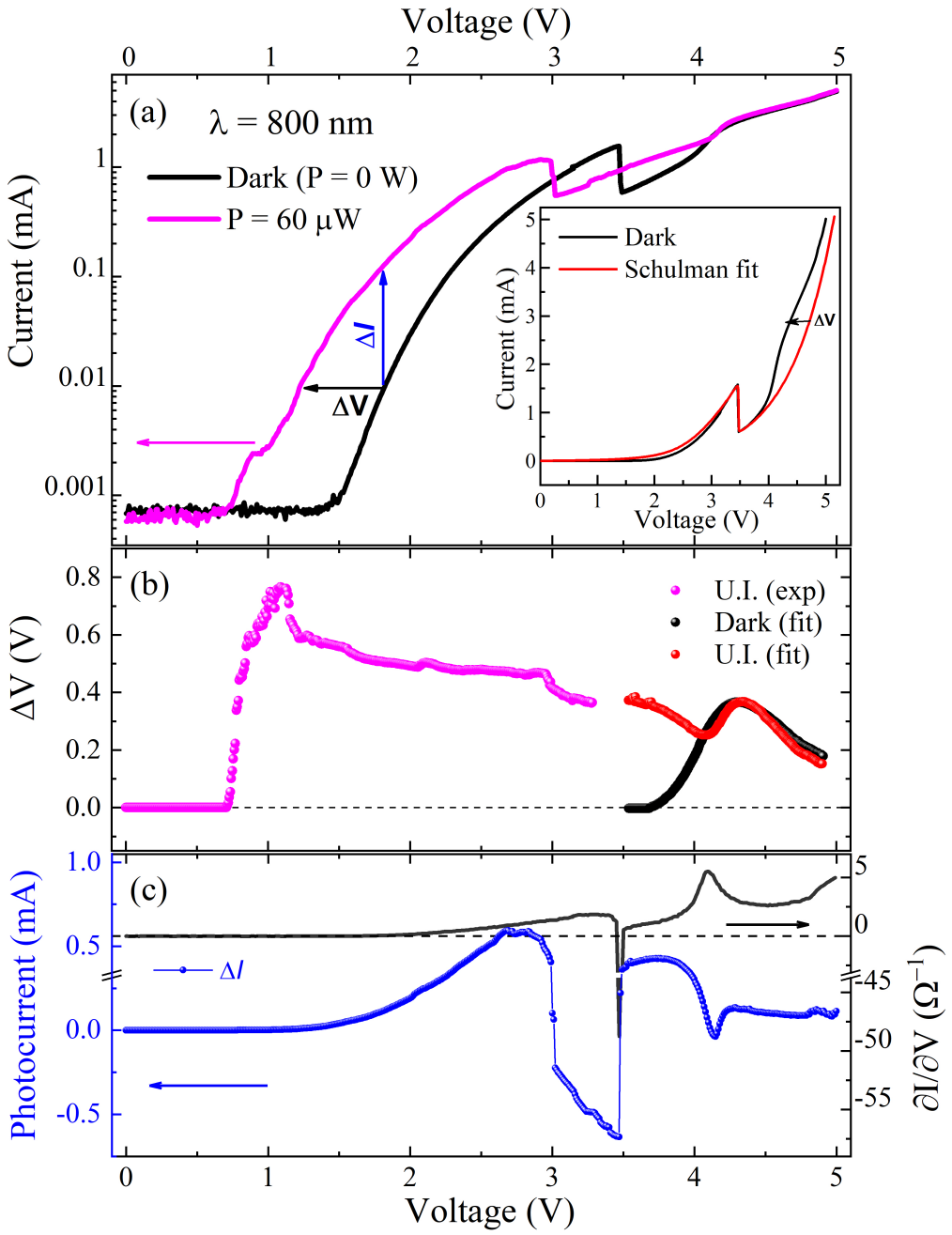

Figure 6.11: As a function of the applied voltage (a) I(V)-characteristics measured in the dark (solid black line) and under illumination (solid pink line) with a laser of λ=800 nm and using a power of 60 μW. Inset: I(V) in the dark used to obtain an I(V) fitting curve (solid red line). (b) Voltage shift ΔV. Experimentally photoinduced (pink spheres) and obtained from subtracting the I(V) fitting curve for both I(V) in the dark (black spheres) and under illumination (red spheres) (c) Left: photocurrent-voltage relation. Right: first derivative of the dark I(V) curve.

The ΔV was calculated by subtracting the voltages for dark experiments from the voltages under illumination for the same current value. Figure 6.11 (b) presents the ΔV obtained experimentally (pink spheres) and the obtained by subtracting the fitting curve from both in the dark (black spheres) and under illumination (red spheres) as a function of the applied voltage. The ΔV is a nonlinear function of V with a maximum of $\sim$ 0.78 V at V = 1.1 V and an apparent flat range between 1.5 and 3 V where the change in ΔV is minimal ($\sim$ 0.07V), allowing to assume that, in fact, the accumulated charges remain trapped for a period of time or voltage. The photocurrent was estimated by subtracting the current in the dark from the current under illumination for equal voltage values. The resulting photocurrent-voltage correlation is depicted in Figure 6.11 (c-left) as a blue line. The photocurrent is also a nonlinear function of V, with a maximum of $\sim$ 0.58 mA at V = 2.7 V (blue spheres). Finally, Figure 6.11 (c-right) shows as a black line the first derivative of the dark I(V) curve, the inflection changes in the curve can indicate different events occurring in the carrier transport that are not so evident in the I(V)-characteristic curve.

The correlation between the I(V)s, obtained in the dark with the EL emissions are presented in Figure 6.12 (a) and (b), respectively. As it could be observed in Figure 6.10, at voltages $V \gtrsim 4$V, the photo-induced voltage shift of the I(V) under illumination disappears, and the onset of electroluminescence (EL) emission can be observed (shown in Figure 6.12 (b)). After exceeding this critical voltage value, new charge carriers are created via the impact ionization process on the collector side. Due to the electric field, these carriers can go through the structure; electrons may continue their way to the top contact or accumulate at the OW junction barrier. While holes, as previously discussed, can accumulate in the vicinity of the DBS and even get trapped by the QDs. However, since EL emissions have been observed, recombination processes of electron-hole pairs across the structure are happening; given that the main EL emission observed come from the GaAs layer, it is assumed that the electrons accumulated at the OW junction recombine with the recently created holes that are on their way to the DBS. Nevertheless, the voltage threshold at which EL occurs is sufficiently high to assume that holes can tunnel resonantly to the emitter side, where they can also recombine with electrons. These processes have attributed the ΔV found at high voltages under the theoretical curve comparison.

As previously discussed, the QD-RTD under illumination and biased with an applied voltage generate electron-hole pairs; some are photogenerated, others created by impact ionization processes, and all spatially distributed due to the applied electric field. As a result, the I(V)-characteristic shifts to lower voltages, here interpreted as ΔV caused by the accumulation of the generated charge carriers. However, this implies an optimal working point as a photodetector where the charge carrier accumulation mechanism

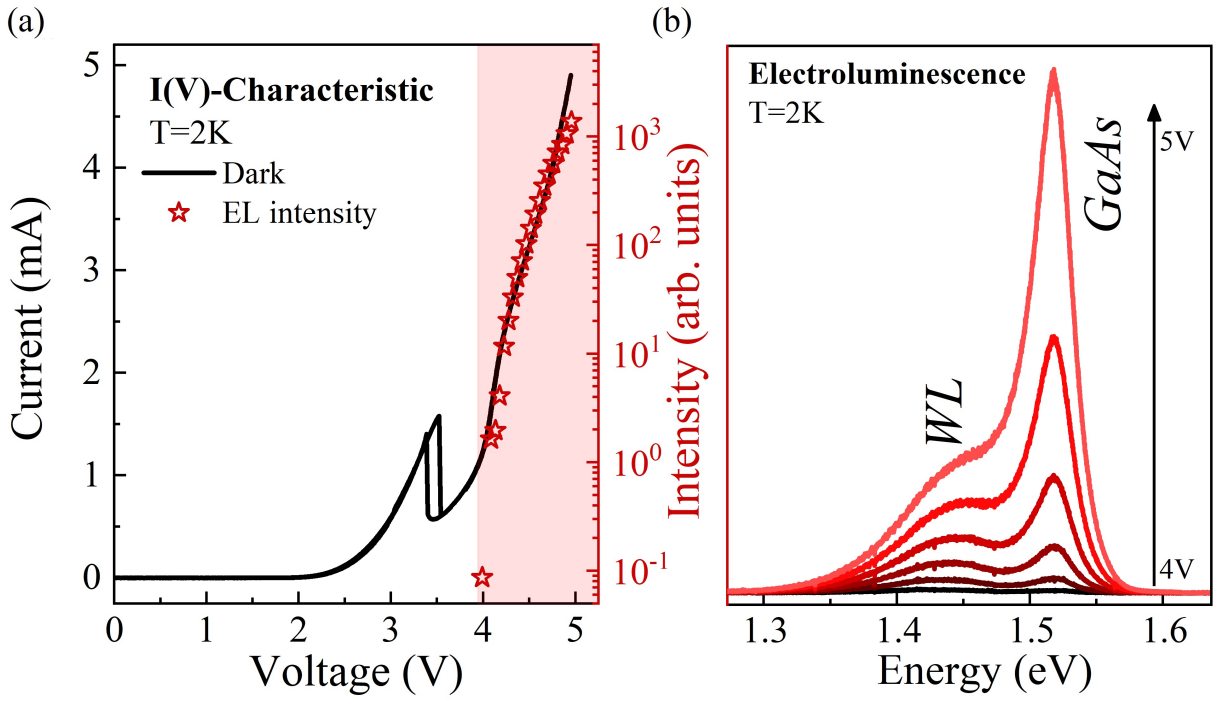

Figure 6.12: As a function of the applied voltage (a) Black Left side: I(V)-characteristics measured in the dark (solid black line). Red right side: EL integrated intensity (red empty stars). (c) Electroluminescence spectra collected for voltages $V \gtrsim 4$V

offsets recombination processes. Different experimental and theoretical approaches have been carried out to explain how the accumulation of photogenerated charge carriers that produces a photoinduced voltage shift ΔV is proportional to the number of accumulated charges [43, 122, 123]. In this thesis, a more straightforward analysis to explain how the accumulation of the photogenerated charge carriers within the device produces a voltage shift is proposed.

6.3.1 Theoretical method

To explain how the voltage drop occurs throughout the heterostructure, a fundamental theoretical assumption is considered; based on the fact that the potential accumulated charge carriers come from the doped layers or are photogenerated or come from impact ionization processes. Under an applied forward bias voltage along the z-direction, as depicted by the + and − signs in Figure 6.13 (a) and under external laser excitation from the top of the RTD. The following assumptions are made:

1. Electrons from the emitter side traveling through the QD-RTD to the collector side can accumulate before the DBS producing the initial potential energy drop.

2. The applied voltage can ionize segments of the doped regions (N_{D1}^{+}, N_{D2}^{+}), thus generating depletion regions on the collector side.

3. Photogenerated carriers by an incident light produce electrostatic effects, such as bending the energy profile. Furthermore, due to these electric field interactions, they can drift along with the RTD.

4. The photogenerated holes build up close to the collector barrier at the DBS and get captured by the QDs where they reside apparently for a considerable period of time or until the electric field distorts the potential sufficiently to promote other escape channels. Besides contributing with an additional voltage drop across the DBS.

5. The photogenerated electrons, on the other hand, can accumulate at the optical window junction.

Carrying out all these assumptions, the understanding of the accumulated charge density distribution (ρ) along the growth direction, as illustrated in Figure 6.13 (b), can be formed. An initial accumulation of electrons (n_0) near the emitter barrier, photogenerated holes accumulated near the colletor side barrier and trapped by the QDs (P_{QD}), and photogenerated electrons accumulated in the OW junction (n_j) will generate two-dimensional carrier distributions. On the other hand, on the collector side, the absorption layer and the OW can be partially depleted with a length l_1 and l_2, respectively, generating three-dimensional accumulated charge carrier distributions (N_{D1}^{+}) and (N_{D2}^{+}) due to the ionization of these highly doped layers individually in the given order.

The produced electric field along the growth direction is also represented (see Figure 6.13 (c)) and can be calculated using Gauss's law at each region:

$$\nabla \cdot \vec{F} = \frac{\rho}{\varepsilon} \tag{6.2}$$

Subsequently, all the accumulated charge density should be in equilibrium throughout the device; hence, the following neutrality conditions must be assumed: $n_0 = P_{QD} + N_{D1}^{+} l_1$ and $n_j = N_{D2}^{+} l_2$. After that, the voltage drop for each region can be estimated by solving Poisson's equation given by:

$$\nabla^2 V = \frac{-\rho(z)}{\varepsilon}. \tag{6.3}$$

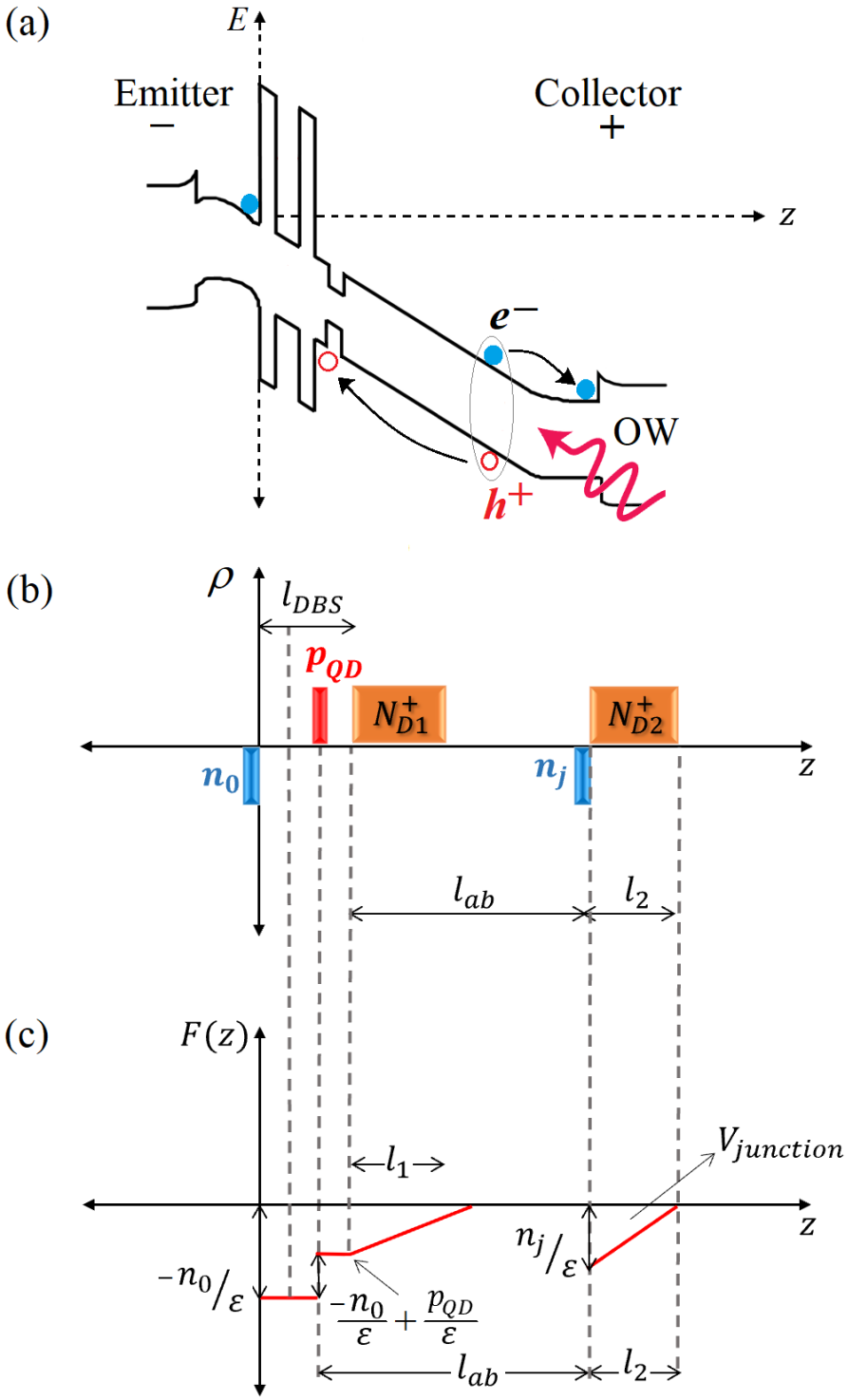

Figure 6.13: Schematic representation as a function of the growth direction of the (a) profile energy band, (b) accumulated charge carrier density distribution and (c) electric field within the QD-RTD under an applied forward voltage and under illumination.

At the same time that the total voltage drop should be given by:

$$V_T = V_{DBS} + V_{QD} + V_{l_1} + V_j \tag{6.4}$$

where, V_{DBS} is the voltage drop at the DBS, V_{QD} the voltage drop due to the trapped charges at the QDs, V_{l_1} the voltage drop at the first depletion layer and V_j the voltage drop at the junction (see Figure 6.13 (c)), the resulting total voltage drop within the device is:

$$V_T = \frac{-n_0 l_{DBS}}{\varepsilon} + \left(\frac{-n_0}{\varepsilon} + \frac{P_{QD}}{\varepsilon}\right) l_{DBS} + \left(\frac{-n_0}{\varepsilon} + \frac{P_{QD}}{\varepsilon}\right) \frac{l_1}{2} + \frac{-n_j}{\varepsilon} \frac{l_2}{2}. \tag{6.5}$$

Using the neutrality conditions $l_1 = \frac{n_0 - P_{QD}}{N_{D1}^+}$ and $l_2 = \frac{n_j}{N_{D2}^+}$, the total voltage drop takes the form:

$$V_T = \frac{-n_0 l_{DBS}}{\varepsilon} - \frac{-n_0^2}{2\varepsilon N_{D1}^+} + \frac{P_{QD} l_{DBS}}{\varepsilon} + \frac{n_0 P_{QD}}{\varepsilon N_{D1}^+} - \frac{P_{QD}^2}{\varepsilon N_{D1}^+} - \frac{n_j^2}{\varepsilon N_{D1}^+}. \tag{6.6}$$

From here is more explicit the form of each one of the components; for instance,

$$V_0 = \frac{-n_0^2}{2\varepsilon N_{D1}^+}, \quad V_{DBS} = \frac{-n_0 l_{DBS}}{\varepsilon}, \quad V_{QD} = \frac{P_{QD} l_{DBS}}{\varepsilon} + \frac{n_0 P_{QD}}{\varepsilon N_{D1}^+} - \frac{P_{QD}^2}{\varepsilon N_{D1}^+}, \quad V_j = \frac{-n_j^2}{\varepsilon N_{D1}^+}$$

where, V_0 is then considered as the voltage produced by the accumulation of charge in the absorption region when there is no incident light.

Supposing that there is not any incident light, $V_{QD} = 0$ and that $V_j = 0$,

$$\frac{-n_0^2}{2\varepsilon N_{D1}^+} + \frac{-n_0 l_{DBS}}{\varepsilon} - V = 0$$

Solving n_0 by using the quadratic function,

$$n_0(V) = -N_{D1}^+ \left(l_{DBS} - \sqrt{(l_{DBS})^2 - \frac{2\varepsilon V}{N_{D1}^+}}\right) \tag{6.7}$$

Following this, the dependence of V_{DBS} on V can be expressed more clearly, resulting in,

$$V_{DBS}(V) = \frac{-N_{D1}^{+}\left(l_{DBS} - \sqrt{(l_{DBS})^2 - \frac{2\varepsilon V}{N_{D1}^{+}}}\right)}{\varepsilon} \tag{6.8}$$

Figure 6.14 (a) display the obtained dependencies of the initial accumulation charge n_0 and the voltage drop at the DBS V_{DBS} with the total applied bias voltage ($V_T = V$) calculated according to equations 6.7 and 6.8, respectively.

On the other hand, the transmission coefficient for a symmetrical DBS can be determined as $T(E) = 1/|\mathbf{M}_{11}|^2$, where, $\mathbf{M}_{11}$ is the *transfer matrix* that allows to calculates the transmission peaks, providing the necessary energies for the charge carriers (electrons) to tunnel resonantly into the DBS, as shown in the inset of Figure 6.14 (a) from the graph two resonant states are observed at the energy positions of 86 meV and 357 meV.

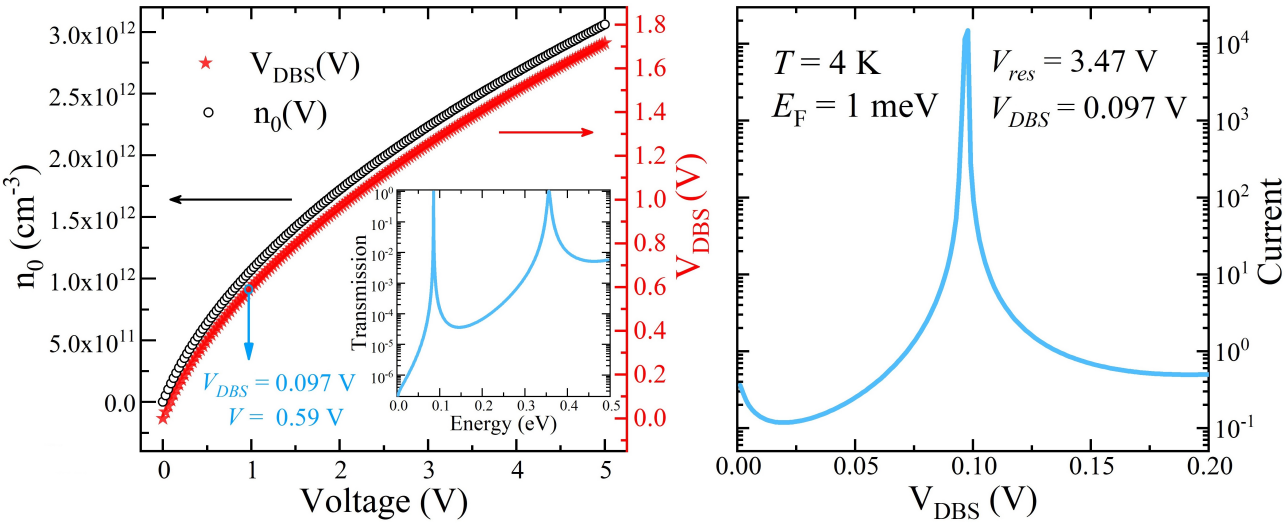

Figure 6.14: Calculated (a) as a function of the total applied voltage. Left black side: initial accumulation charge n_0 (empty black circles). Right red side: voltage drop at the DBS V_{DBS} (full red stars). Inset: simulated transmission for the obtained V_{DBS}. (b) Current as a function of V_{DBS} using the simulated transmission coefficient.

By using the transmission coefficient, the electrons' current was calculated as a function of the V_{DBS} according to eq. 2.4 as shown in Figure 6.14 (b), using a nominal value of Fermi-energy $E_F = 1$ meV and at $T = 4K$, the obtained current has a peak for the resonance for electrons at $V_{DBS} = 0.097$ V. Consequently, for a voltage drop of 0.097 V

at the DBS is required 0.59 V of the total voltage. Thus, of the 3.47 V (experimental resonance voltage) is needed for the resonance condition that around 2.88 V to drops at the junction (V_j). To find how V_j depends on V_T, a simple linear regression is assumed. From two points, a linear function that represents this dependence is obtained. If $V_j = 0$V when $V_T = 0$ V and $V_j = 2.88$ V when $V_T = 3.47$ V then it is obtained that $V_j = 0.83V_T$.

So far, almost all the terms in equation 6.6 have been developed in their dependence on the total voltage. However, the expression corresponding to the voltage drop due to trapped charges at the QDs is not that trivial. Thus, it is also necessary to consider that since the trapped charges in the QDs generate V_{QD}, produced when there is photoexcitation, V_{QD}, is the corresponding term for the photogenerated holes ($P_{QD} = P_{ph}$) and, since photogeneration of electrons (n_{ph}) is possible too, an additional term (which can be part of the n_j) must be considered. Consequently, ΔV takes the form:

$$\Delta V = \frac{P_{ph} l_{DBS}}{\varepsilon} + \frac{n_0 P_{ph}}{\varepsilon N_{D1}^{+}} - \frac{P_{ph}^2}{\varepsilon N_{D1}^{+}} - \frac{n_{ph}^2}{\varepsilon N_{D2}^{+}} \tag{6.9}$$

Then, let's defined $\Delta V = \Delta V_{ph}$ as the voltage shift produced by the build-up of photogenerated carriers, whose voltage dependence can be characterized by light absorption processes, as well as by trapping and transmission of photogenerated carriers. Thus, taking into account that the population of photocreated electrons can be determined as follow:

$$n_{ph} = P \cdot \alpha(\hbar\omega, V) \cdot \eta(V) \cdot \tau_e(V) + \Pi(V) \cdot \eta(V) \cdot \tau(V) \tag{6.10}$$

and the population of photocreated holes can be described as,

$$P_{ph} = P \cdot \alpha(\hbar\omega, V) \cdot \eta(V) \cdot \tau_h(V) + P \cdot \alpha(\hbar\omega, V) \cdot \eta_r(V) \cdot \tau_{hr}(V) + \Pi(V) \cdot \eta(V) \cdot \tau_h(V) \tag{6.11}$$

then the voltage dependence of ΔV becomes explicit. Here, P is the incident light power, $\alpha(\hbar\omega, V)$ is the absorption coefficient, η is the RTD quantum efficiency, τ_e and τ_h represents the rate of escape of the accumulated charge carriers at the DBS, and Π the impact ionization coefficient defined in eq.2.11. The first term of eq.6.10 and the two first of eq.6.11 are the fractions of light converted into successfully collected photogenerated carriers required to produced changes in the electrostatic potential. The mentioned functions are described as following [43, 124–126],

$$\eta(V) = \frac{1}{2}\left[1 + \mathrm{erf}\left(\frac{V - V_{th}}{\sqrt{2}\sigma_\eta}\right)\right] \tag{6.12}$$

$\eta(V)$ is a voltage-dependent function that follows an error function form. $\eta(V)$ is defined as the RTD quantum efficiency determined as the probability that an incident photon has to generate a charge carrier which will be captured and accumulated if V_{th} (voltage at which half of the maximum η is reached) exceed the built-in electrical field to yield efficient capture of photogenerated charge carriers around the DBS [124] σ_η, σ_α, γ and β are constants defined by material parameters and heterostructure design). The absorption is a strong function of voltage and optical excitation, subject to various saturation mechanisms of electron-hole pairs [126].

$$\alpha(\hbar\omega, V) = \frac{1}{2}\left[1 + \mathrm{erf}\left(\frac{\hbar\omega - E_g + \gamma V^2}{\sqrt{2}\sigma_\alpha}\right)\right] \tag{6.13}$$

τ_e and τ_h are determined by the mean lifetime of accumulated charge carriers at the DBS and defined as the inverse of the transmission coefficient T_e, T_h for electrons and holes, respectively.

$$\tau_h(V) = \frac{1}{T_h(V)}, \quad \tau_e(V) = \frac{1}{T_e(V)} \tag{6.14}$$

where,

$$T_h(V) = I_h^r \exp\left[-\frac{V_T - V_r}{2\sigma^2}\right] + I_h \exp\left(\beta_h V\right), \quad T_e(V) = I_e \exp(\beta_e V)$$

The mean lifetime of the accumulated carriers also depends strongly on the voltage since any variation in the photoinduced ΔV modifies the transmission probability; consequently, the half-life of the accumulated carriers and the resonant tunneling condition depends on ΔV as well [124]. Because of this, non-resonant and resonant transmissions (indicated by the r indexes) have been considered. However, the resonance current has been attributed only to photogenerated holes because the increase of accumulated holes by the QDs near the DBS can distort the potential, allowing them to tunnel resonantly through the first quantized heavy hole state of the double-barrier quantum well. In contrast, for electrons, only a non-resonant channel was considered.

The dependence of the photogenerated carriers with these parameters, which are all voltage-dependent, is then established. Figure 6.15 (a) and (b) shows the photogenerated-trapped electrons and holes, calculated by using equations 6.10 and 6.11, respectively. The dark condition (solid black line) concerns to the accumulated carries due to the impact

ionization process. The resonant transmission of holes explains the appearance of the photoresponse peak, as can be seen in Figure 6.15 (b). Figure 6.15 (c) displays the calculated voltage shift according to eq. 6.9 as a function of the number of photogenerated carriers in a colored contour gradient plot. For explicitness, P_{ph} and n_{ph} have been normalized to the electron density on the emitter side, n_0. Dark blue represents negative voltage shift, and red the highest calculated voltage shift. The calculations were made using parameters defined by material and device configuration, namely $N_{D1}^{+} = N_{D2}^{+} = 2 \times 10^{18}\text{cm}^{-3}$, $\varepsilon = 13.3$, $l_{DBS} = 2 \times 10^{-6}$ cm and $n_0 = 1.98 \times 10^{12}$ cm^{-3}. The contour line indicates zero voltage change, and the dashed line indicates the case when the amount of photocreated electrons and holes accumulated are equal.

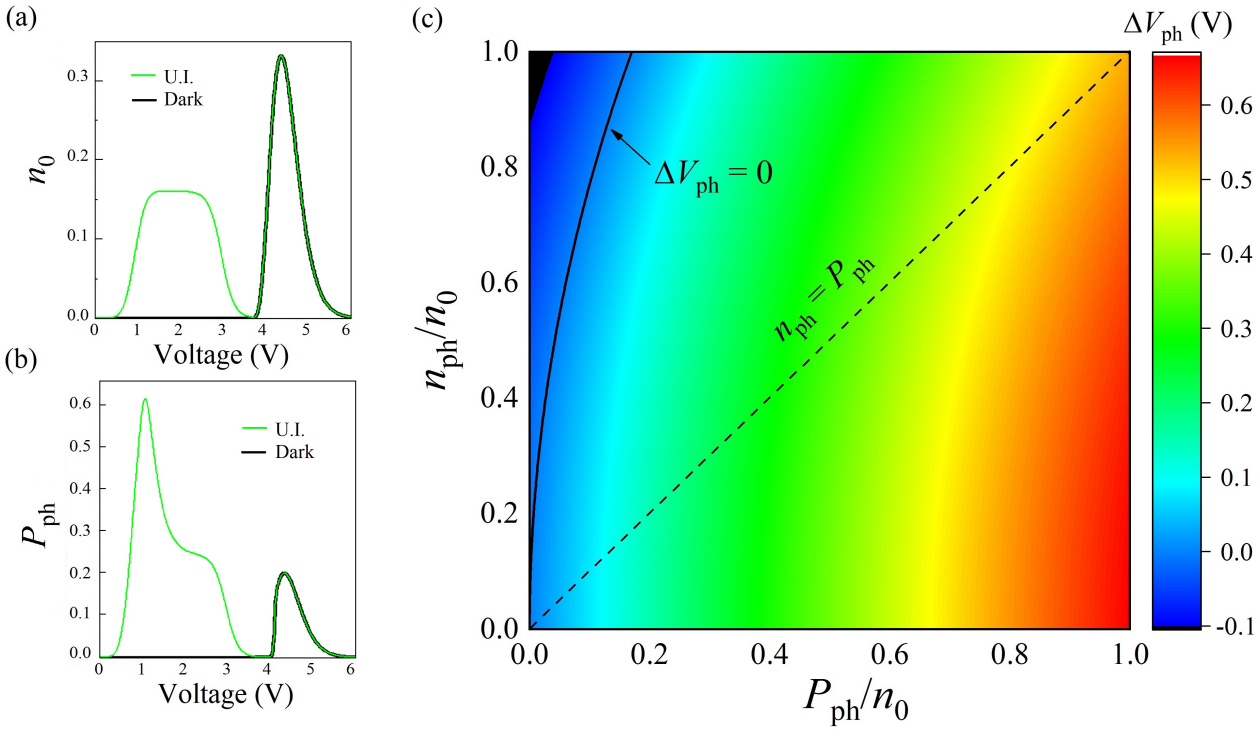

Figure 6.15: Calculated as a function of the applied voltage, photogenerated-trapped (a) electrons (b) holes. (c) calculated ΔV as function of the normalized photogenerated and accumulated charge carriers.

Figure 6.15 (c) demonstrates that only the photocreated holes are taking place at the voltage shift mechanism, producing exclusively positive shifts, imposing an increase of the total voltage drop. In contrast, photogenerated electrons have practically no influence on this performance. Probably when they take negative values (dark regions), a negative shift could be observed. However, accumulated electrons at the OW interface are expected to overcome the junction barrier more efficiently than the trapped holes under an applied forward bias voltage. In this case, $P_{ph} > n_{ph}$. Therefore, with extra accumulated holes,

the voltage shift will be increased. Thus, this corroborates the hypothesis that the QDs act as traps and retain the photogenerated holes.

As a result, the RTD nonlinear photoinduced voltage-shift function can be described by the voltage-dependent parameters exposed before and is depicted in Figure 6.16. The apparent flat range between 1.5 and 3 V observed experimentally, (Figure 6.11 (b)) was nearly reproduced, corroborating the fact that the accumulated photogenerated holes remain trapped by the QDs in this voltage range; thus, the escaping channels are reached for voltages above 3V approximately. The higher-voltages peak observed in Figures 6.15 (a), (b) and 6.16 refers to the voltage shift produced by the accumulation of charges due to the impact ionization process observed experimentally for voltages above 4.5V and studied by comparing with the theoretical (Schulman) simulated I(V)-characteristic (see Figure 6.11 (a)).

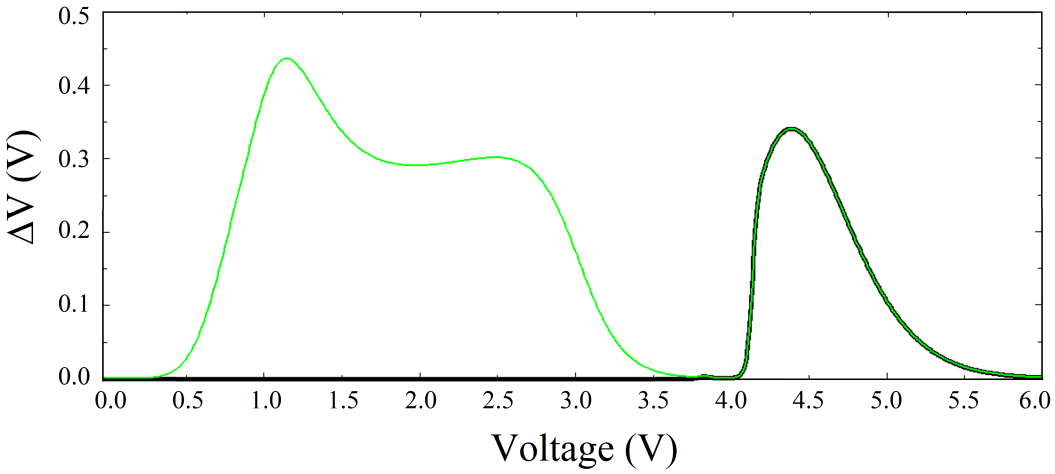

Figure 6.16: Voltage-shift ΔV calculated as a function of the applied voltage, using eq 6.9.

Despite the preceded discussion, the RTD photocurrent-voltage dependence is not only a nonlinear function of the applied bias voltage but also of the incident illumination power, as it was tried to elucidate in Figure 6.10. A constant photoresponse has been observed just for small excitation powers, where the photocurrent has been approximated as a linear function of P [42, 43, 124]. The linear approximation for small excitation powers is ideally for RTDs operating as photon counters. Therefore, to better understand this dependence, time-resolved photocurrent measurements were carried out for different incident laser powers. Figure 6.17 (a) shows the results obtained from the photocurrent difference (ΔI) when biasing the RTD at a fixed voltage of V =2.5 V and under illumination using an λ = 800 nm wavelength laser for illumination powers from P = 0.1 nW to 1 mW at a temperature of T = 2 K. In Figure 6.17 (b), the sensitivity defined as $S_I(P) = \Delta I/P$ is shown as a function of the laser power. The sensitivity reduces by five orders of

magnitude from 10^3 to 10^{-2}. At lower powers is expected to reach a constant flattening region, indicating the device's minimum measurable power, known as critical power (P), crucial for RTD photosensitivity characterization. Thus, for the operation of single-photon detection, sensing at narrow powers possible is highly valuable. However, the current in this region is below the resolution limit of the experimental setup. Thus no experimental data of ΔI data could be obtained for lower powers. It is important to bear in mind the possible bias in these electrical responses when operating the RTD in the voltage region/low current response (optically active QDs region) due to the resolution of the measurement equipment.

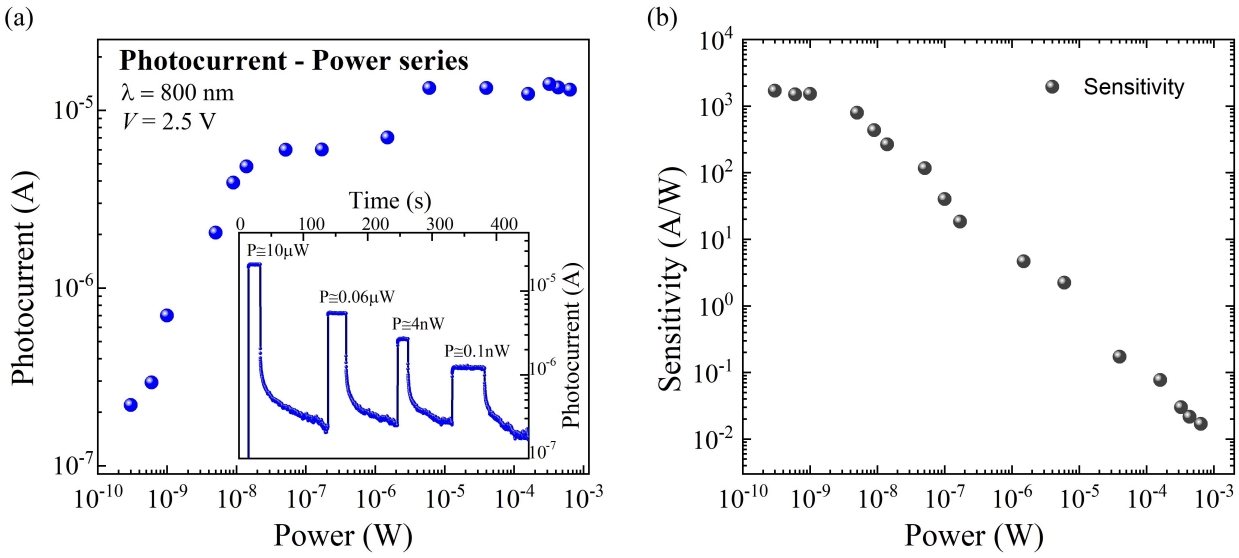

Figure 6.17: As a function of the incident illumination power, P, and for illumination powers from P = 0.1 nW to 1 mW (a) Photocurrent-power relation. The inset is showing the time-resolved measurements pattern. (b) Sensitivity of the photoinduced voltage shift.

The apparent flat at high voltages and the non-constant decreasing sensitivity are attributed to an excess of photogenerated holes. As already mentioned, a considerable accumulation of photogenerated holes at the DBS leads to the photoinduced voltage shift ΔV altering the electrostatic potential, changing the transmission probability and the resonant tunneling conditions itself, but at the same time allowing holes to escape through resonant channels or recombine with the accumulated electrons. Therefore, the charge carrier confinement by the QD-RTD is a self-limiting process. Practical detectors have shown an uncertain response [49]. Thus, defining the working-point region rigorously for different parameters as voltage, laser power and energy to resolve photon number counting is highly required.

6.3.2 Conclusions

First of all, the peak current-density exhibits a strong modulation as a function of barrier thickness, with nearly exponential dependence. On the other hand, QDs emissions were observed even under electric fields where a strong influence on the local electrostatic potential is noted. Despite minor changes in the electric field, the QDS emissions were affected, quenching them for voltages above 0.9 V in the positive bias and above -3.3 V in the negative bias current is still no flowing. I(V)-characteristics in the dark and under illumination showed a highly sensitive but not constant photocurrent that depends strongly on the incident illumination power and energy and bias voltage; this response is mainly due to photogenerated holes captured by QDs. Electroluminescence emission was observed above the resonance condition, revealing other mechanisms of charge generations as impact ionization, which in turn interfere with the potential, generating new charges carriers that can be accumulated along with the structure as well. Especially this feature allows the determination of the optimal working point as a photodetector where the charge carrier accumulation mechanism offsets recombination processes and parasitic effects such as electroluminescence emissions are absent.

A theoretical explanation of how the accumulation of the generated charge carriers within the QD-RTD exhibits a nonlinear photoinduced voltage-shift function is proposed. Defined by a voltage-dependent function with parameters such as the quantum efficiency $\eta(V)$, how efficient are the photogeneration and capture of charge carriers. the escape rate of accumulated charge carriers $\tau(V)$, the absorption coefficient $\alpha(V)$, electronic transport properties, i.e., RTD's current-voltage characteristics in the dark $I(V)$ and the impact ionization coefficient $\Pi(V)$. However, the RTD photocurrent-voltage dependence is not only a nonlinear function of the applied bias voltage but also of the incident illumination power. Sensitivity values from photocurrent measurements as a function of the laser power were obtained. The QD-RTD was able to measure changes in the photocurrent of the order of tenths of μA and for powers around tenths of nW. Nevertheless, the current in this range is below the resolution limit of the experimental setup. Thus no experimental data could be obtained for lower powers. Due to this limitation, the experiments for the numerical resolution of single photons could not be concluded.

Conclusions

The first study of this thesis investigated experimentally and theoretically the magneto- and thermo-optical characteristics of excitonic quasi-particles in a GaAs quantum well. It has been proved the nature of a low energy excitonic peak, showing that it can be attributed to a biexciton emission, and that its dynamics are nearly decoupled from the other excitonic complexes, and that with a non-resonant excitation, the biexcitons are mainly photo-created. The biexcitons PL emission shows a supralinear dependence on laser power, strongly decreasing with increasing temperature, and shows a monotonic Zeeman splitting, a constant g-factor, and a polarization that is defined by the thermal population of the Zeeman sublevels. On the other hand, the higher-energy peak showed an increasing splitting, ascribed to both exciton and a magnetically-induced state, which is consistent with a negative trion. This state appears predominantly for $\sigma+$ polarization under a finite magnetic field and has a strong influence on the exciton emission. The exciton spin splitting and polarization depend on both laser power and external magnetic field.

As a second part, a comparison of a reference (GaAs/AlGaAs) and the Prewell (i-$In_{0.15}Ga_{0.85}As$) resonant tunneling diodes was carried out by combining magneto-transport and electroluminescence measurements. Via magneto-transport results, the charge carrier density for both samples was resolved. However, there are clear differences between both samples on their optical and transport properties, which can be mainly attributed to the prewell presence, such as the LL splitting and the lack of current oscillation after the resonance peak. These results give valuable information on the charge carrier dynamics, such as charge build-up and thermalization processes, which can be useful on device fabrication for practical applications.

The last part presents a general study of an n-doped GaAs/AlGaAs resonant tunneling diode with an integrated InGaAs QDs layer grown near the active region of the diode. Transport, photocurrent, and optical spectroscopy measurements were carried out. It was proved that the resonant current density could be tuned by adjusting the AlAs barrier thickness. Also, it was possible to detect and capture a single charge in a QD caused by a photon, despite the charge carrier confinement by the QD being a self-limiting process, it was possible to determine an optimal working point as a photodetector, defining

the working-point region rigorously for different parameters as voltage, laser power, and energy to resolve photon number counting is highly required because controlling the operation of high-sensitivity single-photon detector. Finally, the highly sensitive nonlinear, photoinduced voltage-shift and photocurrent that depends on the incident light and voltage has been explained within a theoretical model.

In this way, this thesis contributes to an accurate elucidation of excitonic complexes in quantum wells, a complete mapping in the estimation of the charge density across the voltage range of a resonant tunneling diode, and the determination of the parameters that can lead this device to become a high-sensitivity single-photon detector, and in general, to pave the development of more efficient semiconductor devices design and fabrication for practical applications.

6.4 Publications

Articles published in international journals during this work:

- *Physica E: Low-dimensional Systems and Nanostructures: A. Naranjo, H. Bragança, G. M. Jacobsen, R. R. O de Morais, A.A. Quivy, G.E. Marques, V. Lopez-Richard, M.D. Teodoro. 2021. Magnetic and power tuning of spin-asymmetric multiple excitons in a GaAs quantum well (Vol. 129, 114599).*

- *Physical Review Applied: E. R. Cardozo de Oliveira, A. Naranjo, A. Pfenning, V. Lopez-Richard, G.E. Marques, L. Worschech, F. Hartmann, S. Höfling, and M. D. Teodoro. 2021. Determination of carrier density and dynamics via magneto-electroluminescence spectroscopy in resonant tunneling diodes.(Vol. 15, 014042)*

- *International Society for Optics and Photonics: Pfenning, A., Jurkat, J., Naranjo, A., Köck, D., Hartmann, F., Höfling, S. 2019. Resonant tunneling diode photon number resolving single-photon detectors. Infrared Remote Sensing and Instrumentation XXVII (Vol. 11128, p. 1112808).*

Bibliography

[1] Robert N Noyce. Semiconductor device-and-lead structure, reprint of us patent 2,981,877 (issued april 25, 1961. filed july 30, 1959). *IEEE Solid-State Circuits Society Newsletter*, 12(2):34–40, 2007.

[2] Jean-François Eloy and Michel Depeyrot. Nanometer range: a new theoretical challenge for microelectronics and optoelectronics. *Microelectronics journal*, 37(7): 630–634, 2006.

[3] Leo Esaki. New phenomenon in narrow germanium p- n junctions. *Physical review*, 109(2):603, 1958.

[4] Leo Esaki and Ray Tsu. Superlattice and negative differential conductivity in semiconductors. *IBM Journal of Research and Development*, 14(1):61–65, 1970.

[5] R Tsu and Leo Esaki. Tunneling in a finite superlattice. *Applied Physics Letters*, 22(11):562–564, 1973.

[6] Raphael Tsu. *Superlattice to nanoelectronics*. Elsevier, 2010.

[7] David Ferry and Stephen Marshall Goodnick. *Transport in nanostructures*. Number 6. Cambridge university press, 1999.

[8] Michael M Fogler, Sergey V Malinin, and Thomas Nattermann. Coulomb blockade and transport in a chain of one-dimensional quantum dots. *Physical review letters*, 97(9):096601, 2006.

[9] Leroy L Chang, EE Mendez, and C Tejedor. *Resonant Tunneling in Semiconductors: Physics and Applications*, volume 277. Springer Science & Business Media, 2012.

[10] Simon M Sze and Kwok K Ng. *Physics of semiconductor devices*. John wiley & sons, 2006.

[11] Jasprit Singh. *Electronic and optoelectronic properties of semiconductor structures*. Cambridge University Press, 2007.

[12] G. Bastard and J. Schulman. Wave mechanics applied to semiconductor heterostructures. 1988.

[13] O. Madelung. *Semiconductors Group IV Elements and III-V Compounds*. Springer, 1991.

[14] John H Davies. *The physics of low-dimensional semiconductors: an introduction*. Cambridge university press, 1998.

[15] FM Peeters and O Hipólito. Low dimensional semiconductor structures. *Brazilian Journal of Physics*, 22(3):183–193, 1992.

[16] Gleb Finkelstein, Hadas Shtrikman, and Israel Bar-Joseph. Negatively and positively charged excitons in gaas/al x ga 1- x as quantum wells. *Physical Review B*, 53(4):R1709, 1996.

[17] BP Zakharchenya and SA Permogorov. Exciton complexes. In *Encyclopedia of condensed matter physics*, pages 166–171. 2005.

[18] P. Michler, editor. *Single Semiconductor Quantum Dots*. Springer, 2009.

[19] Eilon Poem, Yaron Kodriano, Netanel H Lindner, Brian D Gerardot, Pierre M Petroff, and David Gershoni. The dark exciton in a quantum dot-a novel bright qubit with very long coherence time. In *Quantum Electronics and Laser Science Conference*, page QPDA9. Optical Society of America, 2010.

[20] L. Schultheis, A. Honold, J. Kuhl, K. Köhler, and C. W. Tu. Optical dephasing of homogeneously broadened two-dimensional exciton transitions in gaas quantum wells. *Phys. Rev. B*, 34:9027–9030, Dec 1986. doi: 10.1103/PhysRevB.34.9027.

[21] Daniel B Turner, Patrick Wen, Dylan H Arias, Keith A Nelson, Hebin Li, Galan Moody, Mark E Siemens, and Steven T Cundiff. Persistent exciton-type many-body interactions in gaas quantum wells measured using two-dimensional optical spectroscopy. *Physical Review B*, 85(20):201303, 2012.

[22] Michael Rohlfing and Steven G Louie. Electron-hole excitations and optical spectra from first principles. *Physical Review B*, 62(8):4927, 2000.

[23] Rohan Singh, Travis M Autry, Gaël Nardin, Galan Moody, Hebin Li, Klaus Pierz, Mark Bieler, and Steven T Cundiff. Anisotropic homogeneous linewidth of the heavy-hole exciton in (110)-oriented gaas quantum wells. *Physical Review B*, 88(4): 045304, 2013.

[24] Giovanni Onida, Lucia Reining, and Angel Rubio. Electronic excitations: density-functional versus many-body greens-function approaches. *Reviews of modern physics*, 74(2):601, 2002.

[25] MJ Snelling, E Blackwood, CJ McDonagh, RT Harley, and CTB Foxon. Exciton, heavy-hole, and electron g factors in type-i gaas/al x ga 1- x as quantum wells. *Physical Review B*, 45(7):3922, 1992.

[26] S Haldar, A Banerjee, Geetanjali Vashisht, S Porwal, TK Sharma, and VK Dixit. A parallel magnetic field driven confinement versus separation of charges in gaas quantum well investigated by magneto-photovoltage and magneto-photoluminescence spectroscopy. *Journal of Luminescence*, 206:342–347, 2019.

[27] ALC Triques, J Urdanivia, F Iikawa, MZ Maialle, JA Brum, and G Borhgs. Electron-spin polarization near the fermi level in n-type modulation-doped semiconductor quantum wells. *Physical Review B*, 59(12):R7813, 1999.

[28] MZ Maialle, EA de Andrada e Silva, and LJ Sham. Exciton spin dynamics in quantum wells. *Physical Review B*, 47(23):15776, 1993.

[29] Debasis Bera, Lei Qian, Teng-Kuan Tseng, and Paul H Holloway. Quantum dots and their multimodal applications: a review. *Materials*, 3(4):2260–2345, 2010.

[30] Alexey I Ekimov and Alexei A Onushchenko. Quantum size effect in three-dimensional microscopic semiconductor crystals. *Jetp Lett*, 34(6):345–349, 1981.

[31] Alexander L Efros and Al L Efros. Interband absorption of light in a semiconductor sphere. *sov. phys. semicond*, 16(7):772–775, 1982.

[32] M. Bayer, G. Ortner, O. Stern, A. Kuther, A. A. Gorbunov, A. Forchel, P. Hawrylak, S. Fafard, K. Hinzer, T. L. Reinecke, S. N. Walck, J. P. Reithmaier, F. Klopf, and F. Schaefer. Fine structure of neutral and charged excitons in self-assembled in(ga)as/(al)GaAs quantum dots. *Physical Review B*, 65(19), may 2002. doi: 10.1103/physrevb.65.195315.

[33] G. Shan, Z. Yin, C. H. Shek, and W. Huang. Single photon sources with single semiconductor quantum dots. *Frontiers of Physics*, 9(2):170–193, sep 2013. doi: 10.1007/s11467-013-0360-6.

[34] Jan Niklas Donges. Efficient single photon sources based on inas quantum dots in bullseye microcavities. Master's thesis, Institute of Physics, Julius-Maximilians-Universität Würzburg, 2020.

[35] VJ Goldman, DC Tsui, and JE Cunningham. Observation of intrinsic bistability in resonant tunneling structures. *Physical Review Letters*, 58(12):1256, 1987.

[36] Jian Ping Sun, George I Haddad, Pinaki Mazumder, and Joel N Schulman. Resonant tunneling diodes: Models and properties. *Proceedings of the IEEE*, 86(4):641–660, 1998.

[37] Hiroshi Mizuta and Tomonori Tanoue. *The physics and applications of resonant tunnelling diodes*. Number 2. Cambridge university press, 2006.

[38] Craig Allford. *Resonant tunnelling in GaAs/AlGaAs triple barrier heterostructures*. PhD thesis, Cardiff University, 2016.

[39] PH Rivera and PA Schulz. Characterization of resonant tunneling paths in current–voltage characteristics line shapes. *Applied physics letters*, 67(18):2675–2677, 1995.

[40] JN Schulman, HJ De Los Santos, and DH Chow. Physics-based rtd current-voltage equation. *IEEE Electron Device Letters*, 17(5):220–222, 1996.

[41] Peiji Zhao, Dwight L Woolard, and HL Cui. Multisubband theory for the origination of intrinsic oscillations within double-barrier quantum well systems. *Physical Review B*, 67(8):085312, 2003.

[42] A Pfenning, F Hartmann, M Rebello Sousa Dias, LK Castelano, C Süßmeier, F Langer, S Höfling, M Kamp, GE Marques, L Worschech, et al. Acs nano 9, 6271 (2015).

[43] Andreas Pfenning, Fabian Hartmann, Mariama Rebello Sousa Dias, Fabian Langer, Martin Kamp, Leonardo Kleber Castelano, Victor Lopez-Richard, Gilmar Eugenio Marques, Sven Höfling, and Lukas Worschech. Photocurrent-voltage relation of resonant tunneling diode photodetectors. *Applied Physics Letters*, 107(8):081104, 2015.

[44] F Hartmann, F Langer, D Bisping, A Musterer, S Höfling, M Kamp, A Forchel, and L Worschech. Gaas/algaas resonant tunneling diodes with a gainnas absorption layer for telecommunication light sensing. *Applied Physics Letters*, 100(17):172113, 2012.

[45] F Hartmann, A Pfenning, M Rebello Sousa Dias, F Langer, Sven Höfling, M Kamp, L Worschech, LK Castelano, GE Marques, and V Lopez-Richard. Temperature tuning from direct to inverted bistable electroluminescence in resonant tunneling diodes. *Journal of Applied Physics*, 122(15):154502, 2017.

[46] HT Grahn. Magneto-tunneling between 2-dimensional systems. In *Low-Dimensional Electronic Systems*, pages 157–166. Springer, 1992.

[47] DJ Robbins. Aspects of the theory of impact ionization in semiconductors (i). *physica status solidi (b)*, 97(1):9–50, 1980.

[48] LV Keldysh. Concerning the theory of impact ionization in semiconductors. *Sov. Phys. JETP*, 21(6):1135, 1965.

[49] Qianchun Weng, Zhenghua An, Bo Zhang, Pingping Chen, Xiaoshuang Chen, Ziqiang Zhu, and Wei Lu. Quantum dot single-photon switches of resonant tunneling current for discriminating-photon-number detection. *Scientific reports*, 5(1): 1–5, 2015.

[50] Robert H Hadfield. Single-photon detectors for optical quantum information applications. *Nature photonics*, 3(12):696–705, 2009.

[51] Akio Yoshizawa and Hidemi Tsuchida. A 1550 nm single-photon detector using a thermoelectrically cooled ingaas avalanche photodiode. *Japanese Journal of Applied Physics*, 40(1R):200, 2001.

[52] Michael Varnava, Daniel E Browne, and Terry Rudolph. How good must single photon sources and detectors be for efficient linear optical quantum computation? *Physical review letters*, 100(6):060502, 2008.

[53] ZL Yuan, BE Kardynal, AW Sharpe, and AJ Shields. High speed single photon detection in the near infrared. *Applied Physics Letters*, 91(4):041114, 2007.

[54] A Dorokhov, A Glauser, Y Musienko, C Regenfus, S Reucroft, and J Swain. Recent progress on cooled avalanche photodiodes for single photon detection. *Journal of modern optics*, 51(9-10):1351–1357, 2004.

[55] BE Kardynał, SS Hees, AJ Shields, C Nicoll, I Farrer, and DA Ritchie. Photon number resolving detector based on a quantum dot field effect transistor. *Applied physics letters*, 90(18):181114, 2007.

[56] AJ Shields, MP O sullivan, I Farrer, DA Ritchie, RA Hogg, ML Leadbeater, CE Norman, and M Pepper. Detection of single photons using a field-effect transistor gated by a layer of quantum dots. *Applied Physics Letters*, 76(25):3673–3675, 2000.

[57] Mary A Rowe, EJ Gansen, Marion Greene, RH Hadfield, TE Harvey, MY Su, Sae Woo Nam, RP Mirin, and D Rosenberg. Single-photon detection using a quantum dot optically gated field-effect transistor with high internal quantum efficiency. *Applied physics letters*, 89(25):253505, 2006.

[58] JC Blakesley, P See, AJ Shields, BE Kardynał, P Atkinson, I Farrer, and DA Ritchie. Efficient single photon detection by quantum dot resonant tunneling diodes. *Physical review letters*, 94(6):067401, 2005.

[59] HW Li, BE Kardynał, P See, AJ Shields, P Simmonds, HE Beere, and DA Ritchie. Quantum dot resonant tunneling diode for telecommunication wavelength single photon detection. *Applied physics letters*, 91(7):073516, 2007.

[60] Andreas Pfenning, Jonathan Jurkat, Andrea Naranjo, Dominik Köck, Fabian Hartmann, and Sven Höfling. Resonant tunneling diode photon number resolving single-photon detectors. In *Infrared Remote Sensing and Instrumentation XXVII*, volume 11128, page 1112808. International Society for Optics and Photonics, 2019.

[61] Andrew J Shields. Semiconductor quantum light sources. *Nanoscience And Technology: A Collection of Reviews from Nature Journals*, pages 221–229, 2010.

[62] John Arthur. Molecular beam epitaxy. *Surface Science*, 500:189–217, 03 2002. doi: 10.1016/S0039-6028(01)01525-4.

[63] Jorge Puebla. *Spin phenomena in semiconductor quantum dots*. PhD thesis, 10 2012.

[64] H. Sitter M.A. Herman. *Molecular Beam Epitaxy, Fundamentals and Current Status*. Springer Series, 1989.

[65] J. Wu and P. Jin. Self-assembly of InAs quantum dots on GaAs(001) by molecular beam epitaxy. *Frontiers of Physics*, 10(1):7–58, feb 2015. doi: 10.1007/s11467-014-0422-4.

[66] Kamel Rezgui, Riadh Othmen, Antonella Cavanna, Hosni Ajlani, Ali Madouri, and Meherzi Oueslati. The improvement of inas/gaas quantum dot properties capped by graphene. *Journal of Raman Spectroscopy*, 44(11):1529–1533, 2013.

[67] L. Wang, A. Rastelli, and O. G. Schmidt. Structural and optical properties of ingaasgaas quantum dots treated by partial capping and annealing. *Journal of Applied Physics*, 100(6):064313, sep 2006. doi: 10.1063/1.2349432.

[68] A. Babiński, J. Jasiński, R. Bożek, A. Szepielow, and J. M. Baranowski. Rapid thermal annealing of InAs/GaAs quantum dots under a GaAs proximity cap. *Applied Physics Letters*, 79(16):2576–2578, oct 2001. doi: 10.1063/1.1412279.

[69] RRO Morais, IFL Dias, MAT Da Silva, DF Cesar, JL Duarte, SA Lourenço, E Laureto, ECF Da Silva, and AA Quivy. Effects of confinement on the electron–phonon

interaction in al0. 18ga0. 82as/gaas quantum wells. *Journal of Physics: Condensed Matter*, 21(15):155601, 2009.

[70] James G Fujimoto and Daniel Farkas. *Biomedical optical imaging*. Oxford University Press, 2009.

[71] M. Minsky. Memoir on inventing the confocal scanning microscope. *Scanning*, 10 (4):128–138, 1988. doi: 10.1002/sca.4950100403. URL https://onlinelibrary.wiley.com/doi/abs/10.1002/sca.4950100403.

[72] Vikram Prasad, Denis Semwogerere, and Eric R Weeks. Confocal microscopy of colloids. *Journal of Physics: Condensed Matter*, 19(11):113102, 2007.

[73] Stefan Wilhelm, Bernhard Grobler, Martin Gluch, and Hartmut Heinz. Confocal laser scanning microscopy. principles. *Microscopy from Carl Zeiss, microspecial*, 2003.

[74] Dirk Englund, Arka Majumdar, Andrei Faraon, Mitsuru Toishi, Nick Stoltz, Pierre Petroff, and Jelena Vučković. Resonant excitation of a quantum dot strongly coupled to a photonic crystal nanocavity. *Phys. Rev. Lett.*, 104:073904, Feb 2010.

[75] E. R. Cardozo de Oliveira, A. Naranjo, A. Pfenning, V. Lopez-Richard, G. E. Marques, L. Worschech, F. Hartmann, S. HÃ¶fling, and M. D. Teodoro. Determination of carrier density and dynamics via magneto-electroluminescence spectroscopy in resonant tunneling diodes, 2020.

[76] YU Peter and Manuel Cardona. *Fundamentals of semiconductors: physics and materials properties*. Springer Science & Business Media, 2010.

[77] JW Cockburn, MS Skolnick, JPR David, R Grey, G Hill, and MA Pate. Impact ionization and electroluminescence in single barrier tunnelling structures. *Superlattices and microstructures*, 12(4):443–446, 1992.

[78] Shmuel Glasberg, Gleb Finkelstein, Hadas Shtrikman, and Israel Bar-Joseph. Comparative study of the negatively and positively charged excitons in gaas quantum wells. *Physical Review B*, 59(16):R10425, 1999.

[79] JL Osborne, AJ Shields, M Pepper, FM Bolton, and DA Ritchie. Photoluminescence due to positively charged excitons in undoped gaas/al x ga 1- x as quantum wells. *Physical Review B*, 53(19):13002, 1996.

[80] Axel Esser, Erich Runge, Roland Zimmermann, and Wolfgang Langbein. Photoluminescence and radiative lifetime of trions in gaas quantum wells. *Physical Review B*, 62(12):8232, 2000.

[81] J Jadczak, M Kubisa, K Ryczko, L Bryja, and M Potemski. High magnetic field spin splitting of excitons in asymmetric gaas quantum wells. *Physical Review B*, 86 (24):245401, 2012.

[82] Israel Bar-Joseph. Trions in gaas quantum wells. *Semiconductor science and technology*, 20(6):R29, 2005.

[83] Jai Singh, Dan Birkedal, VG Lyssenko, and Jørn Märcher Hvam. Binding energy of two-dimensional biexcitons. *Physical Review B*, 53(23):15909, 1996.

[84] Dan Birkedal, Jai Singh, VG Lyssenko, J Erland, and Jørn Märcher Hvam. Binding of quasi-two-dimensional biexcitons. *Physical Review Letters*, 76(4):672, 1996.

[85] VV Belykh and MV Kochiev. Heating by exciton and biexciton recombination in gaas/algaas quantum wells. *Physical Review B*, 92(4):045307, 2015.

[86] DA Kleinman. Binding energy of biexcitons and bound excitons in quantum wells. *Physical Review B*, 28(2):871, 1983.

[87] S Charbonneau, T Steiner, MLW Thewalt, Emil S Koteles, JY Chi, and B Elman. Optical investigation of biexcitons and bound excitons in gaas quantum wells. *Physical Review B*, 38(5):3583, 1988.

[88] R. C. Miller, D. A. Kleinman, A. C. Gossard, and O. Munteanu. Biexcitons in gaas quantum wells. *Phys. Rev. B*, 25:6545–6547, May 1982.

[89] A Naranjo, H Bragança, GM Jacobsen, RRO de Morais, AA Quivy, GE Marques, V Lopez-Richard, and MD Teodoro. Magnetic and power tuning of spin-asymmetric multiple excitons in a gaas quantum well. *Physica E: Low-dimensional Systems and Nanostructures*, page 114599, 2020.

[90] DJ Lovering, RT Phillips, GJ Denton, and GW Smith. Resonant generation of biexcitons in a gaas quantum well. *Physical review letters*, 68(12):1880, 1992.

[91] Alok Rudra, Emanuele Pelucchi, Daniel Y. Oberli, Nicolas Moret, Benjamin Dwir, and Eli Kapon. Properties of gaas/algaas quantum wells grown by movpe using vicinal gaas substrates. *Journal of Crystal Growth*, 272(1):615–620, 2004. ISSN 0022-0248. doi: https://doi.org/10.1016/j.jcrysgro.2004.09.047. URL https://www.sciencedirect.com/science/article/pii/S0022024804011042. The Twelfth International Conference on Metalorganic Vapor Phase Epitaxy.

[92] C. Delalande, M. H. Meynadier, and M. Voos. Effect of temperature on exciton trapping on interface defects in gaas quantum wells. *Phys. Rev. B*, 31:2497–2498,

Feb 1985. doi: 10.1103/PhysRevB.31.2497. URL https://link.aps.org/doi/10.1103/PhysRevB.31.2497.

[93] NJ Traynor, RJ Warburton, MJ Snelling, and RT Harley. Highly nonlinear zeeman splitting of excitons in semiconductor quantum wells. *Physical Review B*, 55(23): 15701, 1997.

[94] Leonardo K Castelano, Daniel Ferreira Cesar, Victor Lopez-Richard, Gilmar E Marques, Odilon DD Couto Jr, Fernando Iikawa, Rudolf Hey, and Paulo V Santos. Zeeman splitting and spin dynamics tuning by exciton charging in two-dimensional systems. *Physical Review B*, 84(20):205332, 2011.

[95] RT Phillips, DJ Lovering, GJ Denton, and GW Smith. Biexciton creation and recombination in a gaas quantum well. *Physical Review B*, 45(8):4308, 1992.

[96] VD Kulakovskii, G Bacher, R Weigand, T Kümmell, A Forchel, E Borovitskaya, K Leonardi, and D Hommel. Fine structure of biexciton emission in symmetric and asymmetric cdse/znse single quantum dots. *Physical Review Letters*, 82(8):1780, 1999.

[97] Oliver Stier, Marius Grundmann, and Dieter Bimberg. Electronic and optical properties of strained quantum dots modeled by 8-band k. p theory. *Physical Review B*, 59(8):5688, 1999.

[98] R Seguin, A Schliwa, S Rodt, K Pötschke, UW Pohl, and D Bimberg. Size-dependent fine-structure splitting in self-organized inas/gaas quantum dots. *Physical review letters*, 95(25):257402, 2005.

[99] N Akopian, NH Lindner, E Poem, Y Berlatzky, J Avron, D Gershoni, BD Gerardot, and PM Petroff. Entangled photon pairs from semiconductor quantum dots. *Physical review letters*, 96(13):130501, 2006.

[100] S Rodt, R Heitz, A Schliwa, RL Sellin, F Guffarth, and D Bimberg. Repulsive exciton-exciton interaction in quantum dots. *Physical Review B*, 68(3):035331, 2003.

[101] Vladan Mlinar and Alex Zunger. Internal electronic structure and fine structure of multiexcitons in semiconductor quantum dots. *Physical Review B*, 80(20):205311, 2009.

[102] Gerald Hönig, Gordon Callsen, Andrei Schliwa, Stefan Kalinowski, Christian Kindel, Satoshi Kako, Yasuhiko Arakawa, Dieter Bimberg, and Axel Hoffmann. Manifestation of unconventional biexciton states in quantum dots. *Nature communications*, 5:5721, 2014.

[103] E Hal Bogardus and H Barry Bebb. Bound-exciton, free-exciton, band-acceptor, donor-acceptor, and auger recombination in gaas. *Physical Review*, 176(3):993, 1968.

[104] J Wagner and M Ramsteiner. Binding energies of shallow donors in semi-insulating gaas. *Journal of applied physics*, 62(5):2148–2150, 1987.

[105] Lara F Dos Santos, Yara Galvão Gobato, Márcio D Teodoro, Victor Lopez-Richard, Gilmar E Marques, Maria JSP Brasil, Milan Orlita, Jan Kunc, Duncan K Maude, Mohamed Henini, et al. Circular polarization in a non-magnetic resonant tunneling device. *Nanoscale research letters*, 6(1):1–7, 2011.

[106] HB De Carvalho, MJSP Brasil, V Lopez-Richard, Y Galvao Gobato, GE Marques, I Camps, LCO Dacal, M Henini, L Eaves, and G Hill. Electric-field inversion asymmetry: Rashba and stark effects for holes in resonant tunneling devices. *Physical Review B*, 74(4):041305, 2006.

[107] LF Dos Santos, Y Galvão Gobato, V Lopez-Richard, GE Marques, MJSP Brasil, M Henini, and RJ Airey. Polarization resolved luminescence in asymmetric n-type ga as/ al ga as resonant tunneling diodes. *Applied Physics Letters*, 92(14):143505, 2008.

[108] ER Cardozo de Oliveira, A Pfenning, ED Guarin Castro, MD Teodoro, EC dos Santos, V Lopez-Richard, GE Marques, L Worschech, F Hartmann, and Sven Höfling. Electroluminescence on-off ratio control of n- i- n gaas/algaas-based resonant tunneling structures. *Physical Review B*, 98(7):075302, 2018.

[109] M Sugarawa, N Okazaki, and T Fujii. Ph and s. yamazaki. *Phys. Rev. B*, 48:8848, 1993.

[110] M Potemski, JC Maan, K Ploog, and G Weimann. Properties of a dense quasi-two-dimensional electron-hole gas at high magnetic fields. *Solid state communications*, 75(3):185–188, 1990.

[111] CJ Goodings, Hiroshi Mizuta, and JRA Cleaver. Electrical studies of charge build-up and phonon-assisted tunneling in double-barrier materials with very thick spacer layers. *Journal of applied physics*, 75(4):2291–2293, 1994.

[112] JC Maan, Y Guldner, JP Vieren, P Voisin, M Voos, LL Chang, and L Esaki. Three-dimensional character of semimetallic inas-gasb superlattices. *Solid State Communications*, 39(5):683–686, 1981.

[113] ED Jones, SK Lyo, IJ Fritz, JF Klem, JE Schirber, CP Tigges, and TJ Drummond. Determination of energy-band dispersion curves in strained-layer structures. *Applied physics letters*, 54(22):2227–2229, 1989.

[114] Kyu-Seok Lee, Chae-Deok Lee, Yongmin Kim, and Sam Kyu Noh. Dependence of the heavy-hole exciton reduced mass on quantum-well size in ingaas/gaas heterostructures. *Solid state communications*, 128(5):177–180, 2003.

[115] L Eaves, GA Toombs, FW Sheard, CA Payling, ML Leadbeater, ES Alves, TJ Foster, PE Simmonds, M Henini, OH Hughes, et al. Sequential tunneling due to intersubband scattering in double-barrier resonant tunneling devices. *Applied physics letters*, 52(3):212–214, 1988.

[116] L Eaves, ML Leadbeater, DG Hayes, ES Alves, FW Sheard, GA Toombs, PE Simmonds, MS Skolnick, M Henini, and OH Hughes. Electrical and spectroscopic studies of space-charged buildup, energy relaxation and magnetically enhanced bistability in resonant-tunneling structures. *Solid-state electronics*, 32(12):1101–1108, 1989.

[117] ML Leadbeater, ES Alves, FW Sheard, L Eaves, M Henini, OH Hughes, and GA Toombs. Observation of space-charge bulk-up and thermalisation in an asymmetric double-barrier resonant tunnelling structure. *Journal of Physics: Condensed Matter*, 1(51):10605, 1989.

[118] M Líbezný, SC Jain, Jef Poortmans, Matty Caymax, Johan Nijs, Robert Mertens, K Werner, and P Balk. Photoluminescence determination of the fermi energy in heavily doped strained si1- x ge x layers. *Applied physics letters*, 64(15):1953–1955, 1994.

[119] Nam-Young Lee, Kyu-Jang Lee, Chul Lee, Jae-Eun Kim, Hae Yong Park, Dong-Hwa Kwak, Hee-Chul Lee, and H Lim. Determination of conduction band tail and fermi energy of heavily si-doped gaas by room-temperature photoluminescence. *Journal of applied physics*, 78(5):3367–3370, 1995.

[120] W-H Chang, W-Y Chen, H-S Chang, TM Hsu, T-P Hsieh, and J-I Chyi. Optical emission from individual ingaas quantum dots in single-defect photonic crystal nanocavity. *Journal of applied physics*, 98(3):034306, 2005.

[121] M Bayer. 0. stern, p. hawrylak, s. fafard and a. forchel. *Nature*, 405:923, 2000.

[122] IJS Coêlho, JF Martins-Filho, JML Figueiredo, and CN Ironside. Modeling of light-sensitive resonant-tunneling-diode devices. *Journal of applied physics*, 95(12): 8258–8263, 2004.

[123] Pyong Woon Park, Hye Yong Chu, Seon Gyu Han, Young Wan Choi, Gyungock Kim, and El-Hang Lee. Optical switching mechanism based on charge accumulation effects in resonant tunneling diodes. *Applied physics letters*, 67(9):1241–1243, 1995.

[124] Andreas Pfenning, Fabian Hartmann, Fabian Langer, Martin Kamp, Sven Höfling, and Lukas Worschech. Sensitivity of resonant tunneling diode photodetectors. *Nanotechnology*, 27(35):355202, 2016.

[125] JA Brum and G Bastard. Electric-field-induced dissociation of excitons in semiconductor quantum wells. *Physical Review B*, 31(6):3893, 1985.

[126] Robert A Morgan. Improvements in self electro-optic effect devices: toward system implementation. In *Devices for Optical Processing*, volume 1562, pages 213–227. International Society for Optics and Photonics, 1991.